Assembly of gold nanoparticles into regular clusters inside emulsion droplets

Dipl.-Ing. Johann Lacava

Dissertation
zur Erlangung des Grades
des Doktors der Ingenieurwissenschaften
der Naturwissenschaftlich-Technischen Fakultät III
Chemie, Pharmazie, Bio- und Werkstoffwissenschaften
der Universität des Saarlandes

INM-Leibniz Institute for New Materials
Universität des Saarlandes

Saarbrücken
2014

Tag des Kolloquiums: 24.11.2014

Dekan: Prof. Dr.-Ing. Dirk Bähre

Berichterstatter: Prof. Dr. Eduard Arzt

Prof. Dr. Guido Kickelbick

Vorsitzende: Prof. Dr.-Ing. Dirk Bähre

Akad. Mitarbeiter: Dr. Tobias Kraus

La pierre n'a point d'espoir d'être autre chose que pierre.
Mais de collaborer, elle s'assemble et devient temple.

Antoine de Saint-Exupéry

Acknowledgements

This thesis would not have come true without the help, advice and support of different persons that I would like to acknowledge here.

First and foremost, I would like to thank **Professor Eduard Arzt** for giving me the opportunity to successfully lead this thesis at the INM and to enhance my researches in such an interesting field. I would like to acknowledge him for his trust in my qualities and abilities. I also sincerely acknowledge **Professor Guido Kickelbick** for accepting to act as second referee of this thesis.

This work was performed in the structure formation group at the INM and I'm extremely grateful to **Dr. Tobias Kraus** who accepted me as a PhD student in his group. Tobias Kraus has been a constant and passionate scientific guide. His patience and trust have been very important for me to develop my own thoughts, and his attitude towards science and his open-mindedness have greatly influenced my perception about scientific research.

This thesis is the result of a collective effort of many people that collaborated directly with me. First of all I would like to thank **Anika Weber** for the thousand synthesis she did. Moreover she collaborated a lot on the results of the chapter 5. I'm grateful for all the experiment she performed and for the results that we obtained. She's a great scientist and it was a pleasure for me to work with her. I'm also grateful to **Ahmed-Amine Ouali** for his contribution to this thesis. His work on the different surfactants was helpful and I thank him for his daily inputs and his motivation.

My sincere gratitude also goes to other members of the structure formation group, **Dominik Gerstner**, **Aljosha-Rakim Jochem**, **Thomas Kister**, **Daniel Brodoceanu**, **Axel Bravo Mullto**, **Philip Born**, **Jona Engel**, **Jonas Becker** and **Genesis Ngwa Ankah**. The research publications, conference presentations and the experiment performed at the ESRF in Grenoble would not have been as good without their valuable help, encouragement and feedback.

I am also thankful to **Marcus Koch** for SEM measurement and **Ha Rimbach-Nguyen** for AAS measurement.

The journey of my research would not have been successful without the support, guidance, affection and love of all the individuals who have influenced my life in one way or another.

I am indebted to all my friends, **Flore, Ludo, Nico, Céline, Hak, Núria, Lluís, Daniel, Carina, Dominik and Mélanie** for their friendship and support.

I would like to thank my parents **Francine** and **Antoine**, for their unconditional love and support. They have always encouraged me to pursue my interests in science and engineering and provided me with all possible resources to excel in those endeavors. I am also grateful to my brother **Juju** who has always helped me with informatics and provided me with moral support and enthusiasm, and for the rest of my family (Cécé, Manon, Léa, Christiane, Francis ...) who had to support me during all these years.

Finally, I will always owe my husband **Brice** for giving me the much needed comforting hand and gentle nudges to successfully write my thesis. I'm infinitely grateful for his support, devotion, love and faith. I wouldn't have gone this far without him.

Abstract

The controlled clustering of nanoparticles into defined geometric arrangements has opened a new research area for the design of novel materials with advanced functionalities. This thesis describes a route that exploits liquid droplets as confined templates within which nanoparticles are assembled. Upon removal of the dispersed solvent from the emulsion droplets, the particles formed cluster-like structures. The particles did not arrange into small pieces of dense packings, but resembled clusters predicted for Lennard-Jones interaction potentials. In-situ observation of the assembly process via surface plasmon spectroscopy and small-angle x-ray scattering suggested that assembly occured rapidly, shortly before complete evaporation. The resulting Lennard-Jones geometries represent minimum-energy arrangements of particles. The distribution of the gold nanoparticles in the emulsions was studied for different surfactants. Good surfactants (e.g. Triton X-100) blocked the interface and confined particles in the droplet, whereas others (e.g. Tween 85) formed synergistic mixtures with the nanoparticles at the interfaces. Supraparticles with Lennard-Jones geometries only formed for surfactants that block the interface. The assembly of nanoparticles into minimum-energy clusters was sensitive to interactions between ligands bound to the nanoparticles surfaces, too. The ageing of gold nanoparticles with dodecanethiol ligands was studied for different storage conditions. Surprisingly, fractionation of particles appeared upon ageing. Desorption of ligand was the major process responsible for sedimentation and changes in polarity upon ageing and led to changes in the structure of the supraparticles.

Zusammenfassung

Die kontrollierte Anordnung von Nanopartikeln zu regulären Strukturen ist ein neues Forschungsgebiet für das Design von neuen Materialien mit erweiterten Funktionalitäten. In dieser Arbeit werden Nanopartikeln in die disperse Phase einer Emulsion eingebracht, die dann langsam verdunstet. Nach Verdampfung des Lösungsmittels aus den Emulsionströpfchen bilden die Partikel geordnete Suprapartikeln. Die Struktur dieser Suprapartikeln besteht nicht aus dichten Packungen der verwendeten Nanopartikel sondern es bilden sich geordnete Cluster die mit Lennard-Jones- Wechselwirkungspotential interagieren. In-situ Beobachtung der Anordnung durch UV/Vis-Spektroskopie und Kleinwinkel-Röntgenstreuung zeigt, dass die Anordnung kurz vor der vollständigen Verdampfung auftritt . Wir glauben, dass die resultierenden Lennard-Jones-Geometrie die Anordnung der Partikel mit minimaler Energie darstellen. Die Verteilung von Goldnanopartikel in den Emulsionen wurde für verschiedene Tenside untersucht. Gute Tenside (z. B. Triton X-100) blockieren die Grenzfläche und beschränken Partikeln in den Tröpfen, während andere (z. B. Tween 85) synergetische Mischungen mit den Nanopartikeln an der Grenzfläche bilden. Suprapartikeln mit Lennard-Jones- Geometrie bilden sich nur mit guten Tenside. Die Anordnung von Nanopartikeln in Cluster mit minimaler Energie ist empfindlich gegenber Wechselwirkungen zwischen den Liganden, die an der Nanopartikeloberflächen gebundenen sind. Die Alterung von Gold-Nanopartikeln mit Dodecanthiol-Liganden wurde für unterschiedliche Lagerungsbedingungen untersucht. Dabei tritt eine Partikelfraktionierung auf. Ligandendesorption fürht zu Änderungen der Polarität und zur Sedimentation und zu Strukturänderungen der Suprapartikel.

Contents

Glossary

Acronyms

1D	1 dimension
2D	2 dimensions
3D	3 dimensions
AAS	atomic absorption spectrometry
Au	Gold
AuNPs	Gold nanoparticles
BCC	Body-centered cubic
BCT	Body-centered tetragonal
CdSe	Cadmium selenide
cmc	Critical micelle concentration
Co	Cobalt
CoO	Cobalt monoxide
DLS	Dynamic light scattering
DNA	Deoxyribonucleic acid

EMT	Effective medium theory
ESRF	European synchrotron radiation facility
FCC	Face centered cubic
FC	Icosahedra with an anti-Mackay overlayer
FePt	Iron-platinum
HLB	Hydrophilic-lipophilic balance
HRCS-AAS	High-resolution continuum source atomic absorption spectrometer
IC	Icosahedra with Mackay overlayer
IC*	Icosahedra with Mackay overlayer and a central vacancy
LJ	Lennard-Jones
LSPR	Localized surface plasmon resonance
MD	Complete Marks decahedra
NC	Nanocrystal
NP	Nanoparticle
OA	Oleic acid
O/W, o/w	Oil-in-water
PbS	Lead(II) sulfide
PEGs	Poly(ethylene glycol)s
PMMA	Poly(methyl methacrylate)
PS	Polystyrene
rpm	Rounds per minute
RT	Room temperature

SAMs	Self-assembled monolayers
SAXS	Small-angle X-ray scattering
SDS	Sodium dodecyl sulfate
SEM	Scanning electron microscopy
SPR	Surface plasmon resonance
TEM	Transmission electron microscopy
TOPO	Trioctylphosphine oxide
UV-Vis	Ultraviolet-visible
W/O, w/o	Water-in-oil

Symbols

a	Optical absorptivity of the particles
$\mathbf{A}$	Hamaker constant
$A_f(t)$	Maximal absorbance of filtered particles at time t
$A_f(t_0)$	Maximal absorbance of filtered particles after synthesis
a_l	Lattice constant
A_{SPR}	Peak absorbance
A_{w1}	Peak absorbance of fresh dispersions
c	Velocity of the light
C_{ext}	Extinction cross-section
c_i	Concentration of fraction i of particles
c_0	Total filtered particle concentration
D	Diffusion coefficient of the particles
$\Delta\lambda$	Surface plasmon peak shift
Δp	Pressure difference
Δp_0	Pressure difference at time t_0
$\Delta\rho$	Density difference between the two phases
d_{LUM}	Dilution factor for sedimentation experiment
d_{uv}	Dilution factor for UV-Vis experiment
E	Energy required to remove a particle from the interface
ϵ	Dielectric constant
ϵ_{eff}	Effective dielectric constant

ϵ^{∞}	Dielectric constant of the particles
ϵ_m	Dielectric constant of the solvent
ϵ_0	Vacuum permittivity
ϵ_r, ϵ_i	Real and imaginary components of the dielectric function
η_c	Dynamic viscosity of the continuous phase
f	Packing density
$F(q)$	Particle form factor
g	Gravitational acceleration
Γ	Linewidth of the scattered light
γ_{ow}	Interfacial tension at the oil/water interface
γ	Interfacial tension
γ_e	Electron collision frequency
$g(\tau)$	Autocorrelation function
h,k,l	Miller indices
I_M	Average mass of the clusters
$I(q)$	Scattering intensity
k_B	Boltzmann constant
k_i	Diffusion vector
l	Path length of the absorbing medium
λ	Wavelength
λ_{max}	Peak wavelength
λ_p	Bulk plasmon wavelength

m_e	Effective mass of electrons
μ	Viscosity of the solvent
n	Refractive index of the medium
N	Concentration of free electrons in the metal
ω	Bulk plasma frequency
ω_p	Bulk plasma frequency of a metal
p	Power-law exponent related to the fractal dimension of the clusters
Pe	Peclet number
ϕ	Volume fraction
$\phi_{filtered}$	Mass fraction of filtered particles
ϕ_{stab}	Mass fraction of filtered particles stable upon addition of 1-propanol
ϕ_{unstab}	Mass fraction of filtered particles unstable upon addition of 1-propanol
q	Scattering vector
q_c	Scattering vector at peak maximum
R	Radius of the droplet
R_1, R_2	Radii of curvature of the drop
R_H	Hydrodynamic radius
r	Radius of the nanoparticles
$S_{eff}(q)$	Effective structure factor
σ	Standard deviation
$S(q)$	Stucture factor
T	Temperature

t_{end}	End time of the separation process
θ	Scattering angle
τ	Time required for a droplet to evaporate
T_{end}	Final transmission for the mixture of filtered particles and 1-propanol
T_{max}	Maximum transmission of the cuvette containing pure solvent
T_0	Initial transmission for the total filtered particle concentration
t	Evaporation time
v	Stationary velocity of the drop
$V(x)$	Interaction potential
x	Center-to-center distance separating two spheres
ξ	Correlation length correspondinf to the average size of the clusters

List of Figures

List of Tables

Chapter 1

Introduction

Colloidal nanoparticles are of great interest for researchers from a wide range of disciplines, including materials science, chemistry, physics, and engineering, because of their unique magnetic, electronic and optical properties. Among all kind of nanoparticles, gold is one of the first historically and simplest metallic chemically particles and also relatively stable. The unique optical attributes from their plasmon resonance result in a large enhancement of the electromagnetic field around the nanoparticles. Strong light absorption and scattering of the nanoparticles at the plasmon frequency can be tuned by changing the nanoparticle size, shape, composition or environment and has already found uses in several optical and medical applications [1–4].

The synthesis of nanoparticles is already well known, however the assembly of nanoparticles into ordered structures is still under development and improvement [5–7]. Recently, the focus has been directed towards the creation of ordered structured from colloidal nanoparticles, which holds great promise for the development of advanced materials with novel integrated functions [8]. Ensembles of nanoparticles can display new electronic, magnetic and optical properties as a result of interactions between the individual nanoparticles which can be exploited in devices by controlling the spacing and arrangement of the nanoparticles.

Ensembles of nanoparticles have been used as nanoscale thermometers, pH meters [9] and as biological and chemical sensors [10–12]. Plasmon-based sensors were developed for the detection of oligonucleotides where a change of colour occurs when nanoparticles-DNA conjugates undergo assembly mediated by hybridisation of DNA with target oligonucleotides [10]. Data storage devices have been developed using self-assembled nanostructures of platinum nanoparticles [13]. The device shows memory operations, such as data retention, operated voltages and cycle ability. Arrays of self-assembled magnetic FePt nanoparticles present also some applications in this area [14]. 3D superlattices of FePt nanoparticles are used for data recording at linear densities of up to 5,000 flux changes per millimetre.

Certain applications require defined 3D arrangements of nanoparticles. The preparation of 3D aggregates with controllable size, shape and composition usually require the use of a template. A broad range of objects such as carbon nanotubes [15], block-copolymers [16], viruses [17] or DNA molecules [18], polymer capsules [19–21] or emulsion [22–26] can be used as templates for nanoparticle assembly [27]. The confinement of nanoparticles inside a template leads to the arrangement of nanoparticles where the structure is predefined by the shape of the template. For example, polystyrene-b-poly(methyl methacrylate) films were used as templates to assemble CdSe nanorods on the surface of cylindrical or lamellar poly(methyl methacrylate) [28]. PbS nanoparticles were also assembled on the surface of cylindrical block polyferrocenylsilane-b-poly(2-vinylpyridine) comicelles [16]. Anionic PbS nanoparticles were deposed by electrostatic forces onto the positively charged 2-vinylpyridine fragments.

Many methods developed for the formation of 1D, 2D or 3D nanostrustures are complex (such as lithography-based technique) and requires sophisticated experimental equipment and high costs to achieve sub-100 nm ordered structures. This thesis describes the use of emulsion droplets, a low-cost and easy to manipulate template to form 3D nanoparticle clusters. Emulsion droplets are convenient templates to confine and combine particles into supraparticles by evaporating the disperse solvent [22–26]. Emulsion-based method were previously used for the assembly and encapsulation of particles [22–26, 29, 30]. Velev et al. showed how particles were gathered, assembled and fixed together in the restricted volume provided by emulsion droplets [22, 23]. The system is governed by the interactions between the particles and the droplet interface. The hydrophobic character of the particles is a key parameter in this system. The control of the number of particles per droplet is an interesting aspect to be considered for the preparation of small aggregates with defined size and order. A method developed by Manoharan et al. shows how defined clusters can be formed when microparticles are dispersed in the oil phase of an emulsion [29, 30]. The final size and shape of the clusters depend mainly on the number of particles per drop.

This thesis was motivated by the results of Manoharan. My main goal was to form ordered supraparticles from nanoparticles using emulsion as a template.

Even when the internal structure of assembled nanoparticles in bulk is perfectly defined, the overall shape and size is not because it depends on the process details and cannot be controlled in the current techniques. The process used here combines controlled confinement with superlattice formation. Particle agglomeration takes place in the confined spaces of an emulsions' dispersed phase. This approach avoids the limitations of chemical linkers that can be used to define clusters from small numbers of particles but is unreliable, synthetically demanding, and requires a new process for each desired geometry. The technique employed here mainly requires high-quality emulsions with control over interfacial effects.

The **first chapter** introduces fundamental knowledge on nanoparticles and emulsions. The parameters that define and influence their properties and structure or stability are presented.

Chapter 2 describes the experimental techniques and the instrumentation, as well as the synthesis and characterisation of nanoparticles and emulsions.

Chapter 3 introduces results of the emulsion-based method for the assembly of gold nanoparticles. The first section summarizes existing literature related to the subject. Then the results of nanoparticle assembly using an emulsion droplet are presented. Nanoparticle clusters with defined geometries can be formed inside emulsion droplets when the oil phase is slowly evaporated. The mechanism that governs the formation of such supraparticles are studied. In situ observation of the assembly process via surface plasmon spectroscopy and small-angle x-ray scattering are performed in order to determine which routes lead to the formation of such clusters.

When working with emulsion, the interaction of particles and surfactant at the interface has to be considered and can influence the stability and properties of the emulsion. These parameters can then influence the resulting shape and structure of the supraparticles formed using the emulsion droplets. The effect of different surfactants on supraparticles formation are presented in **Chapter 4**. The distribution of gold nanoparticles inside the different hexane-in-water emulsions is presented for different surfactants.

Chapter 5 presents results on the ageing of gold nanoparticles stabilized by dodecanthiol in an unpolar solvent. UV-Vis spectroscopy was used to observe the behaviour of the suspension over time under different storage conditions. Precipitation was performed using an analytical centrifuge to identify the structural changes that occur during storage. Finally, the influence of ageing of the formation and structures of the supraparticles formed inside emulsion droplets are presented.

Finally, **chapter 6** summarizes the findings of this work and provides an outlook on future extension of the work.

Chapter 2

Theoretical considerations

Some knowledge on nanoparticles and their properties is needed when working on the formation of superstructures. This chapter introduces concepts on nanoparticles, their stability and their optical properties. In a second part, emulsions and their formation routes are discussed. We define, in a first step, the term emulsion and the properties of such a system. This section will also mention the choice of emulsifier and the importance of stability for the formation of emulsions studied here. Pickering emulsions are then introduced. Their particularities and different aspects compared to surfactant are presented here. Finally, an overview of colloidal assembly is presented.

In this chapter, only very general concepts necessary for understanding of the overall thesis work will be discussed. When necessary, more specific concepts will be presented later.

2.1 Gold nanoparticles

Nanoparticles have attracted mcuh interest due to their optical or magnetic properties that significantly differ from bulk properties. The optical properties of nanoparticles have been used since the Middle Ages by glassmakers who tinted their glass in multiple colors using gold particles of different nanometric size. A good example is the "Lycurgus cup" which, as shown in Figure 2.1, shows variations of colors depending on where the light is applied. The chalice appears green in reflected light, but when illuminated from the inside, it appears red.

Figure 2.1: Roman Lycurgus cup - Photographs of the cup taken with two different perspectives: in reflected (left) and transmited light (right). From the department of prehistory and Europe, the British museum.

Through the work of Zsigmondy and Svedberg, it turned out that the color of the ruby glass or other glasses, depends on nanoscale inclusions from noble metals which are formed during the manufacturing step of the glasses. They succeeded in characterising nanoparticles in liquid colloidal system and could determined cluster size below 10 nm by optical means. Even today, this technique consisting of incorporating nanoparticles in the glass paste is used to stain luxury perfume bottles, such as "Fahrenheit" Christian Dior.

2.1.1 Surface plasmon resonance of metallic nanoparticles

Size, shape and environment of metal nanoparticles have an influence on their optical properties due to their unique interaction with light. Maxwell-Garnett [31] and Mie [32] have demonstrated that the coloration of these glasses referred previously is induced by their metallic inclusions.

The optical response (absorption and scattering) of colloidal particles to an electromagnetic field can be described by its dielectric constant $\epsilon = \epsilon_r + i\epsilon_i$, where ϵ_r and ϵ_i are the real and imaginary components of the dielectric function, respectively. For very small particles with $r \ll \lambda$ in a medium of dielectric function ϵ_m, the scattering cross-section is negligible and the extinction cross-section is dominated by absorption given by the equation [33, 34]:

$$C_{ext} = \frac{24\pi^2 r^3 \epsilon_m^{3/2}}{\lambda} \frac{\epsilon_i}{(\epsilon_r + 2\epsilon_m)^2 + \epsilon_i^2}. \tag{2.1}$$

The maximal absorption thus occurs at the "plasmon resonance frequency" where

$$\epsilon_r = -2\epsilon_m, \text{ and } \epsilon_i \text{ very small.} \tag{2.2}$$

The resulting absorption peak in the visible frequency range is the origin of intense colors displayed by metallic nanoparticles. The Mie theory thus predicts the plasmon peak position to be determined mostly by ϵ_r while the peak height and shape is governed by ϵ_i. The negative index means that the plasmon oscillates out of phase with the electric field. Since ϵ_i can be neglected, the maximal absorption depends only on the real part of the dielectric constant.

In metallic nanoparticles, there are electrons that can be considered to move rather freely in the crystal lattice and free electrons respond to the oscillation of an external electromagnetic field in a collective way.

The external field exerts an oscillating force on the electrons and ions constituting the metal nanoparticle. The electron gas formed by the electrons of the conducting band will therefore move collectively creating an accumulation of positive and negative charges on the surface of both sides of the nanoparticle (see Figure 2.2). A restoring force takes place in response to the exciting field on the retroactive movement of electrons. The system may experience a resonance condition where the collective oscillation of the electron gas around its equilibrium position is at the same frequency as the excitation field. The phenomena of the electric field inside the nanoparticle are then enhanced. Absorption is enhanced, and oscillating dipole created by the accumulation of charges, radiates with a maximum intensity at the plasmon resonance frequency ω_{spr}.

This plasmon resonance frequency depends on many parameters such as composition, size and shape of the metallic nanostructures, and their chemical environment [35, 36].

For some transition metal nanoparticles, like gold, silver and copper, plasmon resonance appears in the visible region of wavelengths and can be observed as an absorbance band in the optical spectrum.

Assuming a free electron behaviour for the metallic particle, the real part of the dielectric function of metallic particles can be described using the Drude model as a

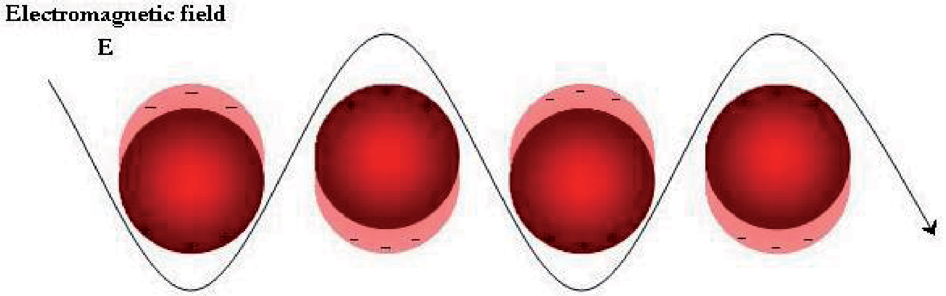

Figure 2.2: Surface Plasmon Resonance - Schematic illustration of the surface plasmon resonance oscillation of electrons of a metal nanoparticle resulting in the strong enhancement of the electric field.

function of the frequency ω:

$$\epsilon_r = 1 - \frac{\omega_p^2}{\omega^2 + \gamma_e^2}, \tag{2.3}$$

where γ_e is the electron collision frequency. The bulk plasma frequency of a metal ω_p, defined as the frequency of bulk plasma oscillations in the metal, is expressed in terms of the concentration of free electrons N in the metal, the effective mass of electrons m_e and the vacuum permittivity ϵ_0:

$$\omega_p^2 = \frac{Ne^2}{m_e \epsilon_0}. \tag{2.4}$$

The Drude model for the dielectric function describes a free electron gas and is sufficient for metals such as aluminium. However, for noble metals such as gold or silver, the dielectric function has to be modified by a contribution ϵ^∞ that covers the effect of interband transitions. The criterion for plasmon resonance then becomes for $\gamma \ll \omega$:

$$\epsilon_r = \epsilon^\infty - \frac{\omega_p^2}{\omega^2}. \tag{2.5}$$

Using this condition, we obtain the plasmon resonance frequency ω_{spr} [33, 34]:

$$\begin{aligned} \omega^2 &= \frac{\omega_p^2}{\epsilon^\infty - \epsilon_r} \\ &= \frac{Ne^2}{m_e\epsilon_0(\epsilon^\infty + 2\epsilon_m)} \\ \omega_{spr} &= \sqrt{\frac{Ne^2}{m_e\epsilon_0(\epsilon^\infty + 2\epsilon_m)}} \qquad (2.6) \end{aligned}$$

where ϵ_m is the dielectric constant of the medium and c is the velocity of light.

2.1.2 Influence of different parameters on the optical properties of metallic nanoparticles

2.1.2.1 Nanoparticle size

The size of the nanoparticles also influences the surface plasmon resonance. As the radius of the nanoparticles appears in the equation of the absorption cross section (equation 2.1), Mie theory predicts a size dependence of the intensity. The peak position and peak width are also affected by the nanoparticle size, but through intrinsic effects. Many theories have been studied to correlate the size to the surface plasmon peak position and finally experimental results showed that a blue shift occurs when decreasing the NPs size (see figure 2.3)[37].

2.1.2.2 Nanoparticle geometry

Confinement and displacement of the conduction electrons depends on the shape of the particle. Consequently the optical response is very sensitive to the geometry of the particle. Figure 2.4 illustrates this behaviour. When the length of a nanorod increases, the optical properties change considerably. Two absorption bands are observed: a strong peak near the infrared region correpsonds to the electron oscillations along the longitudinal direction while a weaker peak which corresponds to oscillations in the transverse directions. The longitudinal peak is very sensitive to the length of the rods.

A relevant change of optical properties is also observed experimentally for Ag prisms with different curvature (Figure 2.4(b))[38, 39]. Indeed the transition from perfectly triangular nanoplate to circular particles is accompanied by a widening and offset toward the longer wavelengths.

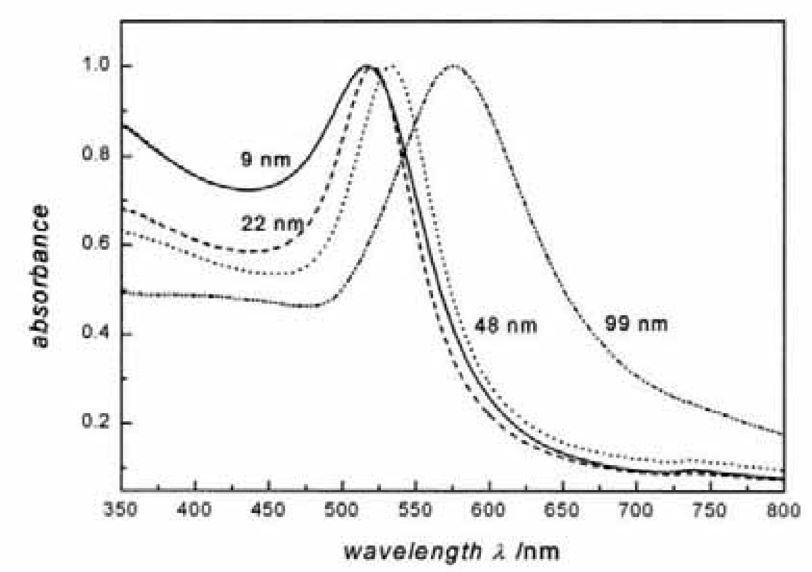

Figure 2.3: UV-Vis absorption spectra of gold nanoparticles of different sizes - The size of the Au nanospheres decreases from 99 nm to 9 nm. As the size decreases, a blue-shift of the surface plasmon resonance peak is observed. *Image from Link and coworkers [37]*

2.1.2.3 Nanoparticle environment

The plasmon resonance frequency is sensitive to the dielectric properties of the surrounding medium of the particle. As described in equation 2.6, the plasmon resonance frequency is related to the dielectric constant of the medium. An increase in the medium dielectric constant results in a decrease of the plasmon resonance frequency and hence a red-shift (or increase) of the plasmon resonance wavelength since :

$$\lambda = \frac{2\pi c}{\omega}. \tag{2.7}$$

Changing the medium surrounding the NPs for another medium having a different refractive index strongly alters the plasmon behaviour of the NPs as observed in figure 2.5 [41]. Fifteen years ago, Mulvaney described how the refractive index of the solvent can influence the position of the surface plasmon band [36, 41].

Figure 2.6 shows that the position of the surface plasmon resonance peak depends on the refractive index of the medium. Mulvaney and others suggested that the position

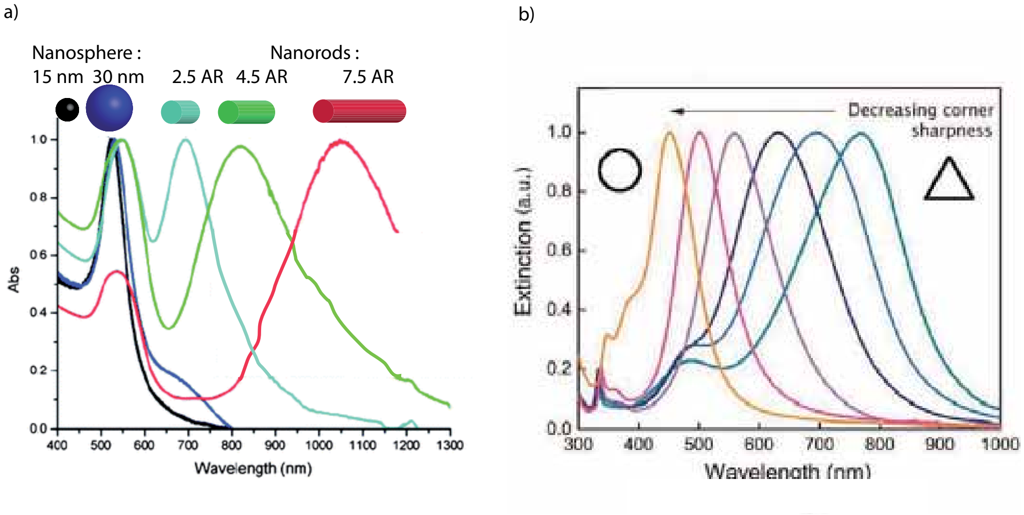

Figure 2.4: UV-Vis absorption spectra of nanoparticles of different shapes - (a)Extinction spectra of Au nanoparticles whose shape vary from nanospheres to nanorods. In the case of nanorods we observed two peaks corresponding to oscillations along the longitudinal direction (strong peak at high wavelength) and oscillations in the transverse direction (weaker peak at lower wavelength). *Adapted from Eustis and Elsayed [40]* (b) Extinction spectra of Ag triangular nanoplates with decreasing corner sharpness. The decreasing corner sharpness is correlated with a blue-shift in the extinction spectra of the nanoparticles in solution. *Image from Rycenga and coworkers[39]*

Figure 2.5: Color change due to a different medium - Changing in the plasmon peak position induced by varying the solvent refractive index. Refractive indices of the solutions at the absorption band maximum are 1.336, 1.407, 1.481, 1.525 and 1.583, respectively. *Image from Underwood and Mulvaney [41]*

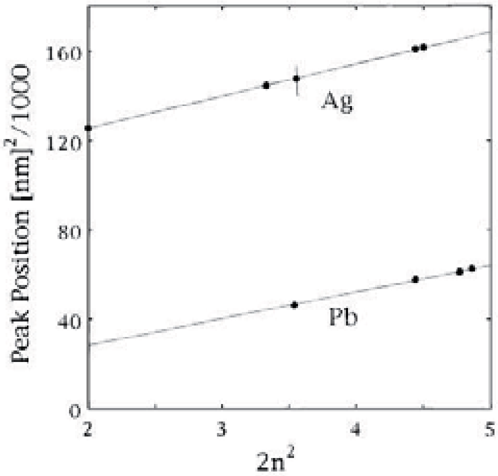

Figure 2.6: Effect of the solvent refractive index on the Surface Plasmon Resonance - Position of the surface plasmon bands of colloidal lead and silver as a function of the medium dielectric function. *Image from Mulvaney [36]*

of the surface plasmon band may be used to measure the local dielectric constant in microheterogeneous systems [36, 42].

2.1.3 Stability of the nanoparticle suspension

An important aspect to be considered when using nanoparticles in solution, is the dispersions state, and especially its stability, which must be maintained.

The behaviour of colloidal suspensions is determined by the forces between particles. On one hand, Van der Waals attractions interacting with Brownian motion, provoke flocculation of the particles. On the other hand, repulsive interactions prevent aggregation of particles with induced kinetically stable suspensions. The sum of these two forces determines the particle stability.

We distinguish two types of repulsive forces. The first type is electrostatic repulsion induced by identical charges on the surface of the particles which can be found for colloids suspended in the aqueous phase. A typical example is the stabilisation of gold NPs prepared by citrate reduction following the Turkevich method [43]. In this case, gold NPs are stabilized by an electric double layer composed of bulky citrate ions, chloride ions and the cations attached to them. The interaction potential between two colloids, taking into account the Van der Waals interactions and electrostatic repulsion forces was first calculated by Derjaguin and Landau and later on by Verwey and Overbeek forming the DLVO model [44, 45].

The second type of repulsion forces are steric interaction where particles are covered by uncharged polymers. In good storage conditions, the adsorbed polymers represent a steric barrier that maintain the stability of the colloidal dispersion.

The nanoparticles used in this work are stabilized by steric repulsions induced by the presence of a ligand on the surface of the particles. Knowing that, the repulsion induced by electrostatic forces is not developed further in the thesis.

2.1.3.1 Van der Waals attraction forces

The Van der Waals attraction between colloidal particles dispersed in a solvent results from the interaction between the particles and the continuous phase. When the distance between particles is larger, the time required for the polarisation of a particle by another becomes large, particularly as the speed of light in the solvent is lower than in vacuum. These effects make the exact calculation of the interaction between two macroscopic bodies difficult. Nevertheless, assuming additivity of interactions and neglecting the effects of time delay related to polarisation and the solvent, we can calculate the interaction potential $V(x)$ between two spheres of radius r and density ρ, and separated by a distance x (center to center):

$$V(x) = -A\frac{r}{12(x-2r)}, \tag{2.8}$$

where A is the Hamaker constant which depends on the chemical nature of the particles and the continuous phase. The Van der Waals interaction between the particles is generally effective in the range of a few nanometers. Hamaker constant is always positive for two bodies of the same chemical nature (attractive interaction), but may be negative for two bodies of different chemical nature (repulsive interaction).

2.1.3.2 Steric stabilisation

A method to stabilize colloidal suspensions is to add polymers to the surface of the colloids. When two particles with adsorbed polymer layers approach each other at a distance of less than twice the thickness of the adsorbed layer, interaction of the two layers takes place.

The repulsive forces depend on the degree of coverage of the surface and the solvent quality.

- A decrease in surface coverage will lead to a decrease of particle stability. Particles only partially coated by polymer may undergo irreversible coagulation caused by Van der Waals attraction between the core particles.
- The quality of the solvent also affects the repulsive interactions. If the solvent affinity with the adsorbed polymer layer is good, the polymer chains can extend and the sphere of influence will be big enough to maintain stability. However, if the solvent affinity is poor, the polymer chains will tend to interpenetrate into those of a layer on another particle and thereby promote aggregation.

2.1.4 Importance of optical properties and stability of the suspension

The optical properties of metallic nanostructures have also been the focus of intense scientific study. The assembly or aggregation of metallic nanoparticles results in a red-shift of the plasmon extinction wavelength maximum from that of isolated nanoparticle as well as a peak broadening. This is also evidenced by a visual color change (i.e. from red to purple for gold nanoparticles). The magnitude of the red shift due to aggregation is controlled by several factors where the most important are aggregate size, the interparticle distance and the particle size. Many studies, experimental and theoretical [46], have investigated the optical properties of one and two-dimensional (2D) arrays of fcc metal nanoparticles. The plasmon shift gives a measure of the distance between the particles. Sonnichsen et al. utilized this recently to design a **plasmon ruler** to measure nanoscale distances in biological systems on the basis of the spectral shift resulting from the coupling of two gold nanoparticles by a defined biomolecular binding scheme [47]. The plasmon ruler was developed in the case of dimers composed of metallic gold nanoparticles, as an analytic expression for the dependence of the LSPR wavelength shift as a function of nanoparticle size and the gap between the nanoparticles [48–50]. From the previously mentioned results, SPR can be used as an analytical tool for agglomeration studies since SPR shift can well describe the assembly of metallic particles.

The ligand and solvent influence the stability and assembly of nanoparticles. The choice of the solvent and the density of ligand at the surface of the particles have an impact on the steric repulsions and on the stability of the suspension. A good solvent is a prerequisite for stabilizing the suspension [51]. Theses parameters have to be taken into account when performing an assembly process since they can influence the interaction forces that are present in the suspension and hence influence the forces needed for the assembly process. Recently, Born et al. demonstrated that ligand-solvent interactions of the individual nanoparticles dominate suspension stability and agglomeration kinetics [52]. By varying temperature and changing ligand chains lengths of thiol-capped gold NPs, the suspension was destabilized and formed agglomerates.

2.1.5 Morphologies of agglomerates

The ligand and solvent influence the assembly of nanoparticles. Experiments supported by simulations demonstrate that the final morphology of nanoparticles assemblies depends on the solvent used [52–54]. Pileni and co-workers carried out both experimental and theoretical studies on the influence of the NP sizes (4 to 7 nm) in nonpolar solvents (cumene, hexane, octane, and toluene) on the growth of 2D ordered assemblies of 1-dodecanethiol-capped gold NPs via solvent evaporation. They suggest that the structure formation is mainly driven by solvent-mediated interactions and not solely by the Van der Waals attraction between the particles [53]. Born et al. demonstrated that ligand-solvent interactions of the individual nanoparticles influence the morphology of the agglomerate by varying temperature and ligand chain lengths of thiol-capped gold NPs [52]. Both experiments and a simple physical model for monolayer-protected AuNPs have also suggested that ligand-ligand interactions can induce AuNP aggregation [55]. They demonstrated that disordered and ordered agglomerates of the same alkyl thiol-coated gold nanoparticles depends on temperature and solvent. They explained that order occurs only above the melting temperature of the ligand shells and is governed by the contact mechanics of the ligand shells.

Ligand-ligand and ligand-solvent interactions dominate suspension stability and have to be taken into account during assembly since they also influence the agglomeration kinetics.

2.2 Emulsions

Emulsions are dispersions of one liquid in a second immiscible liquid. In an emulsion, the dispersed phase consists of liquid droplets and the continuous phase of a liquid medium in which the liquid droplets are dispersed. They can be classified based on their morphology: Emulsions that have water as the continuous phase and oil as the dispersed phase are called oil-in-water (O/W) emulsions. When water is the dispersed phase, it is called water-in-oil (W/O) emulsions or inverse emulsion. Emulsions are thermodynamically unstable systems, energy is required to disperse the droplet phase into the continuous phase.

Emulsions can be stabilized by the presence of a molecule or particle. The emulsifier (molecule or particle) will stabilize the emulsion by creating a physical barrier between the two phases and reducing the interfacial tension. According to the nature of the liquids and the expected stability, the emulsifier will be chosen. There are multiple classes of emulsifiers: ionic or nonionic surfactant, polymers, surfactant mixtures, or solid particles.

2.2.1 Emulsion stability

Emulsions undergo destabilisation after a period of time. The drops formed undergo several processes that tend to bring the system to its lowest state of energy corresponding to two separated phases with a minimum area of contact between them [56]. Therefore, a minimisation of interfacial area can be obtained by aggregation processes such as flocculation, sedimentation, coalescence, coagulation and Ostwald ripening. Those destabilisation phenomena are presented in figure 2.7.

Creaming (migration of the dispersed phase up to the solution) or **sedimentation** (downward migration of the dispersed phase) are reversible destabilisation phenomena of emulsions, since the agitation of the solution allows the redispersion of the droplets. These two phenomena are due to the density difference between the two phases and is a form of gravitational separation. The stationary velocity during phase separation is governed by Stoke's law:

$$v = \frac{2}{9}\frac{\Delta\rho \cdot g \cdot r^2}{\eta_c} \tag{2.9}$$

– v is the stationary velocity of the drop ($m.s^{-1}$)

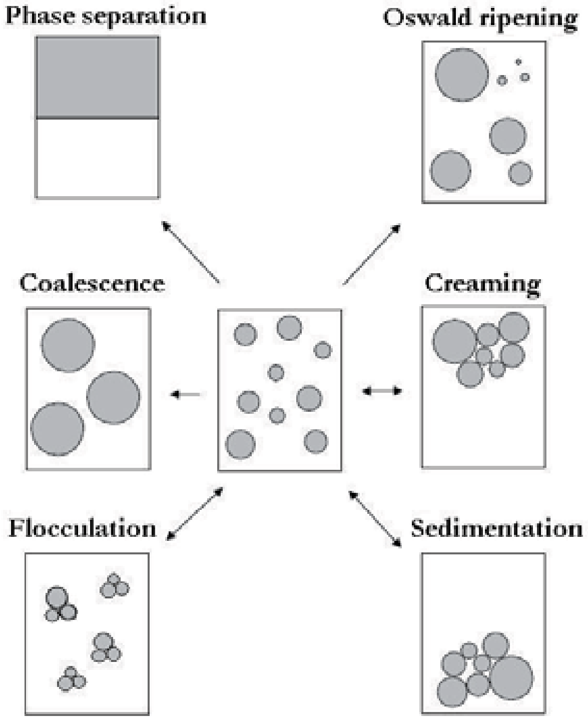

Figure 2.7: Destabilisation phenomena of an emulsion - Creaming, sedimentation and flocculation are reversible phenomena whereas phase separation and coalescence are irreversible phenomena. *Adapted from Tadros[57]*

- g is the acceleration due to gravity ($m.s^{-2}$)
- $\Delta\rho$ is the difference between the densities of the different phases ($kg.m^{-3}$)
- r is the drop radius (m)
- η_c is the dynamic viscosity of the continuous phase ($Pa.s$)

The rate of creaming (or sedimentation) is proportional to the square of the radius. Decreasing the diameter of the droplets can considerably decrease the migration velocity. In the case of nano-emulsions, where the diameter is smaller than 100 nm, Brownian motion (which describes the random motion of a particle in a fluid) dominates gravity and keeps the droplets almost evenly distributed throughout the emulsion.

Another reversible phenomena is the **flocculation** of the droplets without change of the droplets size [58]. It may occur when the attraction forces between droplets (e.g. Van der Waals forces) are stronger than the repulsive forces. To prevent this process, one solution is to increase the repulsive forces between droplets by introduction of an electrostatic repulsion with the addition of ionic surfactants or a steric repulsion with the addition of non-ionic surfactants.

Even though the previously mentioned phenomena are reversible, they promote coalescence, which is an irreversible process. Other processes induce an increase in the size of the droplets of the emulsion, and are hence irreversible: coalescence and Oswald ripening.

Coalescence is the rupture of the surfactant film separating two droplets, resulting in the fusion of these two droplets (as shown in figure 2.8) [58]. The stiffness of the interfacial layer is the key to the droplet coalescence, which creates an energy barrier that has to be overcome before the thermodynamic stable state is reached. Therefore, it is necessary to introduce a strong interfacial layer in order to enhance the emulsion stability. Coalescence often happens when the droplets are in a very close distance. At this point, the attractive force is greater than the repulsive force and causes failure of the interfacial layer inducing the fusion of the droplets.

Ostwald ripening occurs when the dispersed phase is slightly soluble in the continuous phase. In this case, the Laplace pressure which is larger in droplets of small diameter, will force the solubilisation of molecules of the dispersed phase in the continuous phase, which will then be preferentially assimilated by the larger droplets (because the Laplace pressure is lower) as illustrated in figure 2.8. The transfer between the droplets of the dispersed phase takes place by molecular diffusion through the continuous phase.

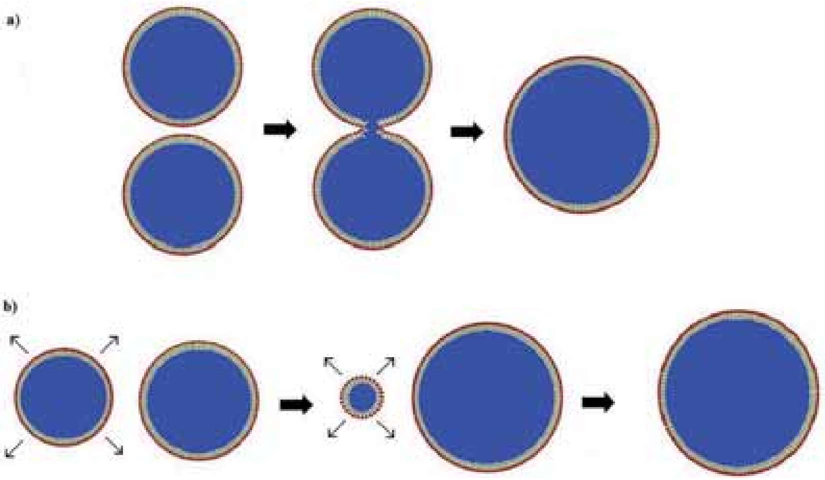

Figure 2.8: Schematic of the coalescence and Ostwald ripening process - a) When two droplets are close and the interfacial layer is thin, it can break, resulting in the fusion of the two droplets. b)Ostwald ripening occurs when the dispersed phase is (slightly) soluble in the continuous phase. The Laplace pressure differential will cause a migration of small droplets into the larger one.

Ostwald ripening thus results in a decrease in the diameter of the smaller droplets up to their complete disappearance and an increase in the diameter of the largest ones.

All these destabilisition phenomena have to be taken into account during emulsification. Three main processes occur simultaneously during emulsification: the dispersed phase breaks up and droplets are formed, emulsifier molecules are adsorbed onto the formed droplets and droplets encounter each other. Despite the fact that emulsions exist in a thermodynamically unstable state, they can remain kinetically stable for months or years. One important destabilisation process that can occur in this study is creaming. There are many ways to reduce creaming [59, 60]:

- reduction of the droplet size can be achieved by efficient homogenisers or by using adequate emulsifiers to prevent droplet coalescence,
- minimisation of the density difference between the two phases which can be achieved by adding a weighting agent to the oil phase or using highly dense emulsifiers,
- increase of the continuous phase viscosity can be achieved by a gelling agent introduced in the continuous phase,
- increase of the droplet concentration which will minimize the movement of the droplets.

Due to Brownian motion, gravity and mechanical agitation, emulsions droplets are constantly moving and can collide with each other. By doing so, they will either move apart or aggregate leading to coalescence. This phenomenon consists of the nucleation of a thin channel between two droplets [56, 58]. The formation of this channel requires a certain level of energy, which determines the nature of the droplet collisions. At high energy level, there is no aggregation and the droplets will move apart. However, at low energy level, droplets are strongly flocculated leading to the creation of a channel between the droplets. The energy barrier is so low that the channel will grow resulting in droplets coalescence. The rate at which the channel forms is also of great importance to predict coalescence. Emulsion droplets are moving constantly and so collision time may be very short. However, if this time is long compared to the time required for the formation of the connecting channel, coalescence may occur. Coalescence is also largely dependent on the properties of emulsifiers adsorbed at the droplets interface. Emulsifier molecules form a layer around the droplets that protects them from coalescence. The concentration of emulsifier must be high enough to completely cover the surface of the droplet. Moreover, the time required for the emulsifier to adsorb at the interface is also an important parameter. In order to minimize the coalescence during the emulsification process, the time required for the emulsifier to adsorb at the interface should be lower than the time required for droplet collisions.

2.2.2 Choice of emulsifier

To prevent destabilisation of the emulsion, we have to introduce an emulsifier capable of stabilizing the droplets formed. There are multiple types of emulsifiers, the most common being amphiphilic molecules called surfactants. Emulsions can also be stabilized by solid particles, leading to emulsions called "Pickering emulsions" which will be discussed in more details later [61]. Surfactants, also called surface-active agents, contain two groups, a hydrophilic group which is water soluble, and a lipophilic group which is oil soluble. All emulsifying agents are adsorbed onto the oil-water interface to provide a protective barrier around the dispersed droplets. In addition to this protective barrier, emulsifiers stabilize the emulsion by reducing the interfacial tension of the system. Some agents enhance stability by imparting a charge on the droplet surface thus reducing the physical contact between the droplets and decreasing coalescence. Surfactants can be classified in four different groups depending on the nature of their hydrophilic part:

- anionic surfactants, where the hydrophilic part is negatively charged,
- cationic surfactants, where the hydrophilic part is positively charged,
- zwitterionic or amphoteric surfactants, where the hydrophilic part has two oppositely charged groups,
- nonionic surfactants, where the molecule has no charge.

The selection of a surfactant in the preparation of emulsions is often made on an empirical basis. There are different models which can be used to choose a surfactant. The simplest one is the Bancroft-rule which is related to the surfactant solubility. Whether a molecular surfactant preferably stabilizes oil-in-water (O/W) or water-in-oil (W/O) emulsions, is determined by the surfactants solubility. The phase in which the surfactant is preferably soluble normally forms the continuous phase [62].

Another model was presented by Griffin [63, 64]. He introduced the Hydrophilic-Lipophilic-Balance (HLB) value for the empirical description of the surfactant orientation at the interface. It corresponds to the relative percentage of hydrophilic to hydrophobic groups in the surfactant. The HLB-value is a dimensionless number between 0 and 20, where values of 0 to 8 are characteristic of an oil soluble surfactant and HLB-values between 10 and 20 are characteristic of a water soluble surfactant.

HLB range	Application
3-6	w/o emulsifiers
7-9	wetting agents
8-18	o/w emulsifier
13-15	detergents
15-18	solubilizing agent

Table 2.1: HLB ranges and their applications - Overview of class of surfactant according to their HLB value

By applying the HLB system, one will be able to obtain an indication of what type of emulsifier to choose according to the system that he wants to obtain (production of W/O emulsion, O/W emulsion, choice of detergent or solubilizing agent). As detailed in Table 2.1, an emulsifier that is hydrophilic is assigned with a high HLB-value (above 8.0) whereas one that is lipophilic is assigned with a low HLB-value(below 9.0).

Regardless of their classification, all emulsifying agents must be chemically stable in the system, inert and chemically non-reactive with other emulsion components.

2.2.3 Pickering emulsions

Emulsions stabilized by solid particles are called Pickering emulsions and consist of dispersions of two immiscible liquids stabilized by solid particles. They are known for about a century and were first identified by Ramsden in 1903 [65] and described more in detail by Pickering in 1907 [61]. Pickering observed that particles can act as stabilizers for foams and emulsions by adsorbing to the interface. A dense layer of particles residing at the oil-water interface prevents the coalescence of droplets.

The stability of Pickering emulsions is related to the adsorption of particles at the interface between the immiscible phases. Solid particles, just like molecular surfactants, generally follow the Bancroft rule: the continuous phase is the one in which the particles have the greatest affinity. An o/w emulsion will be stable if the particles are soluble in water and vice versa a w/o emulsion is stable if the particles are soluble in oil. However, the mechanisms of stabilisation involved are very different from emulsion stabilized by surfactants. Numerous types of particles can be used for Pickering emulsions [66, 67].

The particles are not necessarily solid: effective stabilisation has been observed with microgels, liquid crystals, but also with natural particles such as bacteria and spores [68, 69].

The excellent stability of Pickering emulsions is particularly attractive for pharmaceutical and cosmetic applications. The assembly of nanoparticles at fluid interfaces can form a solid shell around the droplets, which allows the encapsulation of a molecule, as described by Simovic and Prestidge [70]. They show that the release kinetics of the encapsulated active agent is controlled by the density of the adsorbed layer [70]. The amount of particles at the interface can be changed depending on the hydrophobicity of the particles or the presence of salt in the solution.

The efficiency of the stabilisation depends mostly on the characteristics of the particles, namely, their size, shape, concentration and capacity to be hydrophobic or hydrophilic. The hydrophobicity is characterized by the contact angle θ_{ow} between the aqueous phase, the oil phase and the particle [71]. The value of the contact angle determines the position of the particle at the interface (figure 2.9).

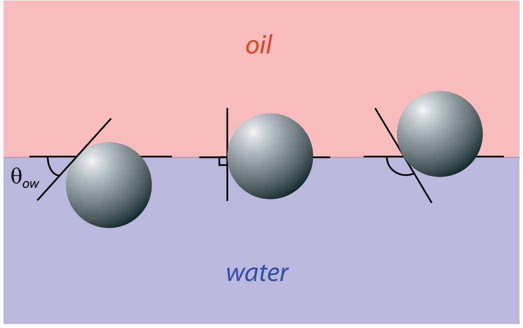

Figure 2.9: Position of a spherical particle at an oil/water interface - Position represented for a contact angle less than 90° (left), equal to 90° (centre) and greater than 90° (right). *Adapted from Binks [71]*

For an optimal stabilisation of emulsions, its value should be close to 90°. Particles with a contact angle smaller than 90° are usually called hydrophilic and if the contact angle is greater than 90° they are called hydrophobic. The emulsion type (O/W or W/O) strongly depends on the value of this contact angle.

The wettability of the particles (measured by the value of the contact angle) influences the amount of energy required to remove a particle from the interface. Assuming a spherical solid particle that is small (submicron), with negligible mass, the energy required to remove a particle of radius r from the interface is given by the equation [71–73]:

$$E = \pi r^2 \gamma_{ow} (1 \pm cos\theta)^2 \tag{2.10}$$

The sign in the equation is positive when moving the particle into the oil phase and negative when moving the particle into the aqueous phase. Depending on the contact angle, the adsorption strength of a particle at the interface can be high or low. It is low (10 $k_B T$) for angles between 0° and 20° or 160° and 180° and maximum for angles approaching 90° [71]. For a contact angle close to 90° the energy to remove a particle from the interface is of the order of a few 1000 $k_B T$. In that case, the adsorption can be considered irreversible.

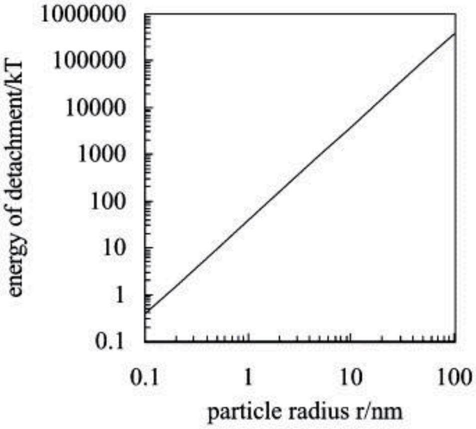

Figure 2.10: Energy of detachment of a particle according to its radius - Energy calculated for a contact angle of 90° and an interfacial tension of 50 $mN.m^{-1}$. We can notice that the energy is really low for radii smaller than 0.5 nm. *Graph from Binks [71]*

The adsorption energy varies considerably with the size of the particles. Figure 2.10 shows the adhesion energy of a particle as a function of its radius. Typically, for very small particles (less than 0.5 nm), the adsorption energy is low regardless of the contact angle (less than 7 $k_B T$). Particles of this kind are not effective as stabilizer because the detachment of the interface is then relatively easy.

Although the phenomenon of stabilisation of emulsions by particles has been known for a long time, their applications are still under development. In biomedical engineering, for example, Pickering emulsions are used to create colloidosomes that could deliver precise concentrations of drugs to specific targets in the human body. Understanding the behaviour of particles at liquid interfaces is also relevant to many aspects of chemical engineering, water purification, mineral recovery techniques, petroleum industry and the manufacture of nanostructured materials, especially when the formation of these emulsions is expected or when it is a technological problem.

2.3 Colloidal self-assembly

Well-defined ordered structures prepared from nanoparticles provide new opportunities for optimizing the properties and performance of new materials made from NPs[74]. Tuning particle size and interparticle distance allow us to obtain a nanocrystal system with tuned properties. Self-organisation of nanoparticles is a new route for the formation of superlattice materials which is achieved by controlling size and shape of the selected nanocrystals and using self-assembly as a way to bound them altogether [75]. In nanocrystal self-assembled structures, nanocrystals are the fundamental building units, acting as “atoms” for the construction of the ordered structure. The properties of the superlattice materials is determined not only by the individual properties of each particle but also by the interaction between those nanocrystals. For example, if the building blocks are magnetic nanocrystals, magnetic effects may be brought into the assembled structure.

Several approaches have been used in order to obtain 2D and 3D structures [75]. Spontaneous formation of periodic domain structures is a phenomenon that has been known for several decades. The formation of nanometer-scale ordered structures has become a subject of intense experimental and theoretical studies. It can be realized using several techniques such as the bulk destabilisation on a solid surface or using templates. The template is the host for the formation of ordered structure and has the advantage that we can control the size and shape of the ordered structures formed. Moreover, they are well-defined systems in which assembly mechanisms can be studied. This procedure is sometimes refered to as TASA template-assisted self-assembly [76]. Templating has been explored by a number of groups as a powerful tool to direct and control assembly processes.

Droplets have emerged as a versatile tool for the development of multiple microscale applications in the last decades. The droplets work as sites for fabrication of hierarchical and responsive materials which can find applications in photonics [77, 78], microfluidics [79, 80] and targeted delivery materials [81–83]. Emulsion droplets and colloidal particles have been exploited as templates for the formation of microcapsules, colloidosomes or supraparticles. Velev et al. demonstrated the use of emulsion droplets as template for the fabrication of dense and hollow spheres from latex particles [22, 23]. They emulsified octanol in an aqueous suspension of latex particles, which were coated with a surfactant to render them more hydrophobic. This caused the spheres to segregate to the interface. After removal of the oil phase, spherical aggregates of disordered spheres were produced. Colloidosomes were later produced by Dinsmore et al. [84]. They consist of hollow, elastic shells whose permeability and elasticity could be precisely controlled. The generality and robustness of these structures were demonstrated by the use of a variety of solvents, particles and contents. To produce capsules with specific properties, temperature-sensitive microgel particles were used to fabricate colloidosomes which expanded and contracted upon heating and cooling. Dinsmore et al. showed that colloidosomes can serve as semi-permeable capsules (figure 2.11).

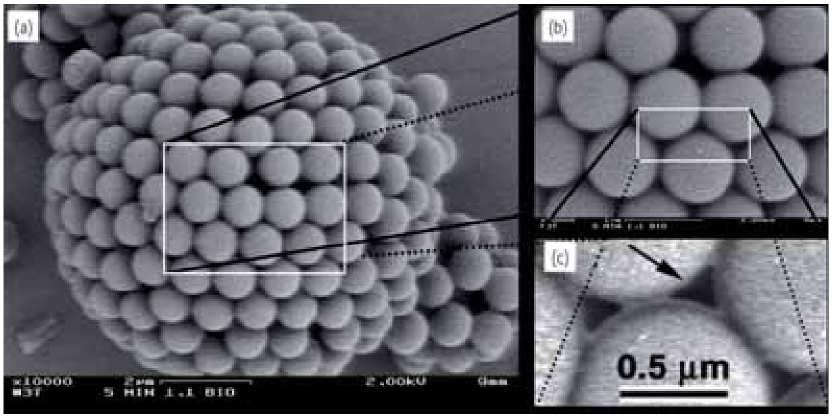

Figure 2.11: Scanning electron microscope image of a dried colloidosome - The 10µm diameter colloidosomes are composed of 0.9µm diameter polystyrene spheres. The beads were sintered together. *Image from Dinsmore et al. [84]*

In subsequent work, Pine and his co-workers (in particular Manoharan) recognized that colloidal particles in the micrometer regime organize into structures when confined in an emulsion droplet [29]. They developed a practical method to form well-defined hard-sphere clusters which were fabricated by drying the oil out of an oil-in-water emulsion. They recognized that well-defined clusters formed when evaporating Pickering emulsions where the polystyrene (PS) microspheres were bound to the interface. Removing the liquid from the droplet containing particles generates compressive forces that draw the particles together. Once the spheres are at the interface, capillary forces are generated and lead to a rearrangement of particles into a defined cluster.

More recently, ordered supraparticles formed where the particles were prevented from collecting at the interface of the droplets [85]. The supraparticles are made by encapsulating polymer colloidal particles (PMMA) in emulsion droplets of hexane. Subsequent removal of the hexane from the droplets led to spherical aggregates of polymer spheres (figure 2.12). The use of two different kinds of surfactants, a standard water-soluble surfactant, and an oil-soluble species prevents particles from sticking to the interface. The addition of a secondary surfactant reduces the binding energy close to the thermal energy, allowing the particles to move freely throughout the droplet and form dense, ordered supraparticles upon removal of the solvent.

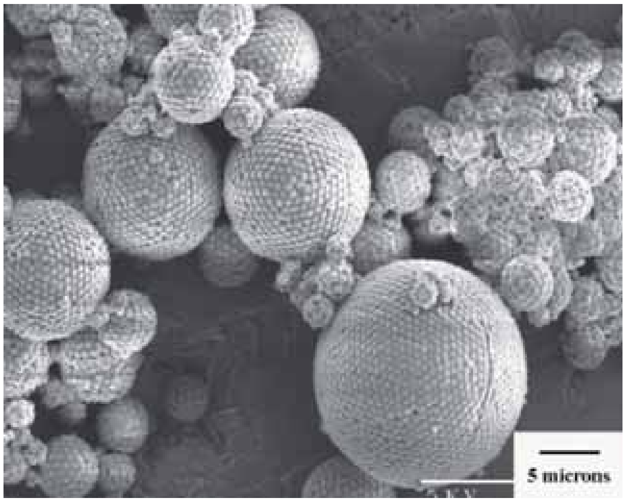

Figure 2.12: Scanning electron microscope image of PMMA supraparticles - The supraparticles are composed of 600-nm-diameter PMMA spheres. On the outside, the particles are arranged in spherical shells resembling the colloidosome structures. Many of the supraparticles are also faceted rather than spherical. *Image from Manoharan [85]*

Chapter 3

Experimental and instrumentation

3.1 Materials

3.1.1 Gold nanoparticles

Gold nanoparticles with core diameters of 6 nm were synthesized using a route adapted from Zheng et al. [86]. They were formed in a one-pot reduction of a gold source by an amine-borane complex in the presence of an alkyl thiol. Chlorotriphenylphosphine gold (ABCR, minimum purity 98%) was mixed with dodecanethiol (Fluka, 98%) in benzene (Riedel-de-Hahn, 99.5%) to form a clear solution to which the tert-butylamine-borane complex (Fluka, 97%) was subsequently added. The mixture was heated to 55 °C for 2 h during which the solution turned into a dark purple color indicating nanoparticle formation. After the reduction reaction the gold nanoparticle suspension was cooled to room temperature. The particles were then precipitated by the addition of ethanol, washed by centrifugation, and subsequently resuspended in hexane.

The size of the metal core of the particles was measured using transmission electron microscopy (TEM) and small-angle X-ray scattering (SAXS) and are presented in Table 3.1.

3.1.2 Surfactants

To stabilise the emulsion, different surfactants were used. Sodium dodecyl sulfate (SDS), polyethylene octyl phenyl ether (Triton X-100), Sorbitan monolaurate (Span

	TEM		SAXS	
	Radius [nm]	σ	Radius [nm]	σ
Gold nanoparticle	3.2	0.29	3.55	0.3

Table 3.1: Size of the core of the gold nanoparticles - Size and size distribution (σ) of the gold cores of the particles were analyzed from TEM using the ImageJ analysis software for dozens of particles and from SAXS by fitting the form factor to the scattering profiles of diluted samples.

20) and Polyethylene glycol sorbitan trioleate (Tween 85) were purchased from Sigma-Aldrich. Table 3.2 introduces some of their properties as provided by the manufacturers and the references mentioned.

	Molecular formula	Type	Molecular weight	cmc [mmol/L]	density [g/mL]	HLB value
Triton X-100		non-ionic	624	0.2 – 0.9	1.07	13.5
Twenn 85	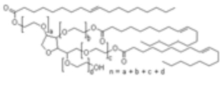	non-ionic	1741	0.00029 [87]	1.028	11
Span 20	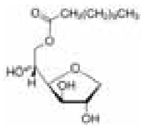	non-ionic	346.47	0.021 [88]	1.032	8.6
SDS	 $CH_3(CH_2)_{10}CH_2O-\overset{O}{\underset{O}{S}}-ONa$	anionic	289	8.2 [89]	1.01	40

Table 3.2: Some properties of surfactants used for the preparation of emulsions

3.1.3 Emulsions

Nanoparticle-containing oil-in-water microemulsions were prepared by emulsification of a nanoparticle dispersion in water containing different surfactants. Efficient emulsification was achieved by using ultrasonic or mechanical shearing, which yielded similar results.

3.1.3.1 Emulsification by mechanical shearing

Emulsions were made from a macroscopic mixture of water and oil, where one of the two phases contains colloidal particles. Fragmentation of the dispersed phase was produced by stirring the mixture using an Ultra-Turrax benchtop homogenizer (Typ T-25, IKA-Werke GmbH, Staufen, Germany) at 20500 rpm during 30 min. The system consists of a rotor within a stationary stator which are separated by a gap. Due to the high rotational speed, the emulsion is drawn automatically in the axial direction, into the dispersion head and then compressed in the radial direction, through the slots of the rotor / stator system. The droplets are fragmented in the velocity gradient prevailing in the air gap.

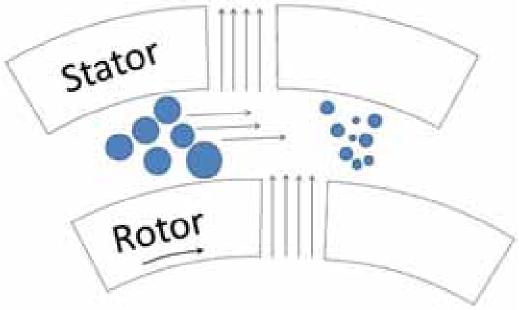

Figure 3.1: Principle of Ultra-Turrax benchtop homogeniser - The fluid is drawn in the axial direction due to the high rotation speed and then pressed radially through the slots of the rotor / stator system. The emulsion is thus subjected to very high shear forces and fragmented into smaller droplets in the gap between the rotor and the stator

The device is equipped with a motor for movement of the rotor at different speeds: from 3000 to 24000 rotations per minute. The turbulent flow implemented allows fragmenting drops but very energetic collisions cause recombination events (coalescence). After a few minutes, a steady state is established in which the distribution of drop sizes result from a complex coupling between fragmentation and recombination.

3.1.3.2 Emulsification by ultrasound

The emulsion could also by sonicated using an ultrasonic bath (S100H Elmasonic, Elma GmbH & CoLG, Singen, Germany) at 40 °C for 30 min. The principle is presented in figure 3.2. The application of ultrasound causes acoustic cavitation resulting in the formation, growth and subsequent implosive collapse of bubbles by the pressure fluctuations of a simple sound wave, which creates extreme levels of highly localized turbulence. The turbulent implosions break up primary droplets into sub-micro size droplets.

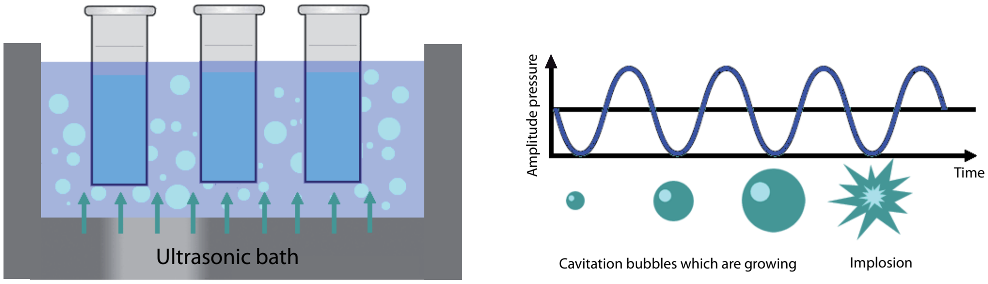

Figure 3.2: Ultrasound and Cavitation - Ultrasound results in successive waves which induce the fromation of bubbles that oscillate and eventually grow to an unstable size and then implode

For a typical experiment, gold nanoparticles dispersion in hexane were mixed with ultrapure water (Milli-Q water purification system type ELIX 20, Millipore Corp., USA) and 1% per weight aqueous solution of surfactant. In order to enhance good stabilisation, the surfactant concentration was adjusted to be above critical micelle concentration (cmc). Exact concentrations are given in table 3.3

	Surfactants			
	Triton X-100	Tween 85	Span 20	SDS
Volume water [mL]	16	16	16.31	16
Volume gold suspension [µL]	320	320	320	320
Volume surfactant [µL]	320	320	4000	320
Concentration of surfactant in emulsion [mmol]	0.3	0.11	8.4	0.57

Table 3.3: Emulsion characteristics

After emulsification from mechanical shearing or ultrasound, the solvent was then removed from the emulsion droplets by evaporation. In the simplest case, the oil phase was left to evaporate at room temperature and ambient pressure for at least 12 h. For the synchrotron SAXS study, evaporation was enhanced using a nitrogen stream. A sealed vessel containing the emulsion was submerged into a thermostated bath and kept at 298 K. The vessel was connected to a nitrogen stream that bubbled through the emulsion to permit evaporation of the dispersed solvent in only 4 h.

3.2 Characterisation techniques

The following section gives an overview about the experimental techniques used in this work.

3.2.1 UV-Vis spectroscopy

UV-Vis spectrometry was performed using a Cary 5000 photospectrometer (Varian Inc., USA) that recorded spectra in the wavelength range from 200 nm to 800 nm. Approximately 1 mL of the respective samples was measured using a quartz cuvette with a beam path of 1 cm. The spectrum of the background (water or hexane) was subtracted from the samples' UV-Vis spectra.

The UV-Vis spectra were fitted with Lorentz curves for the determination of absorbance (A_{SPR}) and wavelength (λ_{SPR}) at peak maximum. The Lorentz fits of the UV-Vis spectra were performed using Origin 8.0 software. The Gaussian fits function gives good results of fit values ($\chi^2 \approx 1$), proving accurate curve analysis.

3.2.2 Transmission electron microscopy

Morphological and structural characterisation was carried out with a CM 200 electron microscope (Philips, Netherlands) operating at 200 keV. Samples were prepared by placing a drop of the supraparticle-containing dispersion on the surface of a carbon-coated copper grid and allowing the grid to dry in air. To determine the mean size of the gold cores of the particles and the interparticle distance between agglomerated nanoparticles, several dozens of particles were evaluated using the ImageJ analysis software (available for free download from the NIH) (figure 3.3).

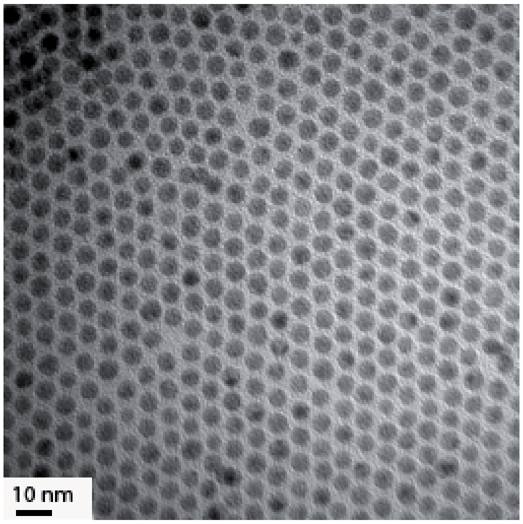

Figure 3.3: Gold nanoparticles - TEM image of 3.55 nm radius gold nanoparticles capped with dodecane-1-thiol.

3.2.3 Scanning electron microscopy

A scanning electron microscope (SEM) (FEI Quanta 400F, FEI Europe, Eindhoven, Netherlands) was used to characterize the surface structure of large supraparticles. Samples for SEM were prepared by placing a drop of the supraparticle-containing dispersion on the surface of a silicon wafer and allowing it to dry in air.

3.2.4 Tensiometry

The interfacial tension between the inner and outer phases results in an increased pressure inside the drop. The relationship between the difference in pressure Δp and the interfacial tension is described by the Young-Laplace equation,

$$\Delta p = \gamma \left(\frac{1}{R_1} + \frac{1}{R_2} \right) \tag{3.1}$$

where Δp is the pressure difference at the drop interface, γ is the interfacial tension, and R_1 and R_2 are the radii of curvature of the drop. Without external forces, the drop should have a spherical shape. However, the effect of gravity will deform the drop by generating an increasing pressure inside the drop and the pressure difference can be rewritten as:

$$\Delta p = \Delta p_0 + \Delta \rho g z \tag{3.2}$$

where Δp_0 is the reference pressure without influence of gravity, $\Delta\rho$ is the difference in density between the two phases, g is the gravitational acceleration and z is the vertical distance between measuring point and opening of needle.

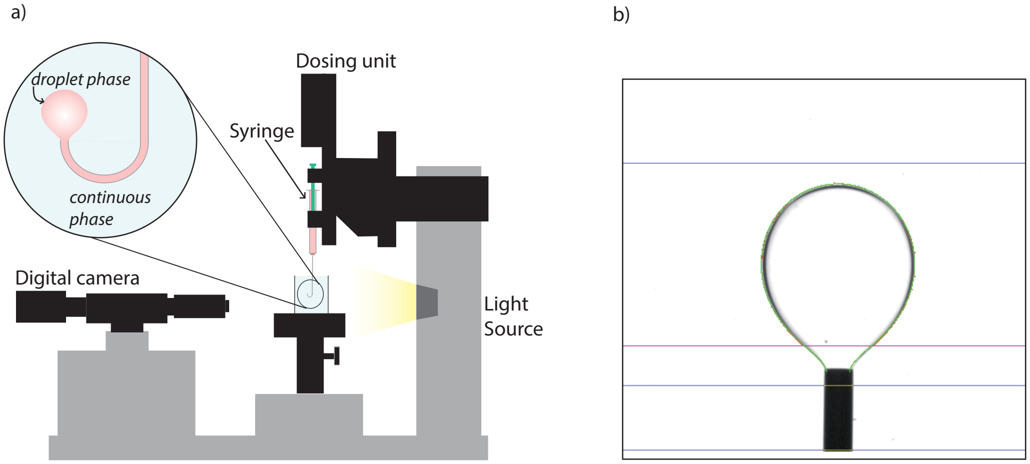

Figure 3.4: Pendant Droplet tensiometer - a) Shematic representation of the pendant droplet tensiometer setup. b) Optical image of a pendant droplet of hexane held by J-needle in water. The shape of the pendant droplet is captured by tensiometer and fit to a shape (green curve around the droplet) predicted by the Young-Laplace equation using the software provided with the tensiometer.

The volume of the drops was chosen such that they were deformed by gravity, just before the point of break-off from the needle tip. Since the shape of the drop depends on the interfacial tension of the system, different volumes (between 1 µL and 20 µL) were chosen depending on the system studied. To determine te interfacial tension, the shape of the droplet was captured and fit to a shape predicted by the Young-Laplace equation using software provided with the tensiometer.

Interfacial tension measurements were carried out on a DSA 100 pendant drop tensiometer (Krüss GmbH, Germany), which we used as a drop shape analyzer. Measurements were performed at an ambient temperature of 295 K ± 1 K. Drop images were acquired by a black and white, high-speed camera and analyzed using the DSA3 software supplied by the manufacturer. To measure the oil-water interfacial tension, the continuous phase was filled into a quartz glass cuvette. The dispersed phase was filled into a glass syringe which was connected to a J-shaped needle that protruded into the cuvette as illustrated in figure 3.4 a).

The interfacial tension values were obtained by fitting the profile of the pendant drop to its theoretical shape using the DSA3 software as shown in figure 3.4 b). The arithmetic mean and the standard deviation of at least three measurements were used as interfacial tension values.

For all measurement performed in this work, the concentration of gold in hexane was 0.38 mg/mL. All surfactants were at concentrations considerably above cmc, approximately 9 mmol of SDS in water, approximately 1 mmol of Triton X-100 in water, approximately 1 mmol of Tween 85 in water and approximately 1 mmol of Span 20 in water. The drops assumed their equilibrium shapes after 1 min; repeated measurements were peformed during 5 min until a plateau was reached that we report as the equilibrium interfacial tension.

3.2.5 Dynamic light scattering

Dispersed particles, when suspended in a liquid medium, undergo Brownian motion which causes fluctuations of the local concentration of the particles, resulting in fluctuations in the intensity of the scattered light.

From the time-dependent intensity fluctuations and by using a correlator we can determine a so-called autocorrelation function, $g(\tau)$:

$$g(\tau) = \frac{\langle I(q,0)I(q,\tau)\rangle}{\langle I(q)\rangle^2} = e^{-2Dq^2\tau} \tag{3.3}$$

where D is the diffusion coefficient of the particles and q is the scattering vector defined as

$$q = \frac{4\pi n}{\lambda} sin\left(\frac{\theta}{2}\right) \tag{3.4}$$

and n is the refractive index of the medium, λ the laser wavelength, and θ the scattering angle.

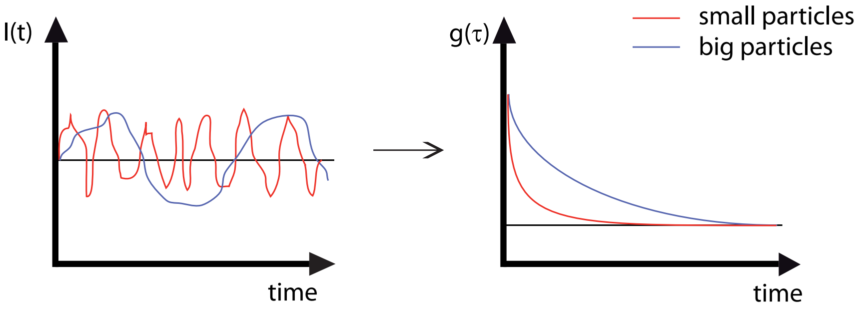

Figure 3.5: Intensity and autocorrelation function - Smaller particles are moving more rapidly than bigger particles resulting in a smaller decay time

Assuming that the particles are spherical and non-interacting, the mean radius is obtained from the Stokes-Einstein equation:

$$R_H = \frac{k_B T}{6\pi\mu D} \tag{3.5}$$

where k_B is the Boltzmann constant, T the temperature, and μ the shear viscosity of the solvent.

At a constant temperature T the method only requires the knowledge of the viscosity μ of the suspending fluid for an estimation of the average particle size and its distribution function. The radius measured in DLS is called the hydrodynamic radius and refers to how a particle diffuses within a fluid. The radius obtained by this technique depends not only on the size of the particle, but also on the ligand attached to their surface (Figure 3.6). This means that the size calculated may be larger than that measured by electron microscopy which indicate to the diameter of the core.

Dynamic light scattering (DLS) was performed using a laser scattering goniometer (CGS-3, ALV GmbH, Germany) equipped with a 35 mW HeNe laser emitting at a wavelength of 632.8 nm. The scattered light was collected at 90° scattering angle, split and detected by two avalanche photodiodes. A hardware correlator (ALV-7004, ALV GmbH, Germany) correlates the scattered intensity data in real time and outputs the

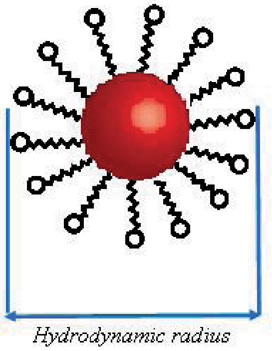

Figure 3.6: Hydrodynamic radius of a particle - The diameter measured in DLS takes into account the ligand shells which are attached at the surface of a particle

normalized intensity correlation function as a function of the delay time. The sample was contained in a 1 cm-diameter glass cuvette held in a sample chamber filled with toluene. Its temperature was held at 293 K by a thermostated, circulating water bath (Phoenix II, Haake, Germany).

3.2.6 Small angle X-ray scattering

Small angle X-ray scattering allows the characterisation of the material which is irradiated by x-rays as a function of its scattered intensity. It is sensitive to the size, the shape, the concentration of particles in the sample and their interactions. By measuring the scattered intensity for small angles (i.e. close to the direction of the incident light), we have access to the structural properties of the sample to a scale in the order of $2\pi/q$. For a range of scattering vector q between 0.006 nm^{-1} and 6 nm^{-1}, it corresponds to scales between 1 μm and 1 nm.

When a beam of wavelength λ, with a diffusion vector and k_i, with a flow N_0 (in counts/s) irradiate a sample of volume V and thickness e, a fraction N of the flow is elastically scattered in the direction k_d in the solid angle $\Delta\Omega$ (Figure 3.7) :

$$\Delta N = N_0 T_r \frac{e}{V} \frac{d\sigma}{d\Omega} \overrightarrow{k_d} \Delta\Omega \tag{3.6}$$

where T_r is the transmission of the sample and $(\frac{d\sigma}{d\Omega})\overrightarrow{k_d}$ is the effective differential scattering cross section. The scattering intensity per unit volume is defined by:

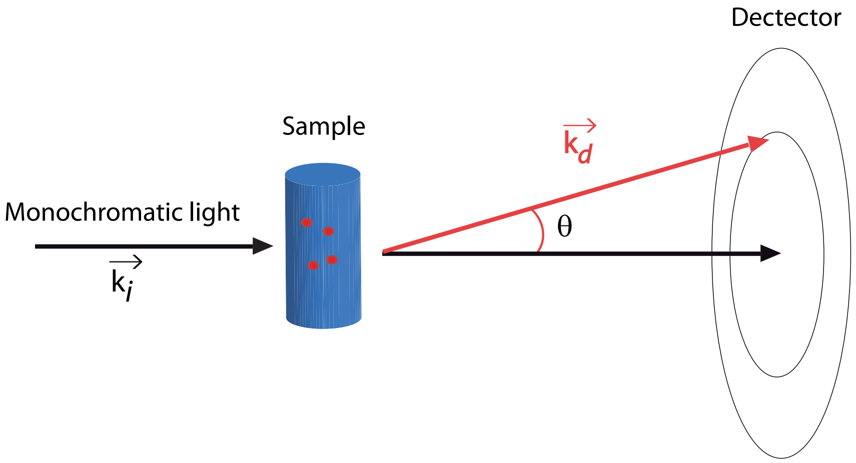

Figure 3.7: Principle of SAXS - the sample is irradiated by a monochromatic X-ray and the scattered intensity from the sample are detected on the detector

$$I = \frac{1}{V}\frac{d\rho}{d\Omega}\overrightarrow{k_d} = \frac{\Delta N}{N_0}\frac{1}{T_r e \Delta\Omega} \tag{3.7}$$

and the scattering vector $\overrightarrow{q} = \overrightarrow{k_d} - \overrightarrow{k_i}$, is defined by its amplitude :

$$q = \frac{4\pi n}{\lambda} sin\left(\frac{\theta}{2}\right) \tag{3.8}$$

The scattered intensity for a set of N particles can be written as

$$I(q) = \phi V_p F(q) S(q) \tag{3.9}$$

where ϕ is the concentration of particles, V_p their volume and $F(q)$, the so-called form factor which describes the scattering of individual particles and contains information on the size and shape of the particles. The structure factor $S(q)$ describes the interference by light scattered from different particles and contains information about the interparticle interactions. In the case of dilute suspension, no interactions between particles are observed and $S(q) \approx 1$. The scattering profile of the intensity $I(q)$ therefore describes only the size and shape of the particle. For homogeneous spherical particles, the form factor can be described as a function of the radius of particle R [90]:

$$F(q) = \left[\frac{3}{(qR)^3} (sin(qR) - qRcos(qR) \right]^2 \tag{3.10}$$

$S(q)$ describes the inter-particle correlations and is sensitive to interactions between them. Different expressions were developed for the determination of the structure factor.

In the case where the particles become sufficiently attractive and form clusters, the excess scattering at low q can be described by a Lorentzian term $S_c(q)$ [91],

$$S_c(q) = \frac{I_M}{(1 + q^2 \xi^2)^p}, \tag{3.11}$$

where I_M and ξ are proportional to the average mass and size of the clusters, and p is a power-law exponent related to the fractal dimension of the clusters.

SAXS experiments were carried out at the SAXS beam line ID02 of the European Synchrotron Radiation Facility (ESRF) in Grenoble, France. The experiments were repeated for two different sample-detector distances (10 m and 1 m) to cover a wide q range, at a wavelength of $\lambda = 0.1$ nm and scattering angles 2θ between 0.009 and 6°). Two different emulsions were analysed subsequently at the two sample-detector distances. During the evaporation of the particle-containing emulsion, 0.3 µL emulsion were removed every 10 min, introduced into a flow-through capillary cell (outside diameter approximately 2 mm, wall thickness approximately 0.01 mm) and characterized in a SAXS measurement. The procedure was repeated until complete evaporation of the solvent was reached. We used the same cell during all experiments to enable reliable subtraction of the background. The two-dimensional scattering images were radially averaged, a water background was subtracted and the data was analyzed using ESRF's SAXSutilities software [91]. For measurements on dried clusters, drops of the supraparticle-containing dispersion were placed on the surface of a mica window (diameter 16 mm and thickness 10 µm to 20 µm) and allowed to dry in air. The windows were placed in a four-position sample changer normal to the beam.

3.2.7 Analytical centrifugation

The stability of the ageing dispersions was characterized by precipitating them in a polar solvent mixture and analytical centrifugation. Filtered dispersions were mixed with equal volumes of 1-propanol and immediately transferred to cuvettes in a LUMiSizer multisample analytical centrifuge (L. U. M. GmbH, Berlin, Germany). 1-propanol was chosen as it mixes well with hexane. The centrifuge uses a line array detector and LED light source to measure space- and time-resolved extinction profiles while the sample rotates at defined speed and temperature as illustrated in figure 3.8. Intensities of the transmitted light as a function of time and position over the entire length of the cuvette were recorded. Agglomeration and phase separation of the individual samples was compared and analyzed by tracing the sedimentation of the particles and their agglomerates.

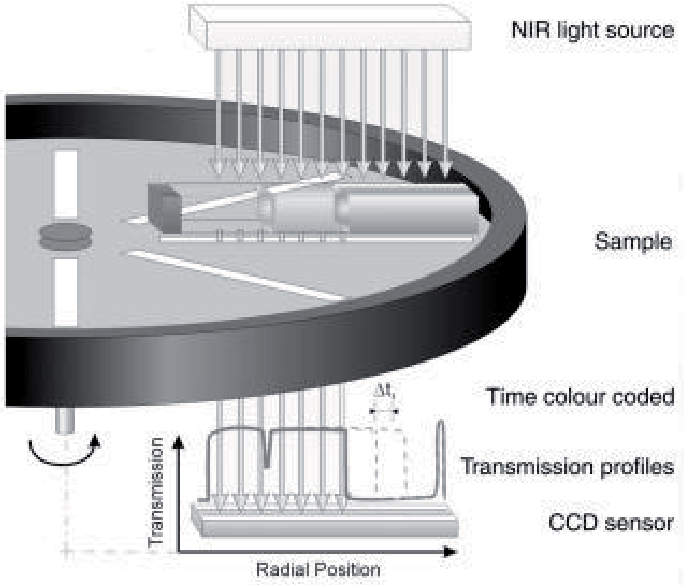

Figure 3.8: Measurement scheme of the LUMiSizer - Parallel NIR light goes through the sample and the transmission profiles are detected as a function of time and position over the entire cell lenght.*Figure from Sobisch et al.[92]*

All measurements were made in polycarbonate tubes (synthetic rectangular cell PC), 2 mm transmission path, 0.4 ml filling capacity (L. U. M. GmbH, Berlin, Germany) at velocities from 300 to 2500 rpm. SEPView software provided by the manufacturer was used to control the instrument and analyze data. The evolution of the transmission profiles contains information on particle size distribution and agglomeration kinetics.

3.2.8 Atomic absorption spectrometry

The gold content in the supernatant liquid of gold suspension was characterized by elementary analysis after all AuNP had been removed. Dispersions were precipitated with the same volume of ethanol and centrifuged at 20500 rpm for 15 min. Gold in the supernatant was quantified using a contrAA 700 high-resolution continuum source atomic absorption spectrometer (HRCS-AAS). The spectrometer was equipped with a Xe short arc lamp as a light source shining through the sample-containing graphite furnace.

A solution of 400 μg/L of gold equivalent in 1-propanol (in the form of chlorotriphenylphosphine gold) was used as standard solution. The samples were diluted with 1-propanol at a volume ratio of 1:10. A volume of 20 μL of the diluted sample was injected into the graphite tube. Transmission was measured at a wavelength of 267.595 nm.

Drying, pyrolysis, and atomisation in the graphite furnace were performed according to Table 3.4. The mean absorbances of duplicate injections were used throughout the study.

Averages of two absorbance values from sequential injections were used throughout this work.

Programm step	Temperature [°C]	Ramp [°C/s]	Hold time [s]	Gas flow [L/min]
Drying 1	90	6	20	0
Drying 2	120	6	10	0
Drying 3	150	6	5	0
Pyrolysis	800	100	20	0
Auto zero	800	0	5	0
Automatization	2200	1600	3	0
Cleaning	2500	500	5	0

Table 3.4: Graphite furnace temperature programs for the determination of gold in supernantant liquid using HR-CS AAS.

Chapter 4

Assembly of gold nanoparticles into Lennard-Jones-like Clusters

This chapter was published in *Nano Letters 2012 12 (6), 3279-3282.* [93]

4.1 State of the art

The emulsion encapsulation method is an interesting route to clusters-like aggragates with unique configurations of particles. Manoharan, Elsesser and Pine [29] found that when a small number of colloidal microspheres are attached to the surfaces of liquid emulsion droplets, removing fluid from the droplets leads to packing of hard-sphere-like microspheres. The structure of the clusters obtained range from sphere doublets, triangles, tetrahedra and octaehdra to unusual polyhedra.

Almost a decade ago, Manoharan [30] recognized that the resulting structures can be classified into three different groups: colloidosomes (where the particles sit at the liquid-liquid-interface), colloidal clusters (small polyhedral configurations of colloids formed by capillary forces) and supraparticles (close-packed spherical crystallites). The packing structure obtained is unique and depends only on the number of particles.

In 2005, Pine, working together with Yang and Cho [94], described the fromation of colliodal cluster formed from 830-nm PS and 800-nm silica particles using a water-in-oil emulsion. The aqueous silica suspension was emulsified in hexadecane or toluene followed by slow evaporation of water leading to the formation of silica clusters. They investigated how surface properties of particles influence the cluster structure. Depending on the number of nanoparticles per cluster, n, the structure changes. For $n \leq 8$ the cluster structure appears to have a unique configuration whereas for $n = 8$ and $n = 11$, some isomeric clusters were observed depending on the electro-kinetic properties of the surface of the colloidal particles.

In 2007, Bai [24] used an emulsion-based approach to assemble nanocrystals from various shape, composition and size. The structure of the supraparticles obtained with sizes ranging from 100 to 200 nm radius was not investigated.

Rastogi use the evaporation-based self-assembly method to form supraparticles from a mixed suspension of latex microspheres with different diameter (from 320 nm to 1000 nm) and gold nanoparticles with a diameter of 22 nm [78]. A droplet of the suspension was deposited on solid superhydrophobic substrate and let to evaporate during 60 min. The results are spherical supraballs or opal balls with colored domains organized in series of concentric rings. During the solvent evaporation process, the gold nanoparticles are small enough to pass through the interstices of the latex particles and are thus located on the surface of the droplet.

More recently, an emulsion-based self-assembly method was used to assemble particles into clusters ($n > 15$), supraparticles ($n > 100$), and supraballs ($n \gg 100$) [94]. They were fabricated by removing the dispersed solvent from a toluene-in-water or water-in-toluene emulsion. During the evaporation process crosslinked PS nanospheres were packed closely into higher-order clusters, supraparticles or ordered supraballs, depending on the size of the emulsion droplet and the concentration on PS particle inside each droplet (figure 4.1).

Higher-ordered clusters with structural complexity were generated by assembling a small number of PS particles ($n \leq 15$). For a higher number of particles inside each droplet, spherical aggregates, namely, supraparticles, were generated. In that case, the degree of packing order was not high enough to be classified as hexagonal or fcc structure and were defined by the author as supraparticles with intermediate packing ordering. When the concentration of PS particles was further increased, ordered supraballs with hexagonal packed structure were obtained.

The emulsion-templated structures presented previously are not minimum-energy arrangements, but bear witness to their formation mechanism. Here, I introduce a process that lets defined numbers of nanoparticles reach their minimum energy configurations. Monodispersed gold nanoparticles in hexane were emulsified in water using

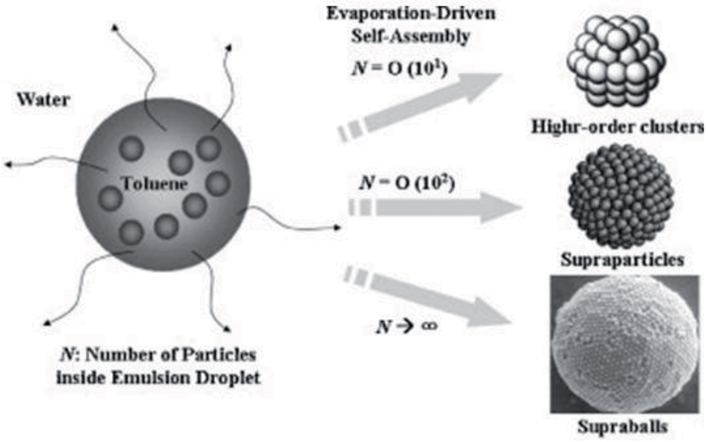

Figure 4.1: Schematic diagram for the fabrication of colloidal aggregates - Evaporation of droplet containing PS nanospheres leads to the formation of higher-order clusters, supraparticles, or hexagonally packed spherical colloidal crystals, namely, supraballs depending on the number of nanospheres. When the number of nanospheres inside the droplets is relatively small, the resultant self-assembled structures will be higher-order clusters, small supraparticles with intermediate packing ordering or hexagonally ordered supraballs. *Image from Cho et al. [94]*

Triton X-100 as a surfactant. The dispersed phase was then slowly evaporated until only the nanoparticles remained (For more details on the emulsification and cluster formation process, see *chapter 3.1.3*). The colloildal clusters formed have some interesting structures that are studied in this chapter.

In the first part of the discussion I will describe the formation of clusters and show that we can obtain interesting structures. I will then present some results on the in-situ measurements during the evaporation. In a second part, I will introduce the different mechanisms that could lead to the formation of the supraparticles and I will determine what is the exact formation route that leads to the clusters with interesting structures.

4.2 Results and discussion

4.2.1 Structure of supraparticles

The stable dispersion of supraparticles is sufficiently robust to dry them and analyze the arrangement of the constituent particles with the TEM.

As shown in figures 4.2 and 4.3 h, polydispersity of the emulsion leads to clusters

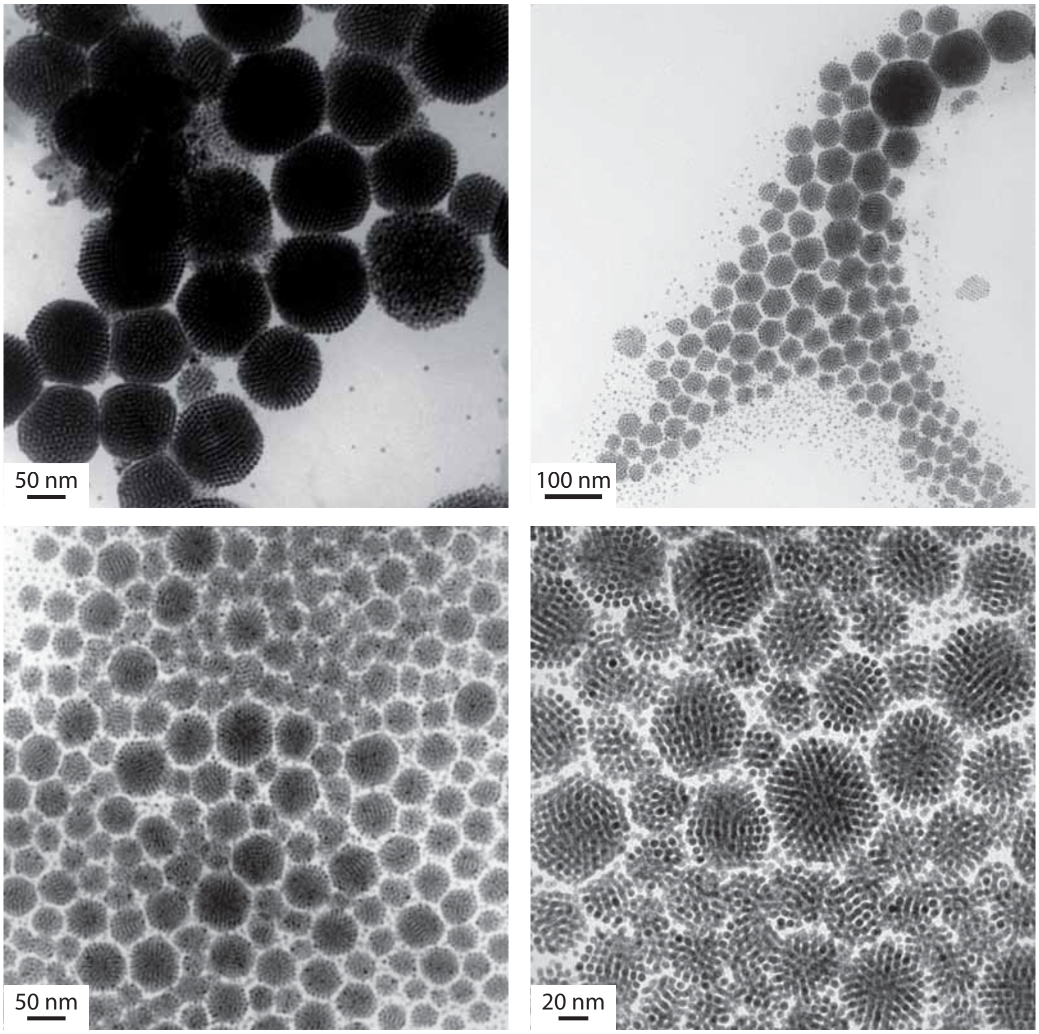

Figure 4.2: Transmisson electron micrograph from different batches of supraparticles - While some supraparticles seems damaged by the drying process, a large amount of supraparticles shows regular structures.

consisting of different numbers of nanoparticles. Upon careful evaporation, the supraparticles assembled into hierarchical superlattices. The assembled structures were regular, but not simple pieces of crystal lattices. We find them reproducible even when changing the evaporation technique between a heated ultrasonic bath, a rotational evaporator or a bubbler.

For comparison, Figure 4.3 b and c show the TEM and small-angle X-ray scattering images of precipitated polycrystalline agglomerates. The scattering ring at $q = 0.93\ \mathrm{nm}^{-1}$ indicates the (111) lattice plane distance of the fcc packing while other rings can be indexed to other lattice planes using Bragg's law,

$$q = 2\pi \frac{\sqrt{h^2 + k^2 + l^2}}{a_l} \tag{4.1}$$

where a_l is the lattice constant and h, k and l are the Miller indices [95]. The (111) ring also occurs in the scattering from sparse layers of dry supraparticles made from the same nanoparticles (figure 4.3 g). It is broadened, however, by the distorted lattices in the clusters. Reflexes on the ring and (weaker) at slightly lower q represent crystalline regions in the supraparticles with different orientations. Reflexes at lower q probably represent the increased interparticle spacing at boundaries inside the clusters.

Some elements of the supraparticles' internal structure visible in figure 4.2, in particular "zipper"-like central lines, remind of the features used for the identification of icosahedral atomic clusters in TEM [96]. The supraparticles also exhibit crystalline outer facets that are reminiscent of atomic clusters.

4.2.2 Formation mechanism of the supraparticles

In order to understand the mechanism of formation of the supraparticles, in situ observation of the assembly process was performed through surface plasmon spectroscopy and small-angle x-ray scattering. Samples were removed from the evaporating emulsions at regular intervals and characterized by UV-Vis spectroscopy. The surface plasmon resonance (SPR) of the gold nanoparticles depends on the average particle distances; UV-Vis spectra therefore indicate the local concentration of particles.

The large droplets in freshly prepared emulsion scatter light efficiently and cause an overall weak transmission (Figure 4.4, a). As the droplets evaporate, transmission increases. After 80 min of evaporation time, the surface plasmon peak is clearly visible

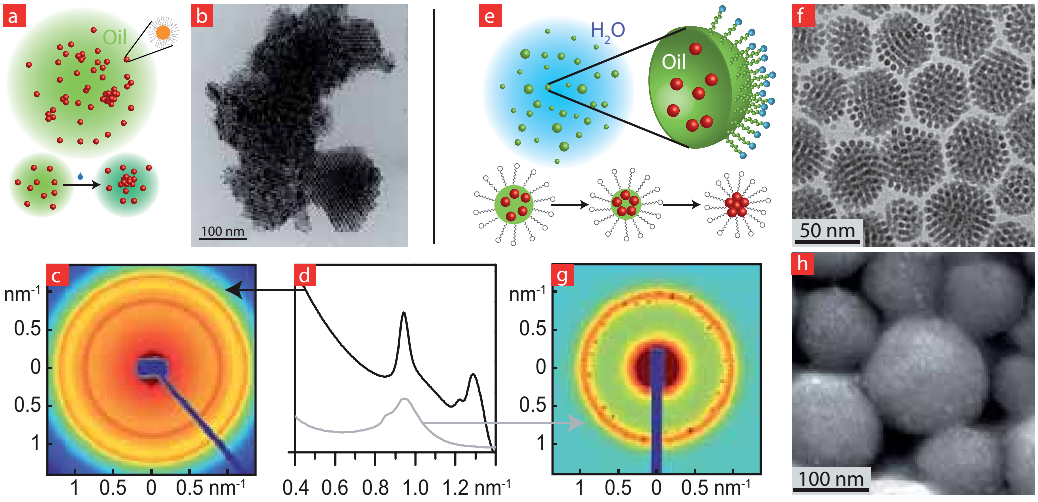

Figure 4.3: Nanoparticle clusters created outside and inside of emulsion templates - Addition of an incompatible solvent to a dispersion of alkanethiol-stabilized gold nanoparticles (a) yields irregular pieces of densely packed nanoparticle crystals (b) that sediment and exhibit pronounced Bragg peaks in SAXS (c,d). In contrast, emulsion-templated assembly (e) yields supraparticles that exhibit Lennard-Jones-Cluster-like internal structures as revealed by transmission electron microscopy (f). Their small-angle scattering pattern (g) indicates a regular structure different from the densely packed superlattice (d). The larger the supraparticle, the more crystalline its surfaces appear in scanning electron microscopy (h).

at $\lambda = 516\,\text{nm}$. It slowly shifts until a drastic change to 520 nm occurs in the last 30 min. Concurrent DLS measurements show that the average droplet size decreases continuously. Each point in Figure 4.4 (b) indicates the mean and standard deviation of the droplet sizes observed in three evaporation experiments. As the average droplet size decreases, the shift of surface plasmon peak increases. At the beginning it is slow, but increases more rapidly at the end of the evaporation process.

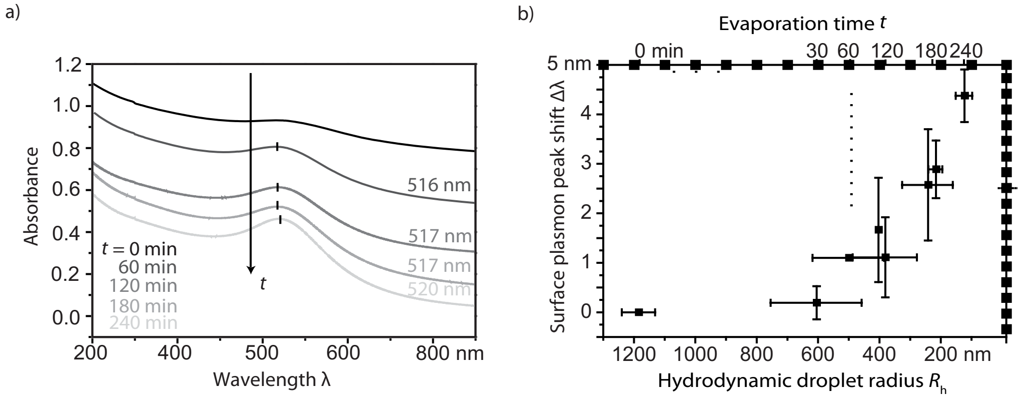

Figure 4.4: Analysis of the cluster formation mechanism by UV-Vis spectroscopy - (a) Samples were taken from the evaporating emulsion and analyzed for the position of the particles' surface plasmon peak. (b) The shift in the position of the SPR peak was correlated with the average droplet size determined through DLS. The shift is important towards the end of the evaporation process when the droplet size decreases rapidly.

Small-angle X-ray scattering (SAXS) can distinguish a particle shell at the liquid-liquid interface from compact clusters, therefore an assembly experiment was performed at the synchrotron facility in Grenoble (ESRF). First, scattering experiments were performed on nanoparticles in pure hexane. The SAXS Utilities software of ESRF [91] was used to obtain radius and polydispersity of the nanoparticles. Those measurements on nanoparticles in pure hexane confirmed the geometry of the nanoparticles with a radius of $3.55\,\text{nm} \pm 0.33\,\text{nm}$. Figure 4.5 shows the fit of the reference scattering data with the solid sphere model implemented in the program.

This data was then used to calculate a Form Factor $F(q)$ of the nanoparticles. The Form Factor $F(q)$ of the nanoparticles from the reference measurements lets us evaluate the scattering intensity $I(q)$ and obtain a structure factor as $S(q) = \frac{I(q)}{F(q)}$. The

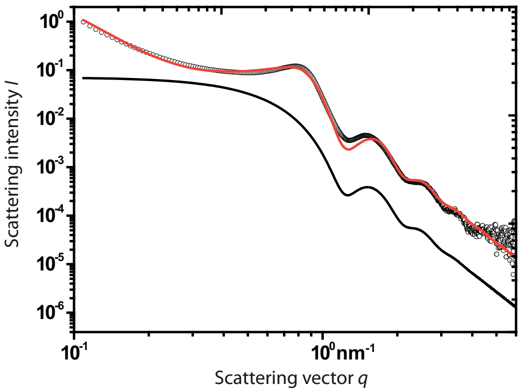

Figure 4.5: Scattering intensity of free gold nanoparticles dispersed in hexane and fit from the hard-sphere model. - The results of the fit (red continuous line) were used to calculate form factors (black continuous line) for the analysis of SAXS data taken on emulsions.

assembly experiment was performed by evaporating the particle-containing dispersion in a nitrogen stream and samples were taken for scattering measurements at fixed intervals. Figure 4.6 (a) shows the time-dependent scattering during the evaporation process. Persistently strong oscillations of the structure factor in the high q region ($q > 0.5$ nm^{-1}) indicate the presence of nanoparticles with a narrow size distribution that agrees with reference measurements on the gold nanoparticle dispersion (particle radius $r = 3.55$ nm $\pm$ 0.33 nm), while no oscillations are visible at lower $q < 0.1$ nm^{-1}. A steady decrease of $I(0)$ can be observed and indicates the shrinking droplets. The oscillations in the low q region reflects the unchanged nanoparticles.

From the $I(q)$ curves obtained by SAXS measurements the static structure factor $S(q)$ was determined for the evaporating particle-containing emulsion during the evaporation process. Figure 4.6 (b) shows the evolution of the structure factor of the emulsion during the evaporation process. Towards the end of the process, a peak appears around 0.6 nm^{-1}. We attribute this peak to the formation of nanoparticle clusters. This peak shifts to increasing q_c upon further evaporation. This shift corresponds to the formation of nanoparticle clusters with decreasing particle-particle distances, where the particle-particle distance d is roughly related to the peaks' positions as $d_c \approx \frac{2\pi}{q_c}$. As the droplets shrink, the particles are compressed until a maximum state, which leads to a peak around $q_c \approx 0.88$ nm^{-1}. This peak corresponds to a particle spacing of 7.2 nm, which is actually slightly below the value of $d_c \approx 7.7$ nm observed in TEM images of

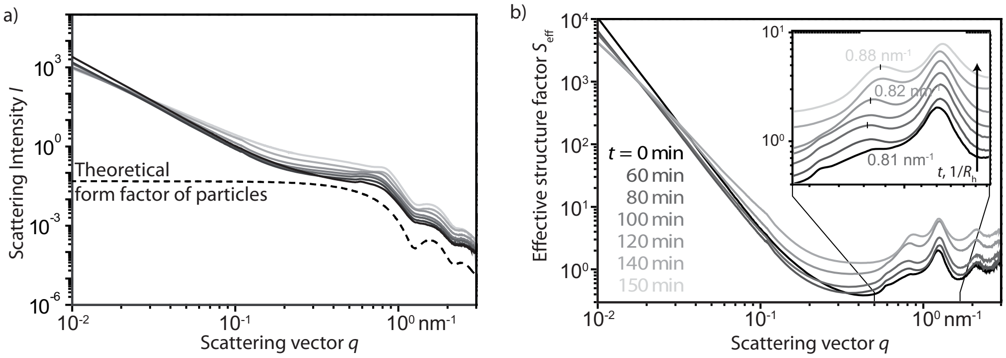

Figure 4.6: Scattering intensity and structure factor of an evaporating particle-containing emulsion - Small-angle X-ray scattering was also performed on samples at regular intervals. The structure factor was determined by dividing the scattered intensity of the emulsion by the form factor F(q) of the free gold nanoparticles.

dry supraparticles.

4.3 Discussion

Figure 4.2 shows the structure of our supraparticles. As it was described in the previous section, some elements of the supraparticles' internal structure remind of icosahedral atomic clusters [96]. We therefore compared the supraparticles to minimum-energy clusters of particles interacting with Lennard-Jones potentials. Theoretical cluster structures from the Cambridge Cluster Database and other sources [97, 98] were cacultated. The database contains numerically established energy minima of the positions of 3 to 1000 particles with LJ potentials inside clusters. An algorithm analyzes the predicted cluster geometries for their outer facets and projects them onto a plane that is parallel to the facet. The resulting catalogue of projections (see Appendix A) was then manually compared to the electron micrographs of supraparticles as shown in Figure 4.7.

The supraparticles matched the predicted projections and the agreement fits surprisingly well, in particular when considering the drying process prior to TEM analysis. The LJ-like nanoparticle clusters we found include icosahedral and decahedral geometries. These cannot be created by cutting face-centered cubic particle packings and many of them strongly deviate from spheres. Such geometries can neither be explained

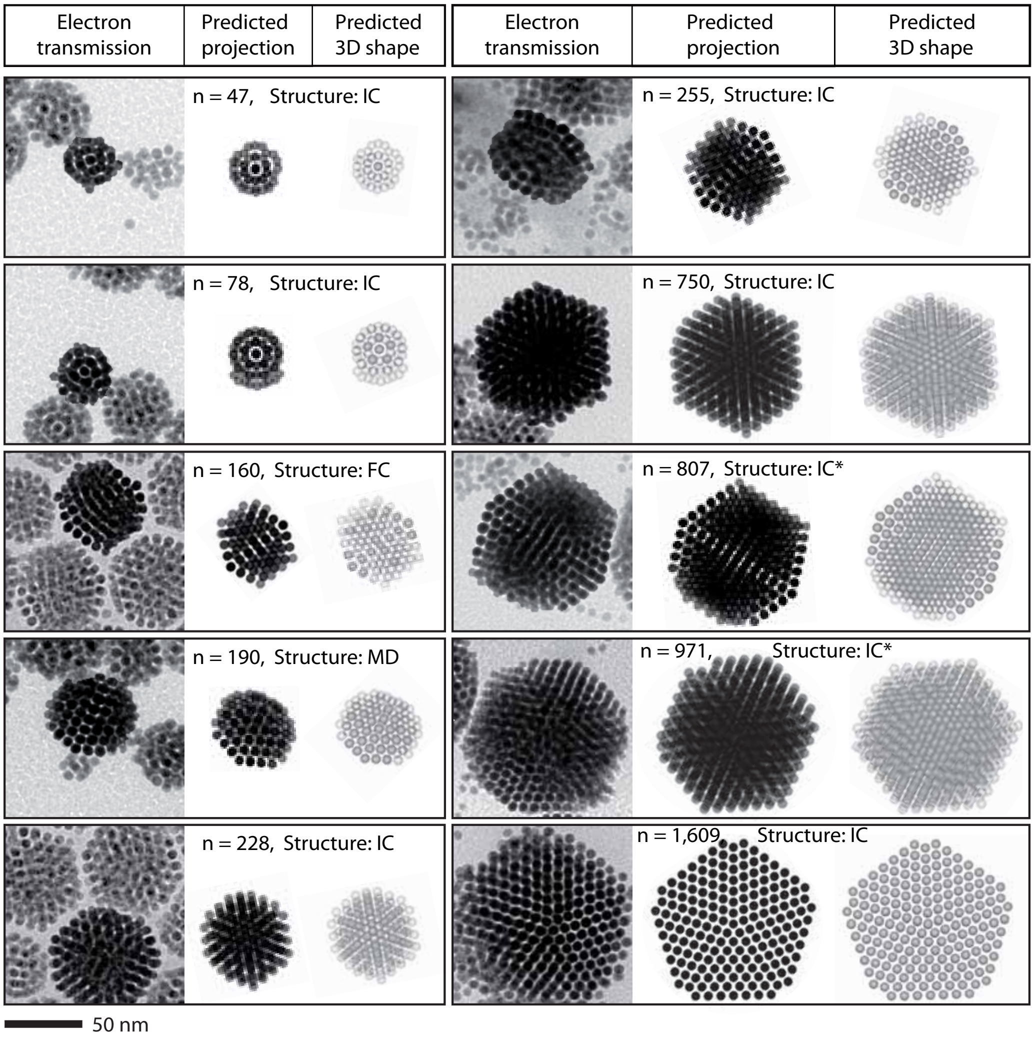

Figure 4.7: Comparison of transmission electron micrographs to projections and three-dimensional renderings of clusters theoretically predicted for particles with Lennard-Jones potentials - In each box, n indicates the number of particles in the predicted cluster. We observed supraparticles having an icosahedral core with a Mackay overlayer ("IC"), an icosahedral core with an anti-Mackay overlayer ("FC"), complete Marks decahedra ("MD") and such having an icosahedral core with a Mackay overlayer and a central vacancy ("IC*") [99–101]

by simple space-filling arguments (which would lead to pieces of densest fcc packing) nor by simple templating of the spherical droplets. Note that clusters such as LJ 1609 cannot form by addition of particles to smaller clusters such as LJ 807. Given the limited interaction lengths between the nanoparticles, which are much smaller relative to the particle diameters than interactions between atoms, formation of such different geometries can only be explained by a mobile intermediate state. Although our procedure is insufficient to establish a strict bijective mapping, it is extremely unlikely that multiple matches would occur incidentally: the twinning planes, single-crystal regions and overgrown layers of the clusters yield tell-tale features in the projections that make the identification robust and reliable.

Manoharan et al. [29] reported that microparticles form regular clusters in evaporating droplets because they are confined to the liquid-liquid interface and collapse when the liquid evaporates. In the absence of this templating effect, they found less regular structures [85]. We therefore assessed whether the nanoparticles in our process segregate to the interface at any point of the assembly process. Interfacial energy reduction by particles [102, 103] and the inwards-moving liquid-liquid interface during evaporation [104] can both cause interfacial templating. We measured the interfacial tensions between the disperse and continuous phases, hexane and water, in pendant droplet experiments and found (in agreement with Glaser et al. [105]) a value of 37 mN/m for a Pickering system with nanoparticles at the interface, considerably below the native interfacial energy of 53 mN/m, but above the interfacial tension of 3 mN/m in the presence of Triton-X 100 at concentrations above the critical micelle concentration.[1] It is therefore energetically unfavorable for the nanoparticles to segregate to the interface.

In a drying droplet, the liquid-liquid interface moves inwards and collects particles, while diffusion will redistribute them throughout the volume. The Peclet number compares these effects [104]:

$$Pe = \frac{R^2}{D\tau} \tag{4.2}$$

where R is the radius of the droplet, D is the diffusion coefficient of the particles in the liquid and τ is the time required for a droplet to evaporate. If $Pe \ll 1$, nanoparticles have time to redistribute inside the droplet by diffusion but if $Pe \gg 1$, particles cannot diffuse to the remaining volume and will accumulate at the droplet interface. In a

---

[1] It has been reported that the interface of small hexane droplets in an aqueous phase shows an even lower surface energy [106].

typical assembly process, we have an evaporation time $\tau = 240$ min, $R = 1180$ nm (the radius directly after emulsification) and the nanoparticles' diffusion constant (from DLS) is $D = 2.3 \times 10^{-10}$ m^2/s. This corresponds to $Pe = 4.2 \times 10^{-7}$, which indicates a homogeneous particle distribution inside the droplets.

The above results suggest that interfacial templating is not the source of order in supraparticles. Free energy minimization is another mechanism that could drive structure formation by maximizing next neighbors and particle-water distances. The short interaction lengths of Van der Waals forces would then imply assembly at low particle-particle and particle-interface distances. To check this hypothesis *in situ* surface plasmon spectroscopy and small-angle X-ray scattering measurement can detect at which stage agglomerates form. To analyze our SPR analysis of evaporating emulsions, we calculate the theoretical evolution of the SPR peak using the effective medium approximation (EMT) [31, 35], assuming homogeneously distributed particles. We assume identical droplets and use the Maxwell-Garnett expression to calculate an effective dielectric constant ϵ_{eff} of a droplet that contains the solvent with dielectric constant ϵ_m and particles with dielectric constant ϵ^{∞}:

$$\epsilon_{eff} = \epsilon_m \left(1 + \frac{3\phi\beta}{1 - \phi\beta}\right) \text{ , } \textbf{with } \beta = \frac{\epsilon^{\infty} - \epsilon_m}{\epsilon^{\infty} + 2\epsilon_m} \tag{4.3}$$

where ϕ is the volume fraction of particles.

We can use the droplet size information from DLS to calculate a theoretical surface plasmon shift assuming homogeneously distributed particles in the droplets. If the shift increases below the predicted value, agglomeration is the most likely cause. To obtain the original number of particles per droplet, we analyze the size of the final "droplets" that only contain particles and no solvent: After 4 hours, the size of the droplets stabilized around 123 nm. In supraparticles, particles are densely packed with approximate packing density of $f \simeq 0.688$ as estimated by MacKay [99]. The supraparticles are surrounded by surfactant molecules that increase their hydrodynamic radius. The size of micelles formed by the surfactant, Triton X-100, equals 3.2 nm. We estimate the radius of the supraparticles R simply by subtracting this size from the hydrodynamic diameter. The number of particles per droplets is then $n = f \times \left(\frac{R}{r}\right)^3$ with a nanoparticle radius r that has to take into account the interdigitation of the ligands. TEM imaging indicates that the average interparticle distance between agglomerated nanoparticles surfaces is 2.52 nm, somewhat smaller than the thickness of two ligand monolayers, while the gold core radius equals 3.2 nm. The relevant radius with the interdigitation taken into account therefore amounts to 4.46 nm. On average, each cluster contains 13 179 nanoparticles.

In our simple model, this number remains constant during the evaporation process. The increasing particle concentration in the shrinking droplets changes the dielectric environment during evaporation and causes the surface plasmon shift. Using the EMT equation to replace the dielectric function of the medium ϵ_m by the effective medium ϵ_{eff} the surface plasmon frequency of particles in a droplet with a volume fraction of particles ϕ is then:

$$\begin{aligned} \lambda_{spr} &= 2\pi c\sqrt{\frac{m_e\epsilon_0}{Ne^2}(\epsilon^\infty + 2\epsilon_{eff})} \\ &= 2\pi c\sqrt{\frac{m_e\epsilon_0}{Ne^2}\left(\epsilon^\infty + 2\epsilon_m\left(1 + \frac{3\phi\beta}{1-\phi\beta}\right)\right)}. \end{aligned} \tag{4.4}$$

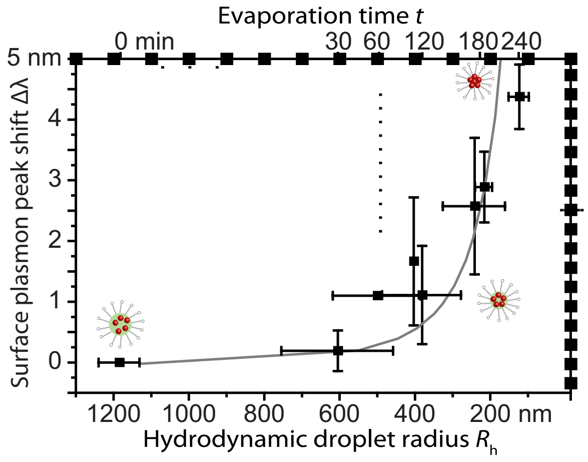

Figure 4.8: Analysis of the cluster formation mechanism by UV-Vis spectroscopy and comparison with theoretical SPR peak caculated from the EMT - The continuous line indicates the theoretical SPR peak for different stages of the evaporation process assuming complete absence of agglomeration.

We can now calculate the theoretical SPR peak for different stages of the evaporation process assuming simple continuous confinement. This is indicated by the continuous line in Figure 4.8. The predictions agree with the experimental observation until the EMT approximation breaks down for the closely packed supraparticles (for a hydrodynamic droplet radius from DLS $R_{\rm H} < 200$ nm). Spectroscopic evidence therefore suggests that supraparticle assembly does not occur by early nucleation and subsequent growth, but in a late stage of evaporation, where particles and interfaces strongly interact.

As it was mentioned in the previous section, SAXS can distinguish a particle shell at the liquid-liquid interface from compact clusters. Figure 4.6 shows the time-dependent scattering during the evaporation process. Persistently strong oscillations in the high q region ($q > 0.5$ nm^{-1}) are observed, while no oscillations are visible at lower $q <$ 0.1 nm^{-1}. A Pickering phase would cause oscillations in the low q-range even for droplets broadly distributed in size, a signature that we did not observe in any of our evaporation experiments. To identify the structure of the emulsion droplet we used the SAXS Utilities software [91] of ESRF to fit our scattering curves using different models.

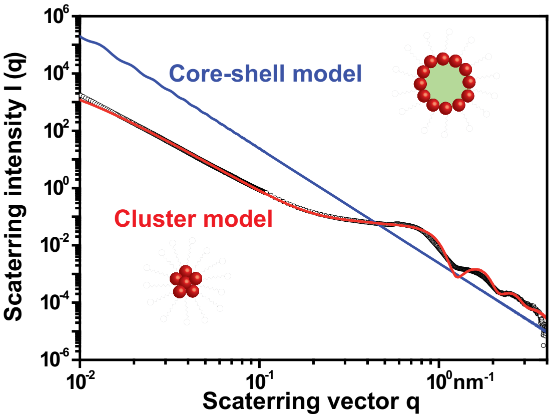

Figure 4.9: Scattering intensity of particle-containing emulsion and comparison with different fit models - Two models were used to fit the scattered intensity of the sample : a cluster model and a core-shell model. The cluster model fits the evolution well.

Figure 4.9 shows the fits of the scattering intensity of an emulsion during the evaporation using two different models, a cluster model and a core-shell model. At all times, the evolution of the scattering intensity clearly differs from that expected for a core-shell arrangement whereas the cluster model fits the evolution well. The hard-sphere clustering model assumes attractive particles and predicts additional scattering $S_c(q)$ to occur when the particles interact and form clusters,

$$S_c(q) = \frac{I_M}{(1+q^2\xi^2)^p}, \tag{4.5}$$

depending on the average mass and characteristic size of the formed clusters that are proportional to I_M and ξ, respectively, and their fractal dimension p. The hard-sphere cluster model fits our $I(q)$ reasonably well in early stages of the evaporation, but fails to predict the emerging peak at q_c. Figure 4.10 shows the evolution of the fit parameters for the data presented in Figure 4.6. As the solvent from the droplets evaporates, the volume fraction ϕ of nanoparticles increases, the correlation length ξ decreases and the fractal dimension p decreases. The increase in the local volume fraction can be attributed to the clustering process. This was expected since when we evaporate the solvent, the nanoparticles are confined inside the droplet. Moreover, The volume fractions ϕ that the model yields are similar to those obtained from SPR studies, albeit somewhat higher. The correlation length (usually connected with the agglomerate sizes) corresponds to the average droplet sizes which become smaller upon evaporation. The decreasing fractal dimension can be interpreted as sign of increasing confinement and density of the forming supraparticles.

Although it has been developed for freely moving particles and not for a confined system of droplets with particles, the fit correctly indicates a steadily decreasing correlation length ξ and even yields a volume fraction of nanoparticles that corresponds to that obtained for the particles in the droplets above (Figure 4.10). That is the reason why we think the hard-sphere clustering model fits our scattering data and suggests correlation lengths that coincide with the droplet diameters and volume fractions that are in line with particles homogeneously distributed in the available volume.

4.4 Summary

In summary, we showed that nanoparticles in emulsion droplets arrange into regular supraparticles by free energy minimization. This is in contrast to the process that Manoharan et al. [29] reported for microparticles in emulsions, which are confined to the liquid-liquid interfaces and collapse into clusters when the liquid evaporates. The structure of our supraparticles is governed by the interparticle potential of metal

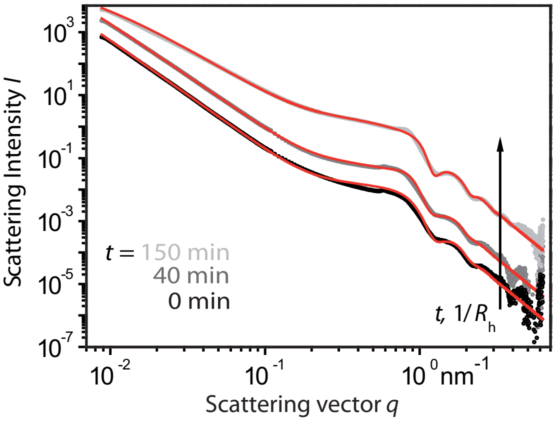

Evaporation time t	Volume fraction ϕ	Correlation length ξ	Fractal dimension p
0 min	0.19	1,053 nm	1.73
20	0.24	761	1.78
30	0.20	640	1.66
40	0.25	523	1.66
50	0.26	459	1.65
60	0.25	277	1.68
70	0.26	221	1.67
80	0.27	229	1.66
90	0.25	165	1.63
100	0.25	159	1.64
110	0.27	150	1.62
120	0.33	120	1.62
130	0.35	140	1.54
140	0.36	117	1.47
150	0.35	159	1.40

Figure 4.10: Cluster-model fits of SAXS from evaporating, particle-containing emulsions. - The cluster model (red continuous lines) fits the data (circles) surprisingly well given that it was derived for freely moving particles. The volume fractions ϕ that the model yields are similar to those obtained from SPR studies, albeit somewhat higher. The correlation length (usually connected with the agglomerate sizes) corresponds to the average droplet sizes. The decreasing fractal dimension can be interpreted as sign of increasing confinement and density of the forming supraparticles.

nanoparticles that resemble Lennard-Jones potentials [107, 108] and the influence of the liquid-liquid interface. In contrast to destabilized nanoparticles with strongly attractive potentials that quickly agglomerate in a nucleation-and-growth mechanism, the particles in the emulsion droplets retain their mobility as the attraction between the particles increases. They have time to find their energetically optimal position in the increasingly dense, non-agglomerated mobile precursor state before they are finally quenched when their ligand shells interdigitate. The liquid-liquid interface gently pushes the particles into a dense geometry, thus funneling the particles into their minimum-energy positions while avoiding secondary minima such as multiple twinned fcc crystals. We did not study whether this process depends on the exact energetic state of the specific cluster geometry. It would be interesting to see whether those supraparticles containing “magic” numbers of particles are more stable than others, as it is the case for atomic clusters.

Technologically, supraparticles are interesting because they are fully defined by the number of nanoparticles involved. The process used here is general and compatible with all moderately attractive nanoparticles, for example, semiconductor quantum dots. To create fluorescent suparparticles, for example, one would measure the diffusion constant of the desired quantum dots, analyze their tendency to segregate to the interface and choose appropriate evaporation parameters and surfactants.

Chapter 5

Characterisation of surfactant-stabilized emulsions containing nanoparticles

This chapter was published in *Soft Matter 2014 10 (11), 1696-1704.* [109]

5.1 State of the art

The liquid-liquid interface plays an important role in the formation of the supraparticles. Structure formation in particle-containing emulsions strongly depends on the interactions between nanoparticles and the liquid-liquid interface. Changing the interfacial conditions will probably influence the structure of the resulting supraparticles.

The ability of surfactants to lower liquid-liquid interfacial tensions is a key property that makes them useful in the preparation of emulsions. Surfactants are driven by their amphiphilic nature to accumulate at oil-water interfaces and lower the oil-water interfacial tension. They are widely used and find applications in the food [110], cosmetic [111], paint [112], polymer [112] and oil industries [113].

Both surfactants and nanoparticles can adsorb to the liquid-liquid-interface. In doing so, surfactants and particles alone [61] and their combinations [114, 115] stabilize emulsions. Depending on which components segregate to the liquid-liquid interface, structure formation follows different routes during the evaporation of the dispersed solvent.

5. CHARACTERISATION OF SURFACTANT-STABILIZED EMULSIONS CONTAINING NANOPARTICLES

Previous studies on nanoparticle-containing emulsions have focused mainly on the effects of particles and surfactants on surface tension and emulsion stability. Ma et al. studied the assembly of anionic and cationic surfactants and negatively charged silica nanoparticles at trichloroethylene-water interface. Silica nanoparticles increased the efficiency of an anionic surfactant, SDS, but had no effect when combined with non-ionic surfactants. The authors concluded that repulsive interactions between SDS and nanoparticles promote surfactant adsorption at the interfaces [116]. Whitby et al. studied the addition of SDS in dodecane-in-water "Pickering" emulsion stabilized by silica nanoparticles [117]. At SDS concentrations above the cmc, the rate of flocculation and creaming were enhanced. Some years later, Vashisth et al. used confocal fluorescence microscopy and cryogenic scanning electron microscopy to show that adding SDS to the same Pickering emulsions leads to the displacements of nanoparticles from the interface at surfactant concentration above the cmc. At surfactant concentrations below the cmc, mixtures of particles and surfactant populated the liquid-liquid interfaces [118].

Recently, complex behaviors of surfactants (lecithin and oleylamine) and silica nanoparticles were observed for oil-in-water emulsions [119]. In the presence of oleylamine, the interfacial tension of the oil-water emulsion increases when the concentration of silica nanoparticle in the oil phase increased. Eskandar et al. suggested that the attraction between oppositely charged nanoparticles and surfactants results in the adsorption of surfactant on the nanoparticles' surfaces and reduces the surfactant density at the oil-water interface which means that additional surfactants are needed to re-etablish the equilibrium at the interface of the emulsion.

In this chapter, gold nanoparticles are used to probe structure formation in oil-in-water emulsions containing different surfactants. When slowly evaporating the oil phase of particle-containing emulsions, conformational changes can be observed as relative surfactant and particle concentrations increase. The results compare the behavior of macroscopic oil-water interfaces in the presence of the same surfactants and nanoparticles. Conclusions on the relationship between interfacial tensions, adsorption of nanoparticles at the oil-water-interface, and the morphology of the particle superstructures formed can be drawn.

5.2 Results

Three aspects of particle-containing hexane-in-water emulsions were analyzed: the effect of surfactants and particles on the surface tension of macroscopic hexane-water interfaces, the distribution of particles in emulsion droplets, and the changes in distribution and agglomeration of particles when the dispersed phase was evaporated.

5.2.1 Interfacial tension of macroscopic drops

Only particles and surfactants that adsorb at the oil-water interface can change its interfacial tension. Figure 5.1 shows the hexane-water interfacial tension as a function of surfactant and nanoparticle in bulk that were calculated from the shapes of macroscopic oil drops. The presence of gold nanoparticles in hexane without any surfactant decreased the interfacial tension from 53 mN/m to 37 mN/m, consistent with the results of Glaser et al.[105] and indicating that nanoparticles segregate to the interface.

We added surfactants to the aqueous phase at concentrations just above cmc (see Table 3.2). The additon of SDS in the absence of particles (green columns) reduced the interfacial tension to 11.8 mN/m, whereas the addition of Tween 85 and Span 20 only reduced the interfacial tension to 30.9 mN/m and 34 mN/m, respectively. The observed tensions are slightly above literature values measured using the ring method of de Nouy [120, 121]. This was expected since it has been demonstrated that interfacial tension of microscopic droplets may differ using different techniques [122]. This difference is due to the equilibrium partitioning of the surfactant which depends on the surface-to-volume ratio of the fluid. Using the ring method, the surface-to-volume ratio is higher leading to an increase of interfacial coverage by surfactant. Hence, the equilibrium interfacial tension will decrease going from pendant drop experiment to the ring method.

The pink columns in figure 5.1 show the interfacial tensions for oil drops containing nanoparticles in water containing surfactants. The particles did not change the tension of oil droplets SDS solution. For Tween 85 and Span 20, the interfacial tension decreased respectively to 15.3 mN/m and 14.1 mN/m, values that are below both particle-containing hexane in water and pure hexane in the surfactant solutions.

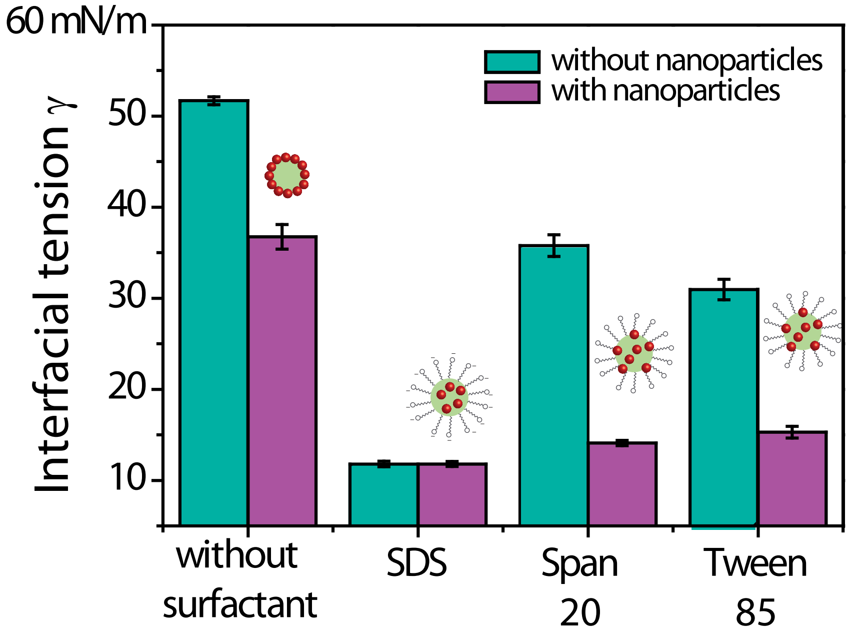

Figure 5.1: Equilibrium interfacial tensions of hexane-water interfaces with different surfactants and particles - All values are calculated from the shape of macroscopic pendant drops. Surfactants were introduced into the continuous phase (water) at concentrations above the critical micelle concentration, gold nanoparticles were introduced into the dispersed phase (hexane).

5.2.2 Particle distribution in microscopic droplets

It is difficult to perform tensiometry on the microscopic droplets of an emulsion. Instead, we used surface plasmon spectroscopy to observe the migration of nanoparticles inside the droplets. The method indicates close packing of nanoparticles as they occur when they densely populate the oil-water interface.

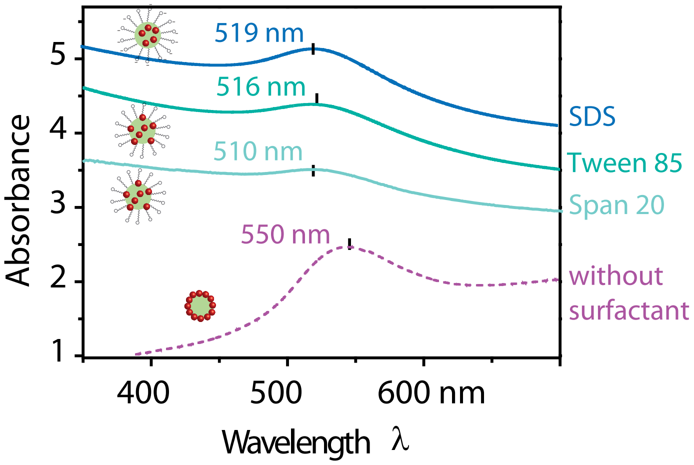

Figure 5.2: UV-Vis spectra of emulsion containing AuNPs just after emulsification - Emulsions containing surfactants exhibited a surface plasmon resonance peak around 517 nm. The peak is shifted to higher wavelengths in the abscence of surfactants.

Figure 5.2 shows the UV-Vis spetra of particle-containing emulsions for different surfactants. We evaluated the position of the surface plasmon resonance (SPR) peak just after emulsification. In the absence of any surfactant, the original peak position of 520 nm drastically red-shifted to 550 nm, indicating a localized concentration increase of the nanoparticles that can be interpreted as migration to the interface. In the presence of SDS, no shift was observed, consistent with nanoparticles that remain dispersed in the bulk. Surprisingly, emulsions containing Tween 85 or Span 20 did not exhibit any shift of the SPR signal, despite of their effect on macroscopic interfacial tension.

5.2.3 Evaporation of oil from microscopic droplets

The nanoparticle concentration in the oil phase is much lower than the surfactant concentration in the aqueous phase. It is interesting to know whether the emulsion structure changes for higher concentrations. We increased the particle concentration by slowly evaporating the oil phase while constantly monitoring the SPR. Concurrent DLS measurements were performed to determine the evolution of the droplet size during the evaporation. The evaporation rate was kept low to create quasi-static, near-equilibrium situations.

Figure 5.3 shows the SPR evolutions during the evaporation of emulsions containing different surfactants. Each point in the graphs indicates the mean and standard deviation of the droplet size and surface plasmon peak shift observed after the same evaporation time in three separate experiments. The insets show the SPR peaks recorded during the evaporation process.

Larger droplets that are present at the beginning of the experiment scatter the light more strongly than the partially evaporated droplets at later stages, which explains the increasing overall transmission (see insets). The SPR peak becomes clearly visible after around 120 min, when the background scattering has decreased sufficiently.

For emulsions stabilized by SDS or Tween 85 (figure 5.3 (a) and (b)), the average droplet size decreased continuously. Concurrently, the SPR peak shifted, with a marked increase in rate towards the end of the evaporation process. Very similar evolution of droplet size and SPR peak were observed for emulsions stabilized by Triton X-100 (*chapter 4*). They coincide with theoretically predicted values that were obtained using the effective medium approximation (EMT) assuming homogeneously distributed particles. The calculated shifts are indicated by the continuous lines in figure 5.3 (a) and (b).

For emulsions stabilized by Span 20 (figure 5.3 (c)), the average droplet size increased during the first 180 min and then decrease until the end of the evaporation. The SPR shift stalled while the droplet size increased. The final shift was comparable to that observed for other surfactants.

While SPR spectroscopy only indicates local concentration changes, SAXS measurements provide details on their distribution. Particle-containing emulsions were evaporated at the synchrotron and samples were taken for scattering measurements at fixed intervals. References were obtained from nanoparticles in pure hexane. The SAXS Utilities software of ESRF was used to fit the reference data and determine radii of 2.95 nm ± 0.10 nm.

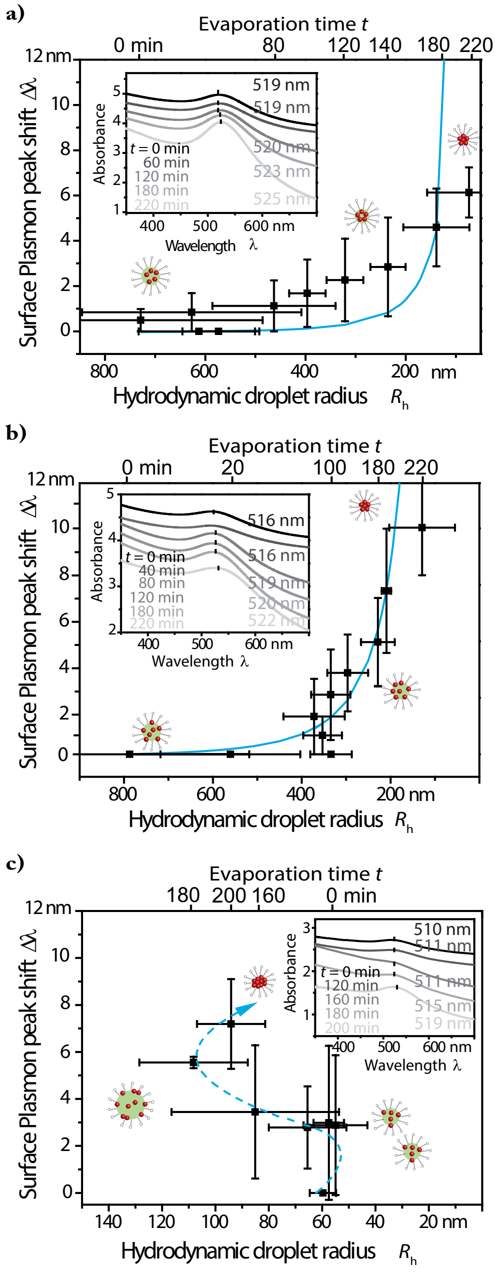

Figure 5.3: Analysis of the cluster formation mechanism by UV-Vis spectroscopy - Samples were taken from evaporating emulsions containing (a) SDS, (b) Tween 85 or (c) Span 20 and analyzed for the position of the particles' surface plasmon peak. For samples containing SDS and Tween 85, the SPR peak is shifted only towards the end of the evaporation process when the droplet size decreases rapidly. The continuous lines in graphs (a) and (b) indicate the shift predicted using an EMT model for homogeneously distributed particles. For samples containing Span 20 (c), the radius of the droplet increased initially (with fixed SPR) and then decreased (with increasing SPR shift). The dotted line in the graph indicate the evolution of the size of the droplet as a function of time.

The evolution of scattering during the evaporation process for emulsion containing SDS, Tween 85 and Span 20 are shown respectively in figure 5.4, 5.5 and 5.6. All samples exhibited strong oscillations in the high q-region ($q > 0.5\ \mathrm{nm}^{-1}$) that indicate nanoparticles with a narrow size distribution. In the low q region ($q < 0.1\ \mathrm{nm}^{-1}$), where larger structures dominate, no oscillations were visible.

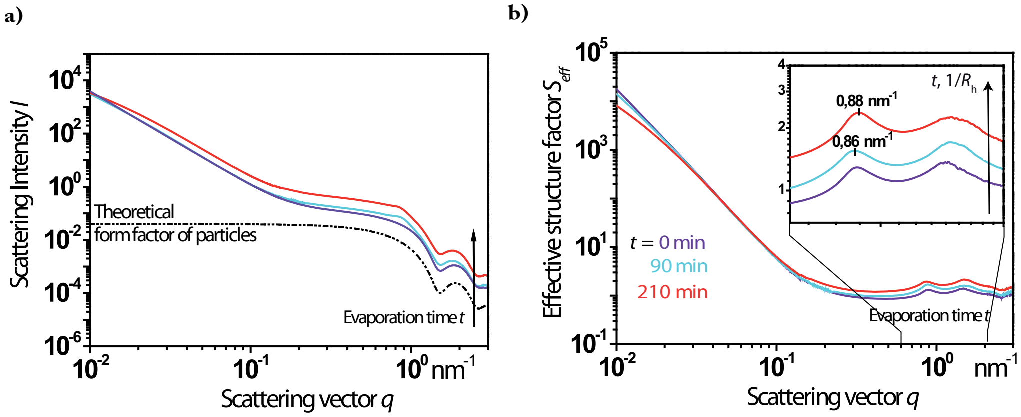

Figure 5.4: Analysis of the cluster formation mechanism by Small-angle X-ray scattering for emulsion containing SDS - Samples were taken from the evaporating emulsion and analyzed. At all times, the evolution of the scattering intensity for sample containing SDS is clearly similar to nanoparticle clusters formed by free energy minimisation.

We calculated a structure factor $S(q)$ from the radially integrated scattering intensity $I(q)$ using

$$S(q) = \frac{I(q)}{F(q)} \tag{5.1}$$

with a theoretical form factor $F(q)$ calculated from the particle geometry obtained in reference measurements. Figures 5.4(b), 5.5-(b) and 5.6(b) show the evolution of the structure factor of three emulsions during the evaporation process.

5.2.4 Structure of nanoparticle clusters

After all oil has evaporated, particle agglomerates remain stabilized in water by the surfactant. These agglomerates can be internally ordered ("supraparticles" or "clusters" [93]) or disordered. Figure 5.7 shows TEM images of agglomerates formed in emulsions containing differents surfactants. Emulsions containing SDS yielded a large fraction of

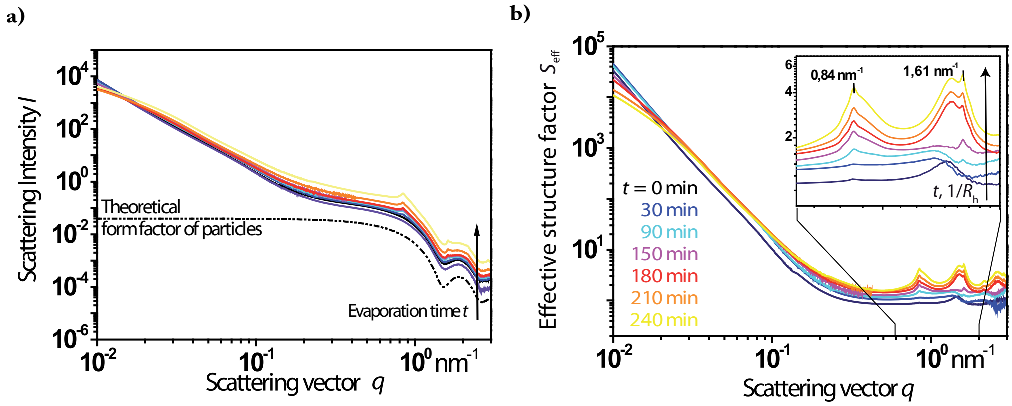

Figure 5.5: Analysis of the cluster formation mechanism by Small-angle X-ray scattering for emulsion containing Tween 85 - Samples were taken from the evaporating emulsion and analyzed. At all times, the evolution of the scattering intensity for sample containing Tween 85 is clearly similar to nanoparticle clusters form by free energy minimisation. However, two peaks in the structure factor occur early and remain at constant q during the evaporation process.

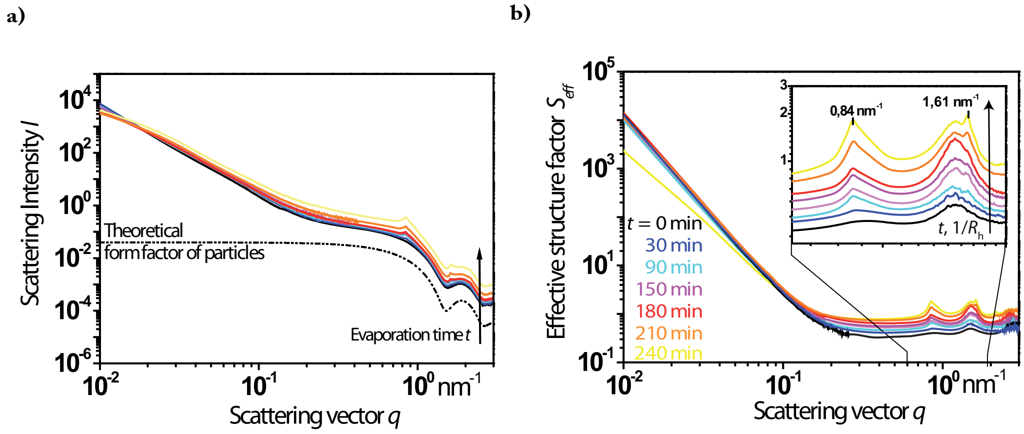

Figure 5.6: Analysis of the cluster formation mechanism by Small-angle X-ray scattering for emulsion containing Span 20 - Samples were taken from the evaporating emulsion and analyzed. At all times, the evolution of the scattering intensity for sample containing Span 20 is cleary similar to nanoparticle clusters form by free energy minimisation. However, two peaks in the structure factor occur early and remain at constant q during the evaporation process.

supraparticles. Most of them were structurally similar to clusters formed from particles interacting with Lennard-Jones potentials and are reminiscent of the clusters formed from Triton X-100 (figure 4.2). Tween 85 and Span 20 (figure 5.7 (b) and (c)) yielded a large fraction of isolated particles and irregularly shaped agglomerates. Small numbers of supraparticles were present, but they were composed of crystalline ”grains” having fcc structure rather than having Lennard-Jones-like features.

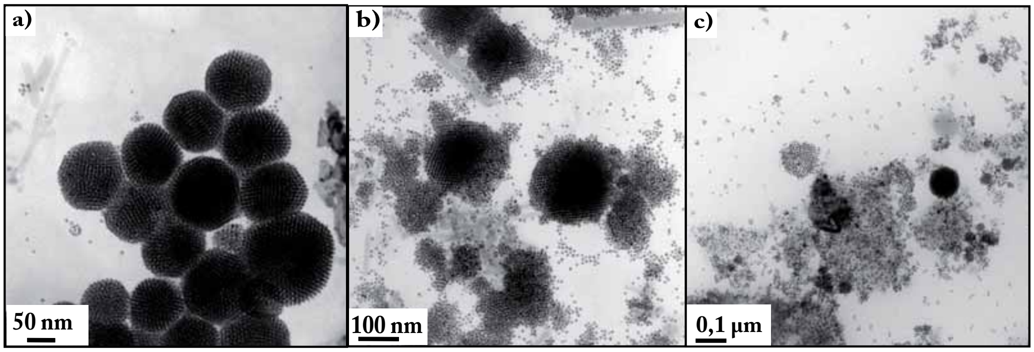

Figure 5.7: Transmission electron micrographs of nanoparticle agglomerates formed in emulsion droplets - Supraparticles with Lennard-Jones-cluster geometries form in emulsions stabilized SDS (a). Emulsions stabilized by Tween 85 (b) and Span (c) yielded disordered agglomerates and smaller amounts of agglomerates with regions that exhibit fcc packing.

5.3 Discussion

Depending on the surfactant/nanoparticle combination, particles segregate or not to the interface. Both the macroscopic surface tension of hexane-water interfaces and the microscopic distribution of particles in emulsion droplets depend on the surfactant-particle combination. We believe that free energy minimization leads to a competition between particles and surfactants for adsorption sites at the oil-water interface. In the absence of surfactant, particles populate the interface. For interfacial tension measurement, it seems that SDS reduces the interfacial tension so low that it is energetically unfavorable for the nanoparticles to segregate at the interface. Moreover no shift in the SPR peak is observed leading to the conclusion that nanoparticles are dispersed in the oil phase while SDS stabilized the droplet. The most efficient surfactant, SDS, fully displace particles from the interface. Interfacial energy measurements, surface plasmon and small-angle x-ray spectroscopy are all consistent with this picture.

Less efficient surfactants such as Tween 85 and Span 20 show surprising behavior when mixed with particles. The mixtures lower the interfacial tension more than pure particles and the surfactants do not fully block the interface. A mixture of particles and surfactants apparently forms at the interface that lowers the macroscopic interfacial tension more than each of its components. Similar synergistic effects have been reported for kaolinite clay (with an equivalent spherical diameter of 0.2 µm) at the hexadecane-water interface in the presence of dodecylamine [123] and for the paraffin-water interface in the presence of oleylamine in the oil phase and silica nanoparticles (7 nm diameter) in the aqueous phase [119].

The synergistic arrangements of particles and surfactants seem kinetically easy to reach. Tween 85 is a polymer (average molecular weight around 1838 g/mol according to the vendor) with a diffusion constant that is at least 1.7 times below that of Span 20, a smaller sorbitan monooleate (molecular weight around 346 g/mol). Both systems rapidly reached stable interfacial tensions in pendant droplets (after 100 s) but not as fast as the system containing only nanoparticles (around 60 s).

Despite of the relatively low interfacial energy of Span 20-particle-combinations, the resulting emulsions broke when slowly evaporating the oil phase (figure 5.3 c). Industrially, Span 20 is used as co-emulsifier together with other surfactants; while particles can play part of this role, their combination did not yield stable emulsions. Tween 85 yielded more stable emulsions, but only SDS provided small droplets that remained small over extended periods of time.

To determine the morphology of our emulsion systems, *in situ* surface plasmon spectroscopy was used to detect at which stage agglomerates form. The arrangement of nanoparticles depends on the distribution of particles inside the evaporating droplets. The simplest model assumes a homogeneous dispersion of particles inside the oil droplets. We calculated the surface plasmon peak shift expected for this configuration using Maxwell-Garnett theory [31, 93] and compared the predictions to the measured surface plasmon shifts (figure 5.3). Emulsions containing Span 20 were too instable to compare to the model but exhibited a continuously increasing shift that suggests a uniform particle distribution in the droplets. For emulsions containing SDS, there is good agreement between predicted and measured shifts. This rules out early agglomeration of the particles and is consistent with SDS blocking the oil-water interface.

Surprisingly, the EMT model also fits the data of Tween 85. We know that AuNP segregate to macroscopic oil-water interfaces in the presence of this surfactant. One may assume that the situation changes for small emulsion droplets and the particles remain in the bulk oil. A more likely explanation of the fit is, however, that the density of nanoparticles at the interface apparently is too low to cause a discernible SPR shift. We estimate a maximum density of 0.39 nanoparticles per square nanometer at the interface of the droplets, corresponding to a minimum distance of 12 nm between the particles.

Small-angle x-ray scattering (SAXS) of shrinking, particle-containing emulsions is dominated by the scattering of AuNP and provides additional structural insights. Time-dependant scattering intensity of our samples showed, for all samples, strong oscillations of the structure factor in the high q region but no oscillations in the low q region. A Pickering phase would cause oscillations in the low q range even for droplets broadly distributed in size. We can rule out such structures. At all times, the evolution of the scattering intensity could be fitted by the cluster model, suggesting particles that are confined but do not form shells (see figure 5.8).

The hard-sphere clustering model [124] assumes attractive particles and predicts additional scattering $S_c(q)$ when the particles interact and form clusters:

$$S_c(q) = \frac{I_M}{(1 + q^2\xi^2)^p}, \tag{5.2}$$

where I_M is proportional to the average mass of the cluster, ξ is proportional to the characteristic cluster size and p corresponds to the fractal dimension. As the solvent from the droplets evaporated, the volume fraction ϕ of nanoparticles increased, the correlation length ξ decreased and the fractal dimension p decreased. The increase in the local volume fraction can be attributed to agglomeration. The correlation length corresponds to the decreasing average droplet sizes during evaporation. The decreasing fractal dimension can be interpreted as sign of increasing confinement and density of the forming supraparticles. The hard-sphere clustering model fits our scattering data and suggests correlation lengths that coincide with the droplet diameters and volume

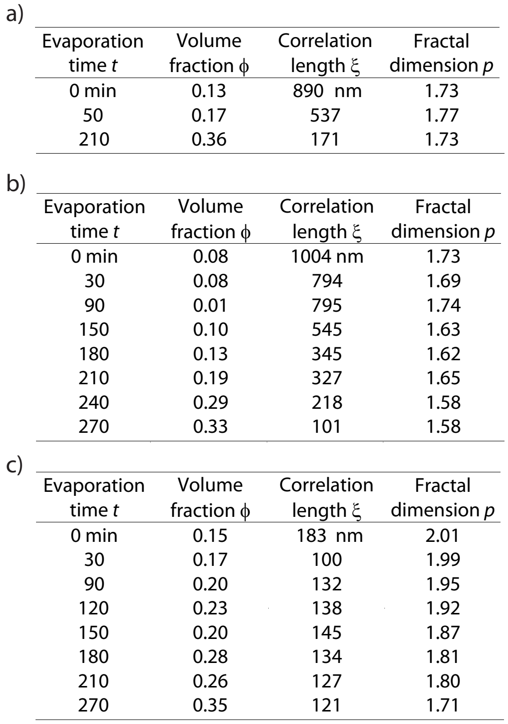

a)

Evaporation time t	Volume fraction ϕ	Correlation length ξ	Fractal dimension p
0 min	0.13	890 nm	1.73
50	0.17	537	1.77
210	0.36	171	1.73

b)

Evaporation time t	Volume fraction ϕ	Correlation length ξ	Fractal dimension p
0 min	0.08	1004 nm	1.73
30	0.08	794	1.69
90	0.01	795	1.74
150	0.10	545	1.63
180	0.13	345	1.62
210	0.19	327	1.65
240	0.29	218	1.58
270	0.33	101	1.58

c)

Evaporation time t	Volume fraction ϕ	Correlation length ξ	Fractal dimension p
0 min	0.15	183 nm	2.01
30	0.17	100	1.99
90	0.20	132	1.95
120	0.23	138	1.92
150	0.20	145	1.87
180	0.28	134	1.81
210	0.26	127	1.80
270	0.35	121	1.71

Figure 5.8: Cluster model fit results - The fits results were determined from evaporation emulsions containing SDS(a), Tween 85(b) and Span 20(c).The volume fractions ϕ that the model yields are similar to those obtained from SPR studies. The correlation length corresponds to the average droplet sizes determined through DLS with a constant decrease for emulsion containing SDS or Tween 85 and a small increase following a decrease for emulsion containing Span 20. The decreasing fractal dimension can be interpreted as a sign of increasing confinement and density of the forming supraparticles.

fractions that coincide with particles homogeneously distributed in the available volume (see figure 5.8).

For the emulsion stabilized by SDS (figure 5.4 (d)), a SAXS peak appeared around 0.8 nm^{-1}. The peak shifted to increasing q_c until all dispersed solvent had evaporated. It probably corresponds to the formation of supraparticles with decreasing particle-particle distances similar to the process we previously reported for emulsions stabilized by Triton X-100. The particle-particle distance d is roughly related to the peaks' positions as $d_c \approx 2\pi q_c$. As the droplets shrink, the particles are compressed to a maximum state, which leads to a peak around $q_c \approx 0.88$ nm^{-1}. This peak corresponds to a particle spacing of 7.2 nm, slightly below the value of $d_c \approx 7.7$ nm observed in TEM.

For emulsion stabilized by Tween 85 and Span 20 however, the peak does not shift to increasing q_c upon further evaporation (Inset in figure 5.5b) and 5.6 b)). We attribute this peak to the formation of agglomerates with constant particle-particle distances. Bragg's law (see equation 4.1) lets us index the peaks [95] from figure 5.9 as belonging to (111) and (311) planes for the peak at $q = 0.84$ nm^{-1} and $q = 1.61$ nm^{-1}, respectively. Both of these planes are characteristic of an fcc packing, a packing that we can also observe on TEM images of the supraparticles (figure 5.7 (b) and (c)). In those two systems, the formation of intermediate aggregates lead to different final supraparticles with FCC facets or having an amorphous structure.

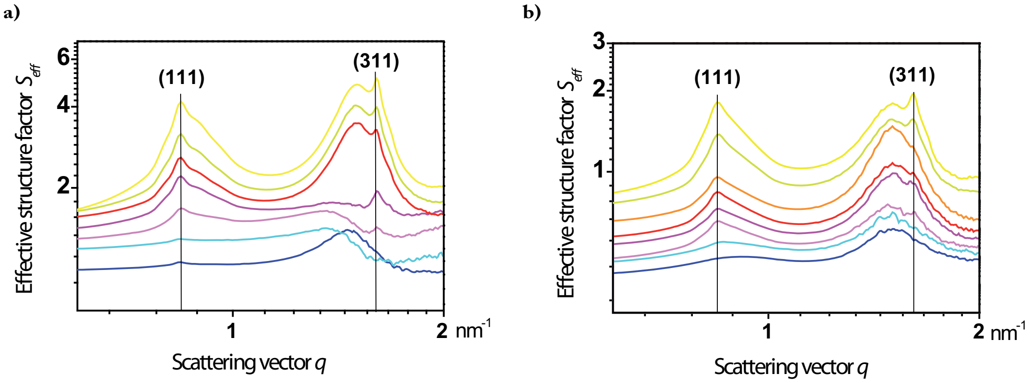

Figure 5.9: Effective SAXS structure factors of samples containing Tween 85 (a) and Span 20 (b) indicating agglomerates with fcc structure. - The maxima are equivalent to Bragg peaks and can be indexed using Bragg's law. They correspond to (111) and (311) planes with d_{111} spacing of 7.4 nm and d_{311} spacing of 3.9 nm.

The results so far suggest two different mechanisms of particle arrangement in the droplets that depend on the surfactant: SDS keeps particles away from the oil-water interface. Particles are compressed in the oil phase and form structures that are dominated by the free energy minimization of particle-particle interactions. Tween 85 and Span 20 do not fully exclude particles from the interfaces. The combined interactions between particles at the interface and particles in the oil phase yield agglomerate with fcc packing.

Transmission electron microscopy supports this picture (figure 5.7). Particle agglomerates formed in emulsions with SDS remind of icosahedra clusters [93, 96]. Tween 85 and Span 20 yield agglomerates having fcc and amorphous structures.

5.4 Summary

In summary, we showed that the structure of nanoparticle clusters formed inside emulsion droplets depends on the choice of the surfactant which influences the stability and structure of particle-containing emulsions. The extreme cases are ”Pickering”-type emulsions that are solely stabilized by particles at the oil-water-interface. At the other extreme, good surfactants such as SDS and Triton X-100 fully block the interface so that all particles remain inside the oil phase. They have time to find their minimum energy position as the hexane evaporate and formed clusters with Lennard-Jones geometries.

Intermediate cases are interesting. Both Span 20 and Tween 85 formed mixtures with nanoparticles that efficiently lower the interfacial tension. The resulting emulsions were less stable than that formed with SDS and Triton X-100, but more stable than the Pickering type. Emulsions that only contain alkylthiol-coated gold nanoparticles prove too instable to work with. When using Span 20 or Tween 85, the dropets obtained are stabilised by a composite layer of particles and surfactants. The clusters formed through evaporation of the solvent are composed of fcc or amorphous clusters.

Manoharan and Pine reported that microparticles adsorbed at oil-water interfaces collapse when the oil phase is evaporated. The spheres form supraparticles with predictable structures[29, 30]. We showed previously that nanoparticles arrange into predictable, but structurally different supraparticles when confined to the oil phase of a droplet stabilized by Triton X-100 (or SDS, as we showed here). Although Span 20 and Tween 85 form reasonably stable emulsions in which particles reside at the oil-water interface, the evaporation of the oil phase does not yield any of the structures observed by Manoharan et al. for larger particles. Instead, pieces of fcc crystals form.

Nanoparticles are more mobile than microparticles and dominated by interactions different from those governing microparticles. The smaller particles can find minimum free energy cluster configurations that have not been observed for the larger species. This may also explain why nanoparticles do not collapse like microparticles when confined at a liquid-liquid interface: where microparticles slowly move, nanoparticles are in constant motion and can fall into local minima of dense fcc packings.

Although these results give us a better understanding on the parameters involved in nanoparticles clustering, more efforts are still needed to reveal the interactions involved during the assembly and how they can be used to manipulate the superstructures built from primary nanoparticles. Many other parameters such as temperature, solvents, ligands and ageing may infuence the assembly processes.

Chapter 6

Ageing of gold nanoparticle and its effects on supraparticles

6.1 State of the art

Ligand molecules on the AuNP surfaces control the growth of the particles during synthesis and prevent particle aggregation. Typical ligands have functional groups that bind covalently to the gold surface. It is tempting to imagine such layers as a solid shell that protects the gold core and imparts it with solubility in liquids that interact with the ω-functionality of the ligand. In reality, even the comparatively strong bonds between thiol-bearing ligands and the nanoparticle surface undergo dynamic binding and unbinding processes [125–127].

This is not unique to AuNPs. Anecdotal evidence suggests that ageing occurs (depending on storage conditions) for many technically relevant systems: it is a common advise to use freshly synthesized particles for material synthesis or studies on colloidal stability. We are not aware of a systematic study on the storage stability of different nanoparticles. The following briefly summarizes publications on different particle types that at least mention observed ageing.

Dollefeld et al. explained the apparent shrinkage of thiol-capped cadmium chalcogenide nanoparticles detected by analytical ultracentrifugation and optical spectroscopy with ligand desorption [128]. They used NMR to show the constant dynamic replacement of ligand molecules and argued that losses can be expected in the absence of excess free ligand. Kalyuzhny and Murray reported ligand losses during the purification of

CdSe nanocrystals [129].

Aldana et al. identified photo-oxidation as an irreversible reaction that leads to desorption of stabilizing thiol ligands from CdSe nanocrystals in water [130]. Particle degradation occurred only in the absence of free thiols in the dispersion. The authors suggested that excess thiols allow the reconstruction of the ligand layer and retain stability and solubility of the nanocrystals.

The particle cores' surfaces underneath ligands may also oxidize. Cheng et al. combined TEM with magnetic measurements to characterize the stability of colloidal Co nanocrystals prepared in the presence of oleic acid (OA) and trioctylphosphine oxide (TOPO) during storage in air. They observed surface oxidation of the Co nanocrystals and inhomogeneous growth of FCC CoO on the surface of the Co nanocrystals, resulting in a drop in the magnetic moment and an increase in the hysteresis loop shift and coercivity [131].

Ligand layers are often imagined as uniform hollow spheres around perfectly spherical cores. On planar gold surfaces, many thiols form self-assembled monolayers (SAMs) with ordered and uniform geometries. On AuNPs, the ligand encounters not only different crystal facets, but also a multitude of edges, terraces and vertices, resulting in binding sites with different affinities for the ligand molecules [132, 133]. The resulting layer has a complex structure that depends on the exact core geometry. Ligand-solvent interactions vary over the particles' surfaces, which affects colloidal stability. Reorganization of the ligand layers can occur as a result of the dynamic equilibrium between free and surface-bound ligand molecules or involve practically irreversible chemical reactions, such as oxidation of ligands or surface sites. It can be a slow process that causes gradual changes in particle behavior.

Chechik and others studied reaction rates of place-exchange reactions between n-butanethiol-protected AuNP and disulfides using electron spin resonance [134, 135]. They observed that aged samples showed decreasing exchange rates and attributed the decrease in the number of defect sites as the original ligand slowly reorganized. The aged (and, therefore, reorganized) ligands on aged nanoparticles desorbed at higher temperature according to thermogravimetry. In their case, ageing improved the stability of the particles.

Ligand surface density is known to affect the properties of nanoparticles. For example, poly(ethylene glycol)s (PEGs) are widely used as as ligands for nanoparticles used in biology and medicine. Their density modulates nanoparticle properties [136]. At low PEG density, the units on a surface are organized in a so-called mushroom configuration, whereas at higher PEG density they display a brush configuration [137]. Only the brush configuration provides an optimal surface protection against opsonization. It is unclear whether and how the surface density of the PEG changes as such particles age under different conditions.

The assembly of colloidal nanocrystals into superstructures is sensitive to the molecular interactions between ligands bound to the NP surfaces. Interactions between the NPs, the ligands and the surrounding solvent has to be considered [52–54]. Recently, it was demonstrated how variations in ligand coverage bound to the NP surfaces can influence the interactions of NPs during assembly and the resulting structure [138]. PbS nanoparticles with dense ligand coverage assemble into superlattices with FCC structures, whereas PbS NPs with sparse ligand coverage assemble into superlattices with BCC structure. Many authors have suggested that loss of ligand occurs preferencialy on {100} facets and ligands on {111} facets or other NPs will be interdigitated or aligned with each other to connect NCs along specific crystallographic directions.

Here, we discuss the ageing of AuNPs with dodecanethiol ligands stored in unpolar solvent. We study changes in optical properties, colloidal stability, the resulting loss when using the particles after storage and the changes occuring when forming supraparticles. Particle handling was choreographed to mimic typically employed protocols (filtering, ultrasonication, etc.) and standardized for a systematic study. Storage at different temperatures, with different headspaces, and in the presence of different concentrations of excess ligand were compared.

6.2 Sample preparation

A batch of 40 mL of gold suspension was divided into 4 aliquot (samples (A),(B) (C) and (D) or samples (A),(B),(E) and (F) or 2 samples (A) and 2 samples (G)). For characterisation of the suspension at different storage conditions, samples (A),(B) (C) (E) (F) and (G) were originally suspended in hexane whereas sample (D) was originally suspended in toluene.

6.2.1 Storage conditions

After synthesis and resuspension in the desired solvent, the samples were stored under different conditions:

- Sample (A) was stored at 23 °C, wrapped in aluminium foil to exclude light.
- Sample (B) was stored at 7 °C in the fridge to exclude light.
- Sample (C) was aliquoted in 5 vials of 2 mL. All aliqoits were dried in vacuum at room temperature. The dried particles were stored at 23 °C, wrapped in aluminium foil to exclude light.
- Sample (D) was resuspended in toluene (a mediocre solvent for these particles. The particles were then precipitated by the addition of the same volume of ethanol, washed 5 times by centrifugation and subsequently resuspended in hexane. The sample was then stored at 7 °C in a refigerator.
- Sample (E) was stored at 23 °C and wrapped in aluminium foil to exclude light. A fraction of 0.0125 % per volume of dodecanthiol was added, the resulting dispersion was vortexed for 1 min, precipitated by the addition of the same volume of ethanol, washed by centrifugation, and finally resuspended in hexane.
- Sample (F) was treated exactly as sample (E), but with a fraction of 0.125 % per volume of dodecanethiol.
- Sample (G) was stored at 23 °C under argon atmosphere, wrapped in aluminium foil to exclude light.

A single particle batch was used for each storage condition to avoid batch-to-batch variations.

6.2.2 Preparation of gold suspension for characterisation

During storage, samples were drawn every week for analysis. To this end, each liquid storage vial was vortexed for 10 s, 0.5 mL were withdrawn from the middle of the storage bottle, and sonicated for 10 min at 150 W. Care was taken not to shake up sediment. One half of the sonicated solution was drawn from the storage bottle into a syringe through a PTFE syringe filter (0.45 μm pore size), transferred to an Eppendorf

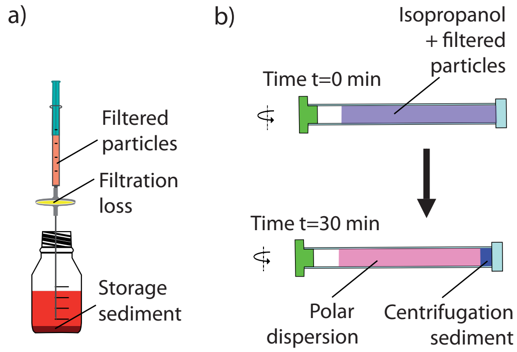

Figure 6.1: Sample preparation and testing of polarity - (a) Samples were drawn from the storage bottle into a syringe, a part of it through a syringe filter. Losses were quantified using mass balances. (b) Aliquots were mixed with polar solvent and their agglomeration and sedimentation was quantified in an analytical centrifuge.

vial (Figure 6.1), and used for analysis. The other half was left unfiltered and used for analysis.

At the same interval, dry aliquots of sample (C) were resuspended in 2 mL hexane and sonicated for 10 min at 150 W. All further handling was identical to liquid samples.

6.3 Results

The choice of storage conditions was based on a literature review. Most nanoparticle dispersions are stored at room temperature [128, 131, 139] or at lower temperature [140]. Sometimes, excess ligand is added to the suspension to ensure optimal surface coverage especially for ligand-exchange reaction [141, 142]. In some cases, the suspension is stored under Argon [140, 143].

Nanoparticle handling typically involves transfer, sonication, filtration and centrifugation steps. We performed these steps for each stored sample every week and used UV-Vis spectroscopy at the surface plasmon resonance (SPR) together with AAS to quantify losses that occurred during every step. The results provide a rough but useful indication of losses one can expect for different conditions.

More subtle are changes in the particle behaviour that do not directly lead to losses but affect functional aspects of the particles, for example when they are used as components in a composite material. We quantified such changes by analyzing the agglomeration state by DLS, the SPR position, and the agglomeration behavior in polar solvents using analytical centrifugation. Together (and comparing filtered and unfiltered samples) these methods are sensitive to a variety of changes in particle behavior.

6.3.1 Fractionation of particles due to ageing

Dispersions were stored for at least 21 days under different conditions and analyzed weekly. Samples were taken from the dispersions following a protocol designed to reflect typical colloid handling methods as applied in practice.

The size of the different dispersions were characterized using DLS and are presented for each storage condition at different storage time in figures 6.2 and 6.3.

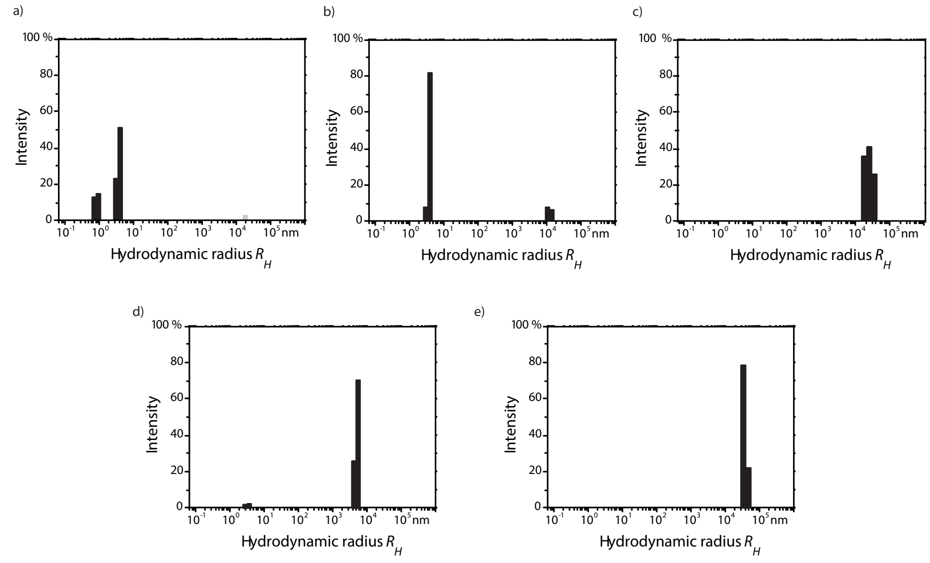

Figure 6.2: Hydrodynamic radius of sample (A) stored at 23 °C**, wrapped in aluminum foil** - The results are presented for different storage times : a) fresh particles, b) after 7 days, c) after 14 days d) after 21 days e) after 28 days. The formation of aggregates is observed after 14 days.

The size of the dispersions depended strongly on the storage conditions. Fresh particles show the same radius of monodisperse nanoparticles around 3.73 nm±0.28 nm for all storage conditions. However, after 14 days, the formation of aggregate is observed for all sample conditions. All stored samples were instable in the sense that the freshly filtered dispersion exhibited increasing particle sizes in DLS after less than one hour.

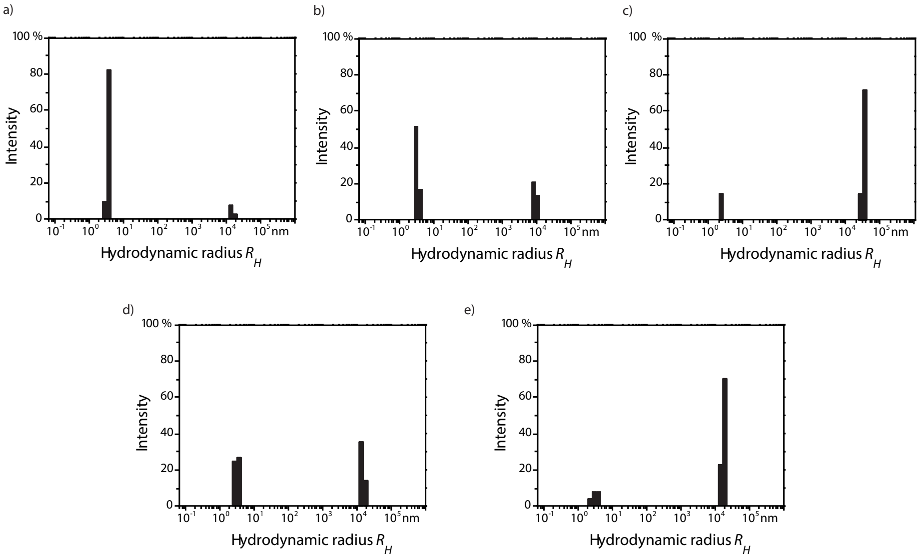

Figure 6.3: Hydrodynamic radius of sample (B) stored at 7 °C - The results are presented for different storage times : a) fresh particles, b) after 7 days, c) after 14 days d) after 21 days e) after 28 days. The formation of aggregates is observed after 14 days.

Precipitation experiments were performed using the analytical centrifugation. Typical sedimentation behavior patterns of the gold nanoparticle suspension with isopropanol are represented in figures 6.4 to 6.7 as a function of the position within the sample cuvette at a given sedimentation time. The position is given as distance from the centre of rotation. The position of the filling height is usually around 107 mm ± 2 mm. The cell bottom is at the radial position of 129 mm. The first recorded transmission profile is characterized by low transmission of approximately 20-30 % and increased during centrifugation. As particles settle, their concentration decreases in this region and transmission increases. Due to the polydisperse settling, the particle concentration gradually changes along the sample length. For all storage conditions, the particles-isopropanol mixture seems to become more and more stable.

An unexpected outcome of the measurement was the fractionation of particles. We consistently found — in ratios depending on storage conditions — that a fraction of particles agglomerated irreversibly and sedimented, a fraction remained suspended but formed smaller agglomerates, a fraction remained dispersed but changed its agglomeration behavior in polar solvents, and a fraction that appeared largely unchanged.

We analyzed the following fractions every week:

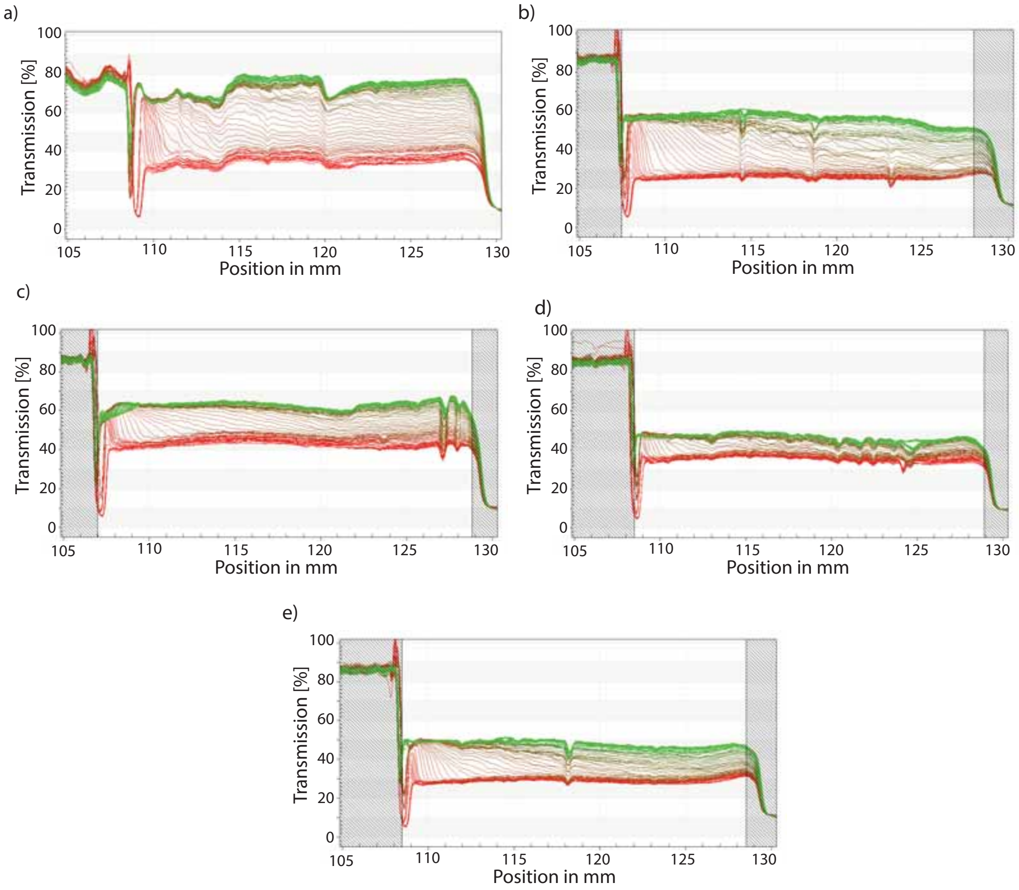

Figure 6.4: Comparison of transmission profiles of isopropanol/gold suspension mixture for sample (A) for different storage times - Results are displayed for a) fresh particles, b) after 7 days, c) after 14 days, d) after 21 days, and e) after 28 days. The centrifugation was performed at 20 °C, at accelerating velocity with interval between profiles of 10 s.

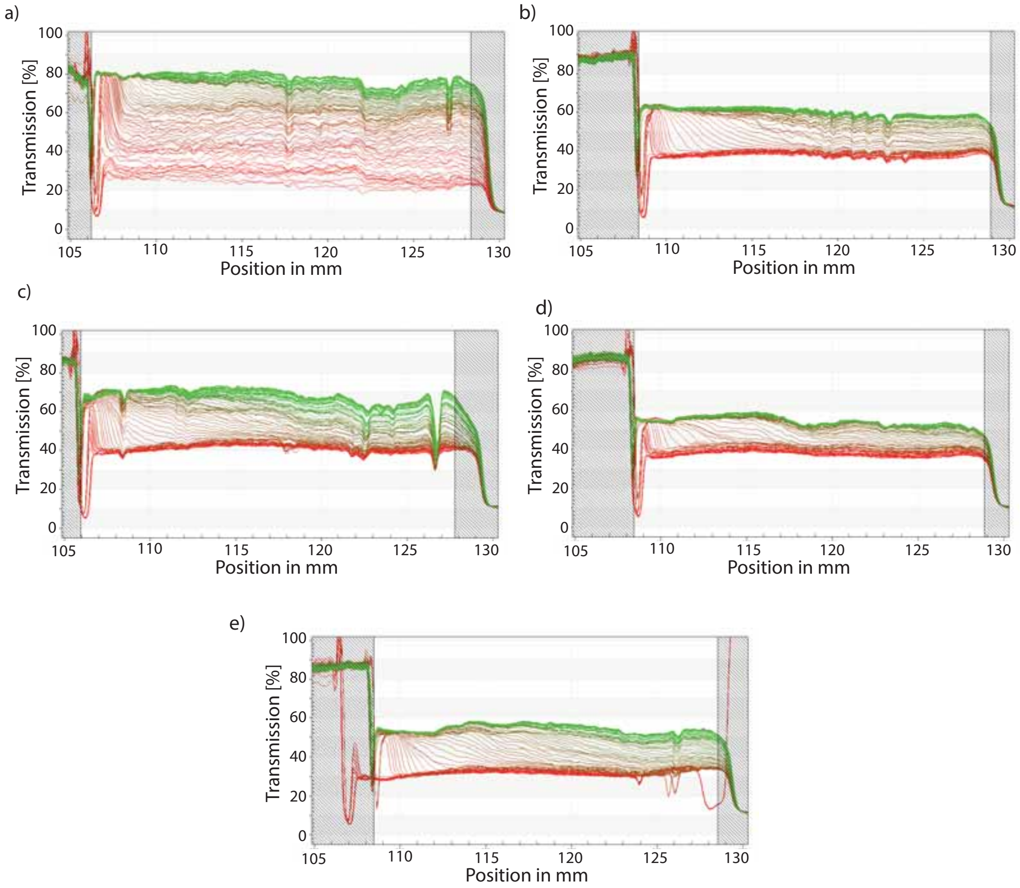

Figure 6.5: Comparison of transmission profiles of isopropanol/gold suspension mixture for sample (B) for different storage times - Results are displayed for fresh particles, b) after 7 days, c) after 14 days, d) after 21 days, and e) after 28 days. The centrifugation was performed at 20 °C, at accelerating velocity with interval between profiles of 10 s.

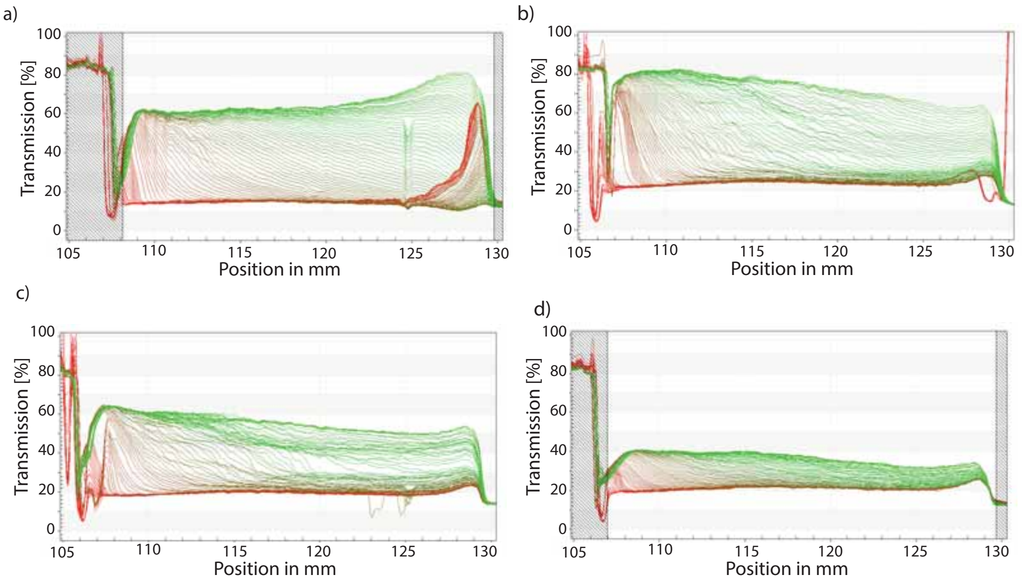

Figure 6.6: Comparison of transmission profiles of isopropanol/gold suspension mixture for sample (C) for different storage times - Results are displayed for a) fresh particles, b) after 7 days, c) after 14 days, and d) after 21 days. The centrifugation was performed at 20 °C, at accelerating velocity with interval between profiles of 10 s.

- particles agglomerating in the storage vessel that formed a sediment: **fraction 1**,
- particles agglomerating in the storage vessel that remained in the filter: **fraction 2**,
- particles dispersed in the storage vessel that remained dispersed upon adding propanol: **fraction 3**,
- particles dispersed in the storage vessel that precipitated upon adding propanol: **fraction 4**.

Fraction 4 dominates freshly prepared dispersions (typical range around 60 %). Upon ageing, the first three fractions gained in size for all storage conditions.

Optical spectroscopy was used to quantify the size of fraction 1, fraction 2 and the combined fractions 3 and 4 (the filtered sample). Particle concentrations were determined by UV-Vis spectroscopy to calculate the fraction lost through sedimentation and filtration. Dilution was necessary to operate in the optimal dynamic range of the

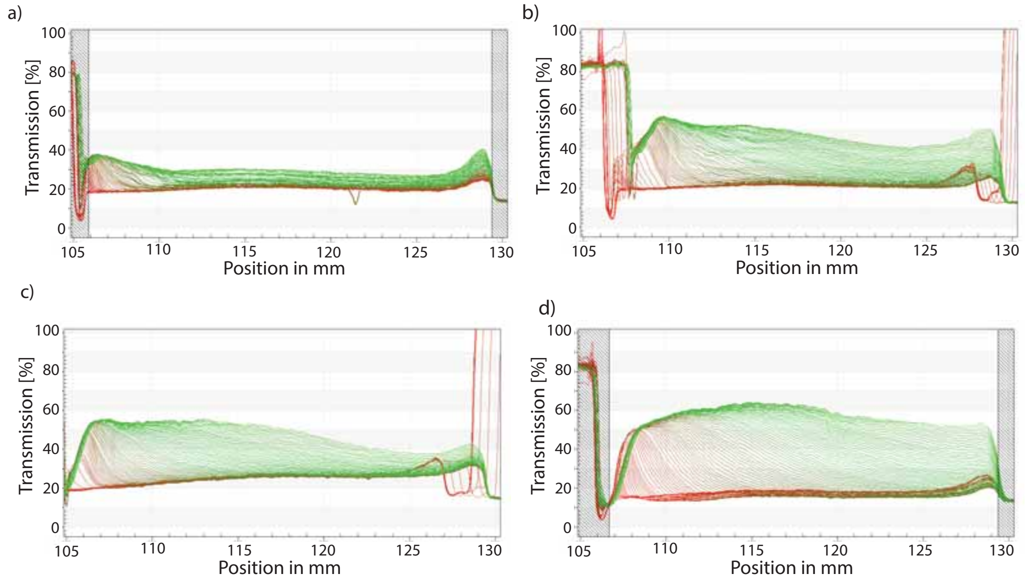

Figure 6.7: Comparison of transmission profiles of isopropanol/gold suspension mixture for sample (D) for different storage times - Results are displayed a) fresh particles, b) after 7 days, c) after 14 days, and d) after 21 days. The centrifugation was performed at 20 °C, at accelerating velocity with interval between profiles of 10 s.

instrument. For each sample, we chose a dilution ratio d_{uv} based on the maximum absorbance of fresh (non-aged) dispersions such that $A_{w1}(\lambda \approx 517\text{nm}) = 0.65 \pm 0.03$. This dilution was then used for all measurements on the sample while it aged.

We assumed the absorbance A to be directly proportional to the concentration c for each fraction at the peak wavelength λ_{max}:

$$A \quad = a \times l \times c \tag{6.1}$$

where a is the absorptivity (dependent on the fraction) and l is the path length of the absorbing medium (where only hexane was used for optical measurements).

Mass balances were used to calculate the fractions where necessary: for example, we measured concentrations of freshly prepared, aged but unfiltered dispersions and compared them to the concentration in the filtered dispersions to calculate the amount of particles lost in the filter (fraction 2). Fractions 3 and 4 were quantified using time-dependent optical spectrometry in an analytical centrifuge.

Many standard procedures in dispersion handling are difficult to perform without variation. Filtration results will depend on the exact agglomeration state and tend to remove dispersed particles when many agglomerates are caught in the filter. Representative sampling from a larger volume is hard when agglomerates are present. When using large volumes, mixing becomes hard. When using small volumes, rapid evaporation falsifies concentrations. Random errors on the order of 10% are expected. We report the results of multiple repetitions to give an impression of the variations.

Fractions 3 and 4 were quantified with an analytical centrifuge. The concentration of gold nanoparticles can have an influence on the precipitation experiment. In order to avoid concentration effects, we used the same concentration for all analytical centrifugation and we diluted the filtered dispersion using the dilution factor d :

$$d = d_{uv} \frac{A_f(t)}{A_f(t_0)} \tag{6.2}$$

where $A_f(t)$ is the maximal absorbance of filtered particles at time t and $A_f(t_0)$ is the maximal absorbance of filtered particles just after synthesis.

The analytical centrifugation is based on the Beer-Lambert law for concentration analysis. However, the Beer-Lambert-law is limited to diluted systems. At higher concentration multiple scattering occurs which results in a non-linear dependency between extinction and concentration. In order to avoid high concentration effects, the solution was diluted by an additional factor of ten:

$$\begin{aligned} d_{LUM} &= 0.1 \times d \\ d_{LUM} &= 0.1 \times d_{uv} \frac{A_f(t)}{A_f(t_0)} \end{aligned} \tag{6.3}$$

Filtered particles (with fractions 1 and 2 removed) were precipitated and the sedimentation of the particles observed by optical transmission.

The concentration of fraction i when considering the filtered particles is c_i, a part of the total filtered particle concentration c_0, and can be expressed as a mass fraction:

$$\phi_i = \frac{c_i}{c_0} \tag{6.4}$$

If the optical transmission is related to the concentration via Lambert-Beer's law,

$$-log(T) \quad = \quad a \times l \times c \tag{6.5}$$

the mass fraction of (filtered) particles stable upon addition of 1-propanol at the end of the separation process ($t = t_{end}$) equals

$$\begin{aligned}\phi_{stab} &= \frac{-log(T_{end}/T_{max})}{a \times l} \times \frac{a \times l}{-log(T_0/T_{max})} \\ &= \frac{log(T_{end}) - log(T_{max})}{log(T_0) - log(T_{max})}\end{aligned} \tag{6.6}$$

where T_{max} is the maximum (spatially uniform) transmission of a cuvette containing pure solvent mixture and T_0 is the initial transmission for the total filtered particle concentration at time t_0. T_{max} is approximately 80% in our experiment.

The mass fraction of (filtered) particles precipitating upon addition of 1-propanol at the end of the separation process ($t = t_{end}$) equals

$$\begin{aligned}\phi_{unstab} &= 1 - \frac{log(T_{end}) - log(T_{max})}{log(T_0) - log(T_{max})} \\ &= \frac{log(T_0) - log(T_{end})}{log(T_0) - log(T_{max})}\end{aligned} \tag{6.7}$$

The mass fraction of particles of the original dispersion (in the storage vessel) stable upon addition of 1-propanol ϕ_3 then equals

$$\phi_3 \quad = \quad \phi_{filtered} \times \phi_{stab} \tag{6.8}$$

Correspondingly, the mass fraction of particles of the original dispersion (in the storage vessel) precipitating upon addition of 1-propanol ϕ_4 equals

$$\phi_4 \quad = \quad \phi_{filtered} \times \phi_{unstab} \tag{6.9}$$

where $\phi_{filtered}$ is the mass fraction of particles that pass the filtration step.

Note that fractionation does not imply sharp transitions in particle properties. It is more likely that certain inherent particle properties change in a continuous fashion. Experiments like precipitation in a polar solvent create fractions containing particles from a range of values of this property (say, particle-solvent interaction). Kinetic effects will likely cause overlaps so that particles having identical properties may end up in different fractions. It is also important to note that in samples where fractions 1 or 2 are dominating, fractions 3 and 4 become small and their analysis is burdened by large statistical uncertainties. We do not report results for samples (C) and (D) due to these uncertainties.

Figure 6.8 shows the fractionation of samples stored under different conditions at different times. In the following, we discuss which mechanisms are consistent with the observed evolution.

Fraction 1 — losses due to sedimentation in the vessel — does not exceed 20% for the dispersions (A) and (B) stored in liquid without additional treatment. It is greater both for samples stored in dry (C) and washed additionally (D). Redispersion and washing apparently fostered sedimentation.

Fraction 2 — losses in filtration — remains approximately constant for wet storage and shrinks for both dry and washed storage. Particles seem to move from fraction 2 to 1.

Fraction 3 — dispersed particles stable upon addition of 1-propanol — grows in almost all cases when considering the total amount of particles that remain dispersed.

Fraction 4 — dispersed particles precipitating upon addition of 1-propanol — dominates originally and systematically shrinks, usually both overall and compared to fraction 3. Particles appear to leave this fraction when ageing.

6.3.2 Evolution of Surface Plasmon Resonance upon ageing

We can exclude fundamentally different mechanisms of ageing (e.g., Ostwald ripening and aggregation) by analyzing the surface plasmons resonance (SPR) of the dispersions.

Considering the SPR model derived by Mulvaney based on the Drude approximation [36]:

$$\lambda_{spr} = \lambda_p^2(\epsilon^{\mathrm{NP}} + 2\epsilon_m) \tag{6.10}$$

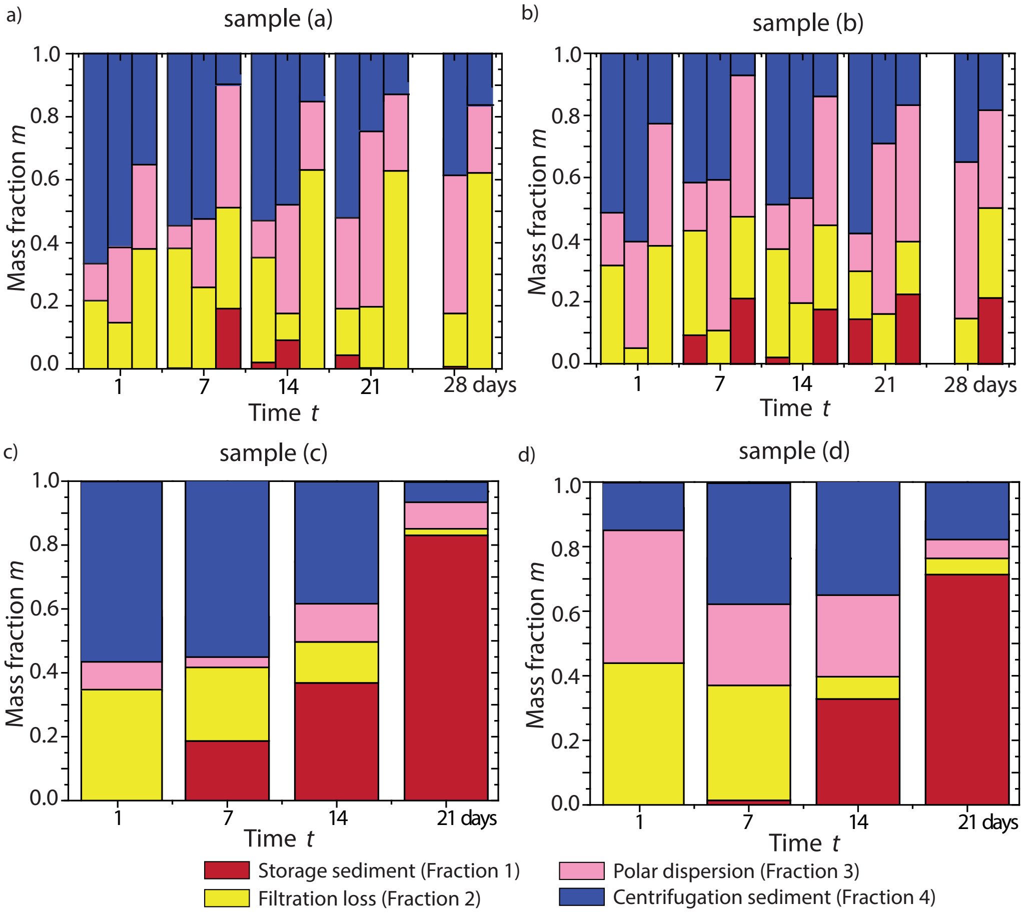

Figure 6.8: Mass fraction of sediment (fraction 1), particles lost through filtration (fraction 2), particles that remained dispersed upon adding propanol (fraction 3), particles that precipitated upon adding propanol (fraction 4) for the sample (A) sample (B), sample (C), sample (D) - For all storage conditions, fraction 4– particles dispersed in the storage vessel that precipitated upon adding propanol – decrease with time with the lowest ratio observed for sample (C). Sample (A) and (B) show almost the same behaviour whereas sample (C) and (D) exhibit an exponential increase of fraction 1 and low fraction 4 from the beginning. This suggests that dry storage and purification lead to sedimentation and changes in polarity probably cause by ligand loss.

where ϵ_m is the dielectric constant of the medium, ϵ^{NP} is the dielectric constant of the metallic nanoparticle, and λ_p is the bulk plasmon wavelength:

$$\lambda_p^2 = (2\pi c)^2 \times \frac{m_e \epsilon_0}{N e^2} \tag{6.11}$$

expressed in terms of the concentration of free electrons N in the metal, the effective mass of electrons m_e, the vacuum permittivity ϵ_0, and the velocity of light c. A blue shift of the SPR is expected upon a decrease in the medium's refractive index or a change in free electron density of the gold nanoparticles [144], while a red shift can be caused by aggregation of particles [31, 35, 46, 49, 145, 146].

As it was explained previously, results and experiment for samples (c) and (d) were not further studied since fractions 1 or 2 are dominating and the analysis of fractions 3 and 4 are burdened by large statistical uncertainties.

Figure 6.9 a) and b) show the shifts of the SPR from that of the freshly prepared and purified dispersion $\Delta\lambda$ to that of samples stored at RT (sample (A)) and at 7 °C (sample (B)) for different times. Blue shifts occurred under both storage conditions, but the shifts from sample B were too small to be statistically significant. The shifts were always greater for filtered than for unfiltered particles, but we did not observe red shifts even in cases where a large fraction of particles had agglomerated.

Figure 6.9 c) and d) show the gold content of the solvent after particles have been removed by precipitation with ethanol, centrifugation, and filtration. We found gold concentrations in the solvent that are easily detected by AAS. However, the standard deviations were too high to be statistically significant.

6.3.3 Effects of ageing in clusters formation

The self-assembly of particles can lead to clusters with complex structures. Here, we used routes previously described in *chapter 3* and *chapter 4* that exploit liquid droplets as confined templates within which nanoparticles are assembled. Gold nanoparticles were introduced into the disperse phase of an emulsion. The dispersed solvent was evaporated until the nanoparticles agglomerated inside the droplets. The superstructures formed were then characterized using TEM. In order to directly observe the influence

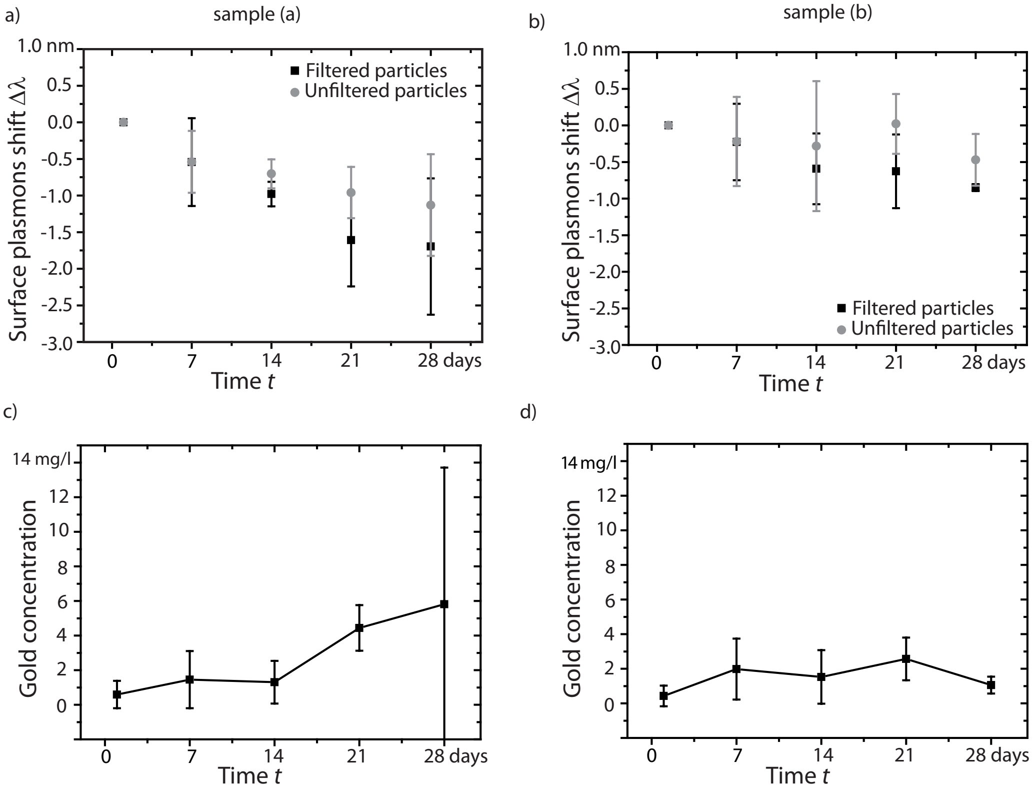

Figure 6.9: Observed blue-shift of the surface plasmon maximum and gold concentration in the supernatant solution - Shifts are displayed versus time for filtered (black) and unfiltered solution (grey) for the sample (A) and the sample (B). Gold concentration in the supernatant solution increases for sample A (c) but stays constant for sample B (d).

of ageing, the same batch was used and self-assembly of nanoparticles was realized and analyzed weekly.

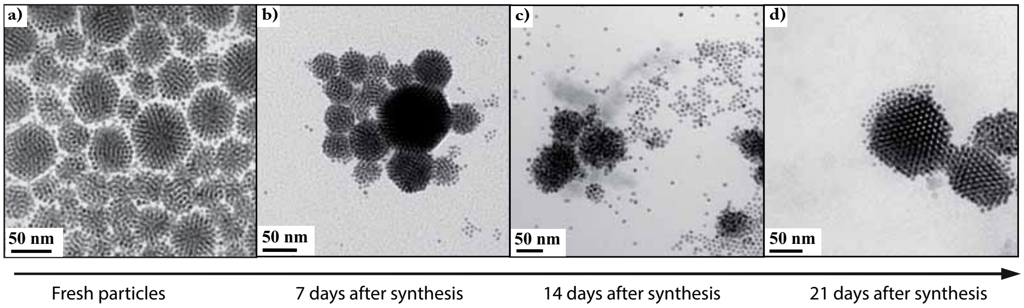

Figure 6.10: Electron micrograph series of agglomerates grown at different time for the same batch - Clusters with LJ geometries are formed when using fresh particles a) or particles which are only 7 days old. After 14 days, the crystallinity of the clusters change and interestingly clusters with FCC facets are observed after 21 days d).

Sample (A) was used for the formation of nanoparticles clusters. These agglomerates can be internally ordered (”supraparticles” or ”clusters” as described in *chapter 3*) or disordered. Figure 6.10 shows TEM images of agglomerates formed in emulsions containing gold nanoparticles at different time. TEM micrographs underline the markedly different morphology of the agglomerates formed using particles from the same batch. The morphologies of the supraparticles varied considerably within a batch. When using fresh particles, morphologies with LJ-geometries like icosahedral or decahedral clusters are observed. As the particles start to age, the morphologies change and different crystalline clusters and even amorphous clusters are observed ((figure 6.10) (c) and (d)). Figure 6.10 d) shows an FCC arrangement of nanoparticles inside the clusters. The transition from LJ-cluster to FCC-packing is observed when the gold dispersion was synthesized more than 14 days before cluster formation.

6.3.4 Effects of excess thiol

In order to improve stability of gold suspension, excess of thiol were added since it is usually added to ensure optimal surface coverage [141, 142]. To test this hypothesis, we added the equivalent to 4 mol% (sample (E)) and 40 mol% (sample (F)) of dodecanthiol to freshly prepared dispersions after washing. All other handling was unchanged.

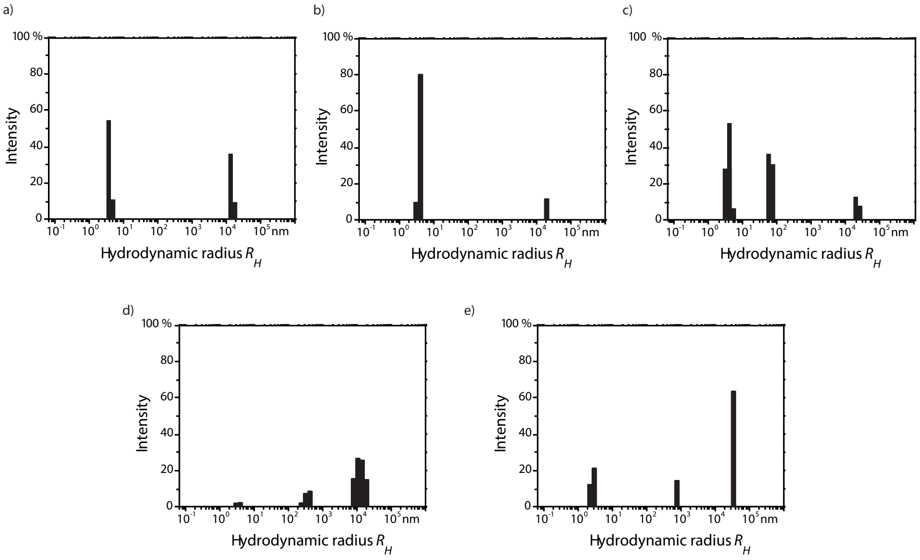

Figure 6.11: Hydrodynamic radius of sample (E) treated with (a) 4 mol% dodecanethiol after washing - The results are presented for different storage times : a) fresh particles, b) after 7 days, c) after 14 days, d) after 21 days, and e) after 28 days. The formation of aggregates is observed after 14 days.

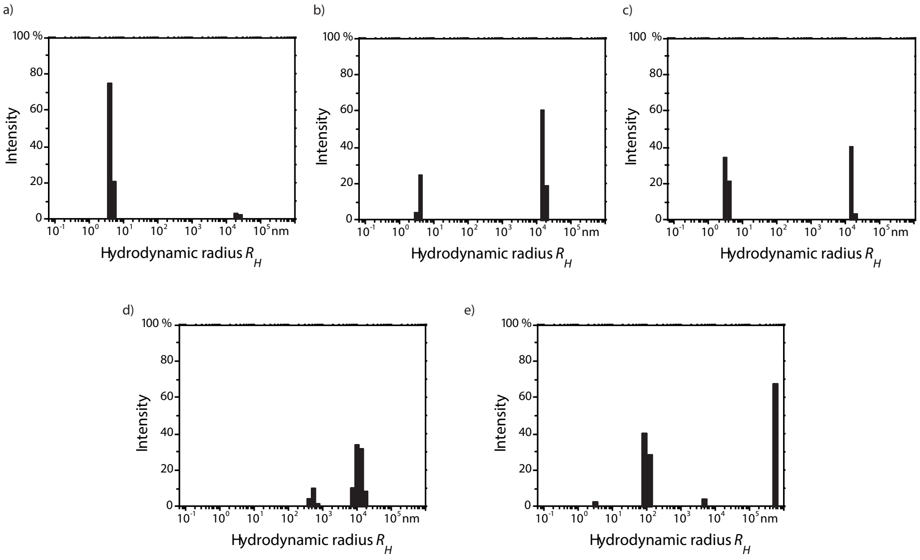

Figure 6.12: Hydrodynamic radius of sample (F) treated with (a) 40 mol% dodecanethiol after washing - The results are presented for different storage times : a) fresh particles, b) after 7 days, c) after 14 days, d) after 21 days, and e) after 28 days. The formation of aggregates is observed after 14 days.

The size of the two samples were analysed using DLS. After 14 days, the two samples were unstable and exhibit increasing particle sizes in DLS after less than one hour (see figure 6.11 and 6.12).

Figure 6.13 shows the evolution of the two samples during storage.

Fraction 1 — losses due to sedimentation in the vessel — does not exceed 20% for both samples and are comparable to the fraction observed for sample A and B.

Fraction 2 — losses in filtration — remains approximately constant.

Fraction 3 — dispersed particles stable upon addition of 1-propanol — are high for fresh particles for the dispersion containing the low amount of thiol and stays constant, whereas it seems to grow for the dispersion containing the high amount of thiol.

Fraction 4 — dispersed particles precipitating upon addition of 1-propanol — are low for fresh particles for the dispersion containing the low amount of thiol and stays constant, whereas it dominates originally the dispersion containing the high amount of thiol and shrinks, upon ageing. Particles appear to leave this fraction when ageing.

The blue shifts in the SPR are somewhat less pronounced than in the absence of thiol, and we did not observe any red shifts. Gold content in the supernatant liquid are higher than in the absence of thiol but no significant trend is observed during storage.

6.3.5 Effects of an inert head-space

We stored sample (G) under argon atmosphere at RT and studied it using above routines.

The size of the particles were analysed using DLS and also exhibit increasing particle sizes in DLS after 14 days. However, a small ratio of particles (around 20%) still remain dispersed in the dispersion and did not form aggregates even after 21 days (see Figure 6.14).

Figure 6.15 a) shows the evolution of the particles during storage.

Fraction 1 does not exceed 10%, fraction 2 increases but remains below 25 %, fraction 3 remains approximately constant and fraction 4 dominates originally the dispersion and shrinks upon ageing but not as fast as other storage conditions.

SPR analysis exhibits red shifts for unfiltered samples and a low blue-shit ($\approx$ 1 nm) for filtered samples. Gold content in the supernatant liquid are the lowest observed compared to other storage conditions.

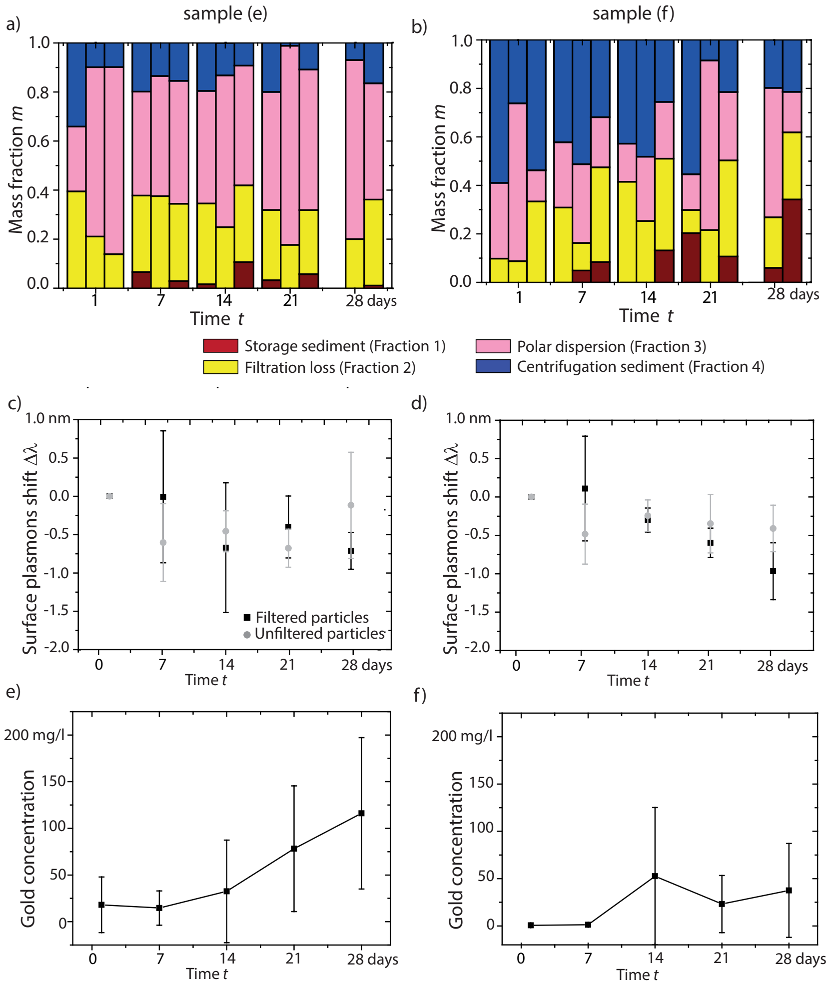

Figure 6.13: Mass fraction, shift in the SPR spectra and gold content in the supernatant liquid for the sample treated with (a) 4 mol% and (b) 40 mol% dodecanethiol after washing - A high amount of polar dispersion is present for the sample treated with 4 mol% dodecanethiol whereas sample treated with 40 mol% dodecanethiol shows almost the same behaviour as sample (A). c) and d) show the observed blue-shift of the surface plasmon maximum versus time from filtered (black) and unfiltered solution (grey) for the sample (E) and (F). Gold concentration (e) and (f) in the supernatant solution increase for both sample upon ageing with a higher increase for sample (E).

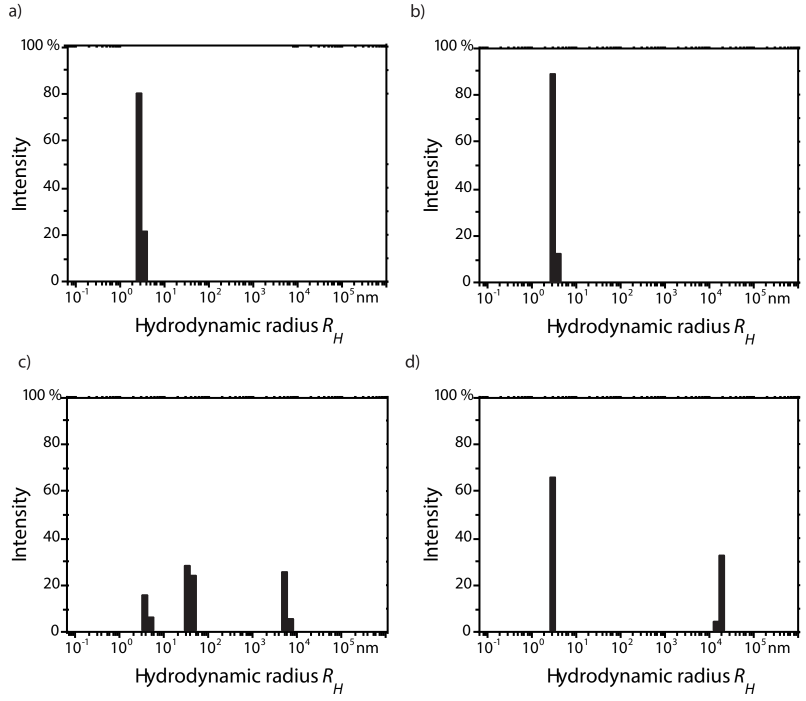

Figure 6.14: Hydrodynamic radius of sample (G) stored at 23 °C**, under Ar atmosphere, wrapped in aluminum foil** - The results are presented for different storage time : a) fresh particles, b) after 7 days, c) after 14 days, and d) after 21 days. The formation of aggregates is observed after 14 days.

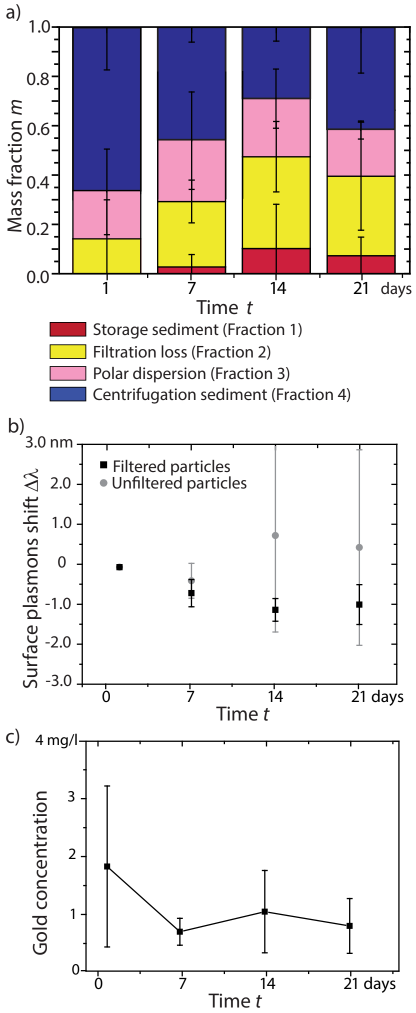

Figure 6.15: Mass fraction, Shift in the SPR spectra and gold content in the supernatant liquid for the sample stored under Argon atmosphere - The different fraction stays constant upon storage which implies that argon prevent oxidation a). Observed blue-shift of the surface plasmon maximum versus time from filtered(black) shows a low decrease with time b) whereas the peaks don't really shift for unfiltered solution (grey). Gold concentration (c) in the supernatant solution is low and stays constant upon storage.

6.4 Discussion

An unexpected outcome of the measurement was the fractionation of particles. Fractionation can result from imperfect mixing in the storage vessel, when different regions age differently. A fresh dispersion typically contains morphologically different particles with similar apparent size that form during synthesis. These particles may age differently and form the final fractions. Fractionation can also result from simple statistics. Nanoparticles carry comparatively small number of ligand molecules. If the probability for one ligand molecule to desorb during a given time is constant, a broadly distributed dispersion will form. Particles that have lost many ligands likely behave differently from particles that retained most ligands. The distribution splits into different fractions.

We suggest that fractions 1 and 2 form through agglomeration. Only agglomerates can sediment on our timescales: fully dispersed particles are Brownian. Filtration may also remove some fully dispersed particles, but only when considerable amounts of agglomerates block the filter. Agglomerate sizes control whether they sediment and enter fraction 1 or remain in the liquid and are filtered.

The existence of fractions 1 and 2 directly after synthesis suggests that agglomeration is ubiquitous. Even when using a well-developed, optimized synthetic protocol as we did, a certain fraction of particles is prone to agglomeration. Most published works use filtration or centrifugation before using particles to remove the unavoidable agglomerates [147–150]. We believe that nanoparticles from most syntheses involve at least some agglomeration even under optimal conditions. Agglomeration aggravated during storage. Samples stored under different conditions widely varied in the evolution of fractions 1 and 2 over time. Particles did not agglomerate at a constant rate; depending on storage conditions, agglomeration rates increased. We suggest that inherent properties of particles change during storage. This hypothesis is further supported by the evolution of fractions 3 and 4. A complex property of particles — their stability in a more polar solvent mixture — was probed to define these fractions. Only particles that did not agglomerate were tested. That the size of fraction 3 changes during storage can only be explained by a change in the particles' structure. That fraction 3 increases upon ageing is surprising.

Let us assume that ageing is caused mainly by a decreasing ligand density. Let us also assume that particles with dense ligand layers are stable against agglomeration in unpolar solvents but rapidly precipitate in more polar solvents. Particles with moderately dense layers slowly agglomerate in unpolar solvents, but remain stable in polar solvents for some time. Particles with sparse layers rapidly agglomerate in unpolar solvents.

All storage conditions lead to a decrease of centrifugation sediment and filtration losses (fractions 1 and 2). Above model explains this effect: in the original population, the majority of particles has a dense ligand layer. It takes a while until this part of the population has lost enough ligand to enter fractions 1 and 2. Before it does so, more and more particles go through a period with an intermediately dense ligand layer. They cause the increasingly large fraction 3 that is only finally diminished as the majority of particles becomes instable.

It is unclear why storage at room temperature (sample (A)) was preferable to fridge storage (sample (B)). Possible explanation include the condensation of water into the solvent (with water increasing the desorption reaction) [151] and temperature-induced agglomeration of particles due to reduced solubility [52], an effect that could be exacerbated by reduced ligand density.

Drying and redispersion (sample (C)) and extensive washing (sample (D)) both caused immediate ligand loss. Many particles enter fractions 1-3 before the storage period starts. Further ageing proceeds as expected: intermediately dense ligand layers become sparse, particles are lost in fractions 1 and 2. The amount of particles towards the end of the experiment is so small that statistical fluctuations dominate.

Drying and redispersion (sample (C)) also markedly increased fraction 2, indicating that dry particles could not be redispersed at all. We do now know whether this is due to ligand losses that make them insoluble or due to other morphological changes of the particles in dry state. The results clearly show that at least simple drying is not a viable option for particle storage. Careful lyophilizing may be less lossy.

The desorption of ligands can explain the fractionation that we observe. We cannot exclude similar, more complicated effects. However, ligand double layers may be present on some particles for example. (We did analyze all TEM micrographs of particles for increased spacing expected for such double layers and did not find any, but they may be lost in TEM preparation.) We cannot decide whether the change in particle behavior is thermodynamic and would occur regardless of the experimental time scales or whether agglomeration merely becomes more rapid (or less rapid, in the case of polar solvents) for aged particles.

Analysis of UV-Vis spectra for the different conditions present shift of the SPR peak. A blue shift of the SPR is expected upon a decrease in the medium's refractive index or a change in free electron density of the gold nanoparticles [144]. The former is likely to occur when ligands dissociate. For example, Jain et al. reported a gradual blue-shift in the SPR of gold nanoparticles from 525 to 519 nm when irradiating gold nanoparticles carrying thiolated DNA and attributed the shift to the dissociation of the ligand [152].

A red shift in the SPR can be caused by nearby particles that affect the medium's refractive index. In close proximity, surface plasmons of multiple particles are coupled, and Mulvaney's approximation eventually breaks down [31, 35, 46, 49, 145, 146].

If both agglomeration and ligand desorption occur in storage, one would expect shifts in both directions depending on the storage time, and broadening of the SPR from the superposition of both effects in different fractions.

The observed shifts can only be explained by a change in the refractive index of the particles' dielectric environment. It is hard to imagine any origin other than the desorption of ligand molecules. Our analysis of the spectra is simple and will not separate the SPR spectra of agglomerated and dispersed particles. But it is robust and would detect red shifts caused by agglomeration. The fact that all shifts are towards the blue strongly suggests that ligand desorption is strong and ubiquitous.

Gold concentrations in the solvent were easily detected by AAS. Usually such concentrations would cause a visible coloration if it was due to residual gold particles. Since there was no SPR signature detectable even in the samples with the highest gold content, we conclude that ligand desorption also entails gold desorption. It is unclear in which form gold is removed from the particles; thiolates or very small clusters are possible candidates. For example, Schmid found that even metal clusters made of $Au_{55}(PPh_3)_{12}Cl_6$ show features in the 520 nm plasma resonance band [153].

The assembly of colloidal nanocrystals into superstructures is sensitive to the molecular interactions between ligands bound to the NP surfaces. The assembly of gold nanoparticles inside emulsions droplets lead to supraparticles with different crystalline structure going from LJ geometries for fresh particles to FCC symmetries or amorphous structures for NPs stored at RT for 21 days. Similar structural changes were previously observed for the assembly of PbS NPs suspended in hexane via drop-casting [138]. NCs without air exposure assembled into FCC superlattices whereas NCs exposed to ambient air for only 2 days assembled into superlattice with BCT structures and NCs exposed to ambient air for 6 days assembled into superlattice with BCC structures. Some authors have suggested that ligand loss occurs preferentially on {100} facets of the NPs which lead to arrangements of NPs along specific crystallographic directions. We suggest that changes in structures of the clusters formed inside emulsion droplets is due to loss of ligand from NPs surface. Ligand desorption (observed via SPR blue-shift) leads to the formation of aggregates as it was detected by DLS. Those results suggest that aggregates are present before assembly of NPs and that they have amorphous or FCC structures. The structures remain during assembly inside droplets leading to the clusters observed in TEM.

If ligand desorption during washing hastens ageing, addition of excess thiol should be beneficial. However, thiol addition after washing seems to revert some of the degradation, but not all. The reduced loss in storage sediment, in particular for the smaller thiol addition, supports the idea that washing leads to an immediate loss of ligand that decreases particle stability from the first day. The large fraction of more polar particles may be explained by the thiol acting as a surfactant molecule that forms double layers around the nanoparticles, but it is unclear why a larger thiol concentration should reduce the polar fraction and not sedimentation. The blue shifts in the SPR are somewhat less pronounce than in the absence of thiol, and we did not observe any red shifts.

Some authors suggest oxidation as a mechanism leading to ligand loss. For example, films of gold nanoparticles (4 nm diameter) interlinked with 1,9-nanonedithiol and 1,16-hexadecanedithiol were oxidized when stored under ambient condition but remained stable under argon [154]. Aldana et al. have also demonstrated that photo-oxidation leads to desorption of thiol ligands at the surface of CdSe nanocrystals [130]. The inert atmosphere affected ageing notably. Sedimentation was reduced from the onset and the fraction of polar particles remained small. Samples stored under argon was the only case where we observed red shifts in the SPR spectra, indicating reduced ligand desorption. (The fact that red shifts were only observed in unfiltered samples is consistent with agglomeration shifting the SPR towards red). The magnitude of these changes is surprising, because we did not exclude air or water during synthesis or purification and expect both to be dissolved in the dispersion at the beginning of the storage period.

6.5 Summary

Alkylthiol-stabilized gold nanoparticles age under commonly used storage conditions. After 2 weeks, more than half the particles had changed their behavior when storing them in air at room temperature. Particularly problematic is the separation of the homogeneous dispersion into a mixture of fractions with different solubility. Experiments that are affected by particle-solvent interactions will produce subtly misleading results when performed on particles having widely different properties.

The results suggest that ligand loss is a major process responsible for sedimentation and changes in polarity upon purification and ageing. Ligand loss was not effectively prevented by storage at 7 °C or as dry particles. It was exacerbated by washing and could not be reverted by adding excess ligand. Only storage in inert argon did reduce ageing.

From a surface chemical standpoint, it appears that reactions involving thiol, gold, oxygen and possibly water and solvent take place during ageing. The exact mechanisms are unknown; it is unclear in which form the ligands (and gold atoms) leave the particles' surface or whether the gold surface with its catalytic properties enhances the desorption reactions. From a colloidal standpoint, it is interesting that details of the ligand chemistry so severely affect stability and behavior of the entire dispersion. The small number of ligand molecules on nanoparticles compared to classical colloids seems to make them more sensitive to the loss of some of them. Small changes in the particle-ligand structure strongly affect the particles' stability in different solvents.

The self-assembly of NPs into ordered supraparticles presents a route to novel functional materials where the assembly is controlled by the ligand-mediated interaction between neighboring NPs. Different ligand coverages on NPs surface has led to changes in the structure of the supraparticles. The resulting geometries depend on the degree of ageing in solution, due to desorption ligands on the particle surface, an effect that was previously demonstrated for the assembly of PbS into superlattices [138].

The sensitivity of particle behaviour on the exact ligand layer structure implies a need for more advanced ligand chemistry. It should be possible to exactly define the structure of this layer — for example, by cross-linking ligand molecules or their mixtures on the surface — and to design solubility, agglomeration behavior, and other important properties. Such ligand layers would be more stable, more reliable and could be better tailored to the application at hand.

Chapter 7

Conclusions and Outlook

This chapter presents a summary of contributions that have been accomplished in this thesis and a note on the future direction of research in this field.

7.1 Conclusions

In the past few years, scientist have dedicated their research to the formation of superstructures made from individual inorganic nanoparticles, which exhibit collective properties and promising applications [8–12, 74]. Among all types of superstructures, supraparticles are interesting because of their distinctive structural features which differ from dense two- or three-dimensional (2D or 3D) assemblies of nanoparticles. In contrast to other 2D or 3D assemblies on solid substrates, supraparticles can have uniform sizes and can be dispersed in solution [24, 30, 94, 155]. Due to their unique magnetic or optical properties, supraparticles have already been shown to exhibit some promising applications in the fields of solar cells [156, 157] and sensors [158].

This thesis has introduced supraparticles made of gold nanoparticles using emulsion droplet as template, with the goal of contributing to the development of an easy process for the production of supraparticles with interesting optical properties.

In the droplets, defined numbers of particles interact in a confined volume until a minimum-energy situation was reached, which leads to the formation of regular, anisotropic supraparticles. It was demonstrated that when monodispersed, sterically stabilized gold nanocrystals with diameters below 10 nm were introduced into the disperse phase of an oil-in-water emulsion, they form cluster-like structures upon removal of the dispersed solvent from the emulsion droplets. In emulsion, particles often segregate to the oil-water interface and form Pickering emulsions. Here, surfactants (such as Triton X-100 and SDS) were used in order to tune the surface energy of the droplets. Other surfactants such as Span 20 and Tween 85 are not sufficiently effective to stabilize the droplet and a mixture of surfactant and nanoparticles form spontaneously to efficiently lower the interfacial tension. Good surfactants such as Triton X-100 and SDS blocked the interface so that the particles remained inside the bulk of the droplets. The resulting emulsions were less stable than that formed with SDS and Triton X-100 and led to the formation of structurally different supraparticles. Interestingly, when using good surfactants, the particles did not arrange into small pieces of dense packings, but resembled clusters predicted for Lennard-Jones interaction potentials. In-situ observation of the assembly process via surface plasmon spectroscopy and small-angle x-ray scattering suggests that assembly occurs rapidly, shortly before the dispersed phase is entirely evaporated. This is in contrast to nucleation-and-growth mechanisms commonly observed in nanoparticle agglomeration and suggests that the ordered configuration observed here represents a minimum in free energy.

Different aspects regarding NPs need to be considered for the formation of superstructures from self-assembled NPs especially interactions between the NPs, the surface-bound ligands and the surrounding solvent and their evolution with time. Ageing of nanoparticles is a factor that has to be taken into account because it can influence the structure of the supraparticles formed. Supraparticles realized using a suspension at different storage time exhibit different structures.

Alkylthiol-stabilized gold nanoparticles aged under commonly used storage conditions. Especially, more than half the particles had changed their behaviour after only 14 days of exposure to air at room temperature. Particularly problematic is the separation of the homogeneous dispersion into a mixture of fractions with different solubility. Experiments that are affected by particle-solvent interactions will produce subtly misleading results when performed on particles having widely different properties. The results suggest that ligand loss is a major process responsible for fractionation and changes in polarity upon purification and aging. Ligand loss was not effectively prevented by storage at 7 °C or as dry particles. It was exacerbated by washing and could not be reverted by adding excess ligand. Only storage in inert argon did reduce ageing.

This resulting difference in structure during assembly proves that ageing of gold suspension has an impact on the formation of ordered supraparticles. Ligand coverage on the NP surface is an important parameter for NP superlattices assembly. The need to control the ligand density at NP surfaces calls for a broad theoretical understanding and computational study of the complex NP-ligand system which is still not fully developed and understood.

7.2 Outlook

We have seen here that emulsion stability plays a major role in the final structure of the supraparticles. The choice of the surfactant is a key parameter for the stabilisation of the droplets and prevent the migration of nanoparticles at the interface. The use of two different kinds of surfactants, a water-soluble and an oil-soluble surfactant would improve the stability of the droplet. PMMA supraparticles were formed by encapsulating the polymer colloidal microparticles in emulsion droplets of hexane and by subsequent removal of the hexane from the droplets [85]. An important feature of the method described here is the use of two different kinds of surfactants: standard water-soluble surfactants, and oil-soluble species which prevent microparticles to collect at the droplet interface. Without the introduction of the second surfactant, the microparticles segregate at the interface of the droplet. Using this new configuration, the particles could move freely throughout the droplet and might form dense, ordered supraparticles upon consolidation. The formation of a thick interfacial layer might improve stability and prevent coalescence of the droplets.

The emulsification methods used in this thesis involve stresses generated by manual or mechanical agitation. However, such stresses are not uniform across the system, nor are they precisely controlled. Emulsions formed in these ways thus consist of drops that are highly polydispersed in size. This effect leads to polydispersed supraparticles as shown on figure 4.2. Emulsification methods like membrane extrusion [159, 160], microchannel emulsification [161–163], and microfluidic devices[79, 164–167] have been developed and optimized to gain better control over the size and polydispersity of the drops. Using these techniques can be useful for the formation of monodispersed supraparticles since the size of the droplet is controlled by the size of the pore membrane or capillary.

Four surfactants were used in this study to investigate their effect on the emulsion stability. In order to extend the conclusions made regarding the emulsion structure, it would be interesting to work with more surfactants, covering a wider HLB values scale.

A further step towards functional materials will be the formation of binary superstructures from emulsion-based self-assembly. The synthesis of binary nanoparticle superlattices on a surface has previously been reported [168]. In future work, binary nanoparticle superstructures could be synthesized through self-assembly of two different nanoparticle components (gold plus silver for example) in one droplet and the collective properties of such mixtures could be investigated. Binary particle mixtures can lead to different structures depending on the particle-particle interactions and the properties of the liquid-liquid interface. It would be interesting to find when/if nanoparticles will mix randomly, as in a disordered mixed phase, or form binary crystals with interface-related deviations from bulk structure like metal alloys, or phase-separate like Janus particles. All of the resulting structures may be technologically interesting and it would be interesting to predict and decide which type of agglomeration can occur.

It would also be interesting to determine whether the mixture of particles of different diameters would provide interesting supraparticles structures. Supraparticles from a mixed suspension of 540 nm-latex microspheres and 22 nm-gold nanoparticles were formed from evaporation-assembly inside a droplet [78]. During the evaporation process, gold nanoparticles are small enough to pass through the interstices of the latex particles and segregate at the surface of the droplet. The resulting supraparticles exhibit a red color. It would be interesting to find out if the emulsion droplet containing a mixture of particles of different size would lead to the same structure as the one described by Rastogi [78] or if the surfactant would prevent the segregation of the smaller particles at the interface of the droplet.

Combining particles with varying ligand lengths could be a versatile approach to design new structures. Agglomeration kinetics of gold nanoparticles coated by alkylthiol were studied for different ligand lengths. Various authors have observed that agglomeration kinetics, and the morphology of the formed agglomerates are dominated by ligand-ligand interactions and ligand-solvent interaction [52].

Finally, the potential applications of supraparticles should also be developed in more detail. At present, the reported applications are mainly based on the properties of individual supraparticles. It is highly desirable to see possible applications of ordered and hierarchical assemblies, in which the inorganic supraparticles are used as building blocks for the formation of assemblies. Such assemblies could provide a much larger domain for the manipulation of their functionality compared to conventional assemblies simply composed of individual nanoparticles.

Appendix A

Projections of Lennard-Jones clusters

To create two-dimensional projections of the three-dimensional predicted Lennard-Jones cluster structures, the coordinate data obtained from the Cambridge Cluster Database and other sources [97, 98] was read into a MatLab-Program. This program first searches a convex hull containing all particles and then proceeds to find intersecting planes that contain as many particles as possible, in effect finding the facets of the clusters. The positions of all particles in the cluster are then projected normally to each of these facets and onto the facet. For each projected point on the facet plane, a circle with a certain greyscale value is drawn. When circles overlap, their greyscale values are multiplied and a darker region is formed. The resulting projections were compiled into catalogs for each cluster (including all clusters with 10 to 1000 particles and some larger ones). Shown below (Figures A1 to A10) are the catalogs for those clusters depicted in Figure 4.7.

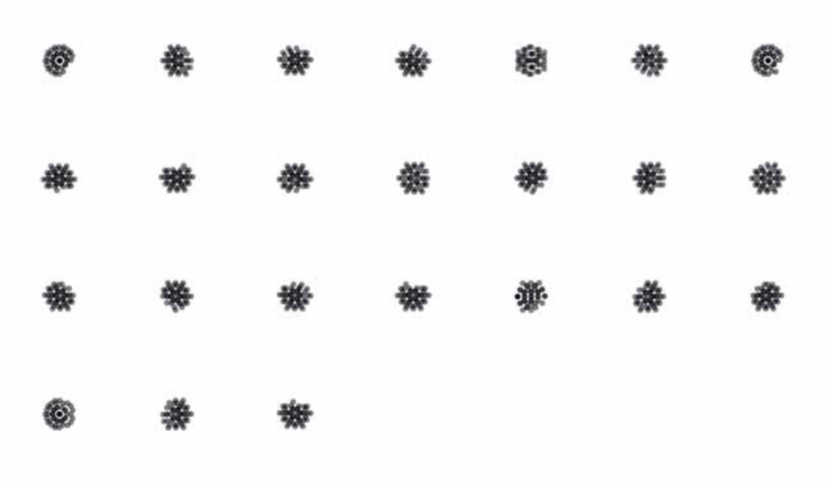

Figure A.1: Lennard-Jones cluster 47 - Catalog of projections of a Lennard-Jones cluster containing 47 particles onto each of its facets.

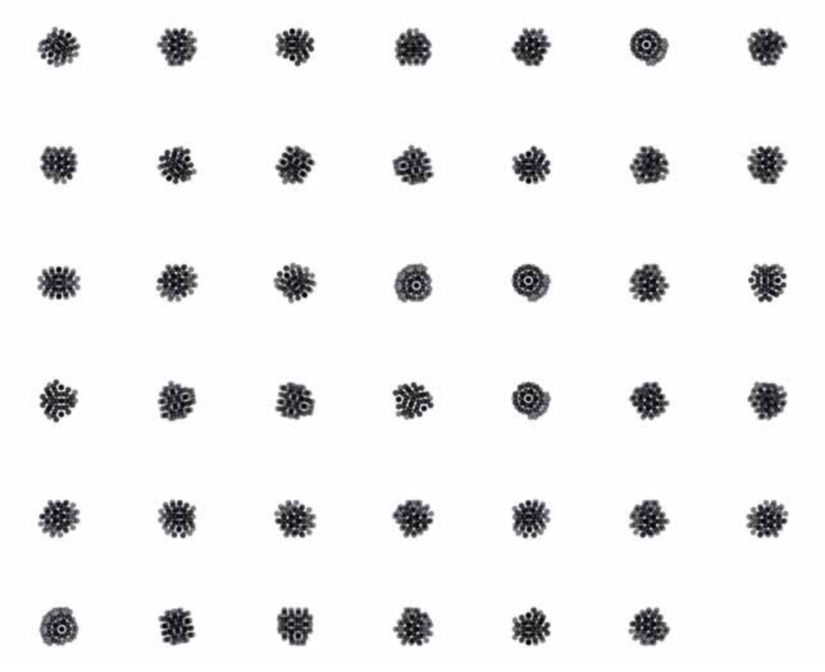

Figure A.2: Lennard-Jones cluster 78 - Catalog of projections of a Lennard-Jones cluster containing 78 particles onto each of its facets.

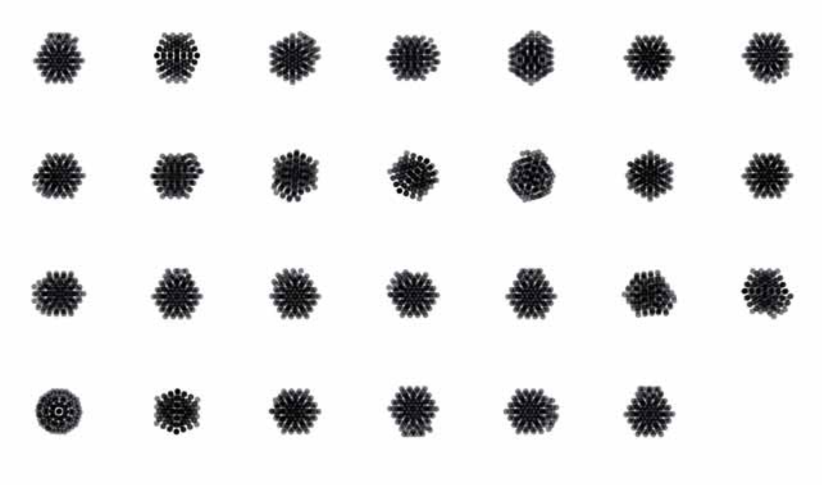

Figure A.3: Lennard-Jones cluster 160 - Catalog of projections of a Lennard-Jones cluster containing 160 particles onto each of its facets.

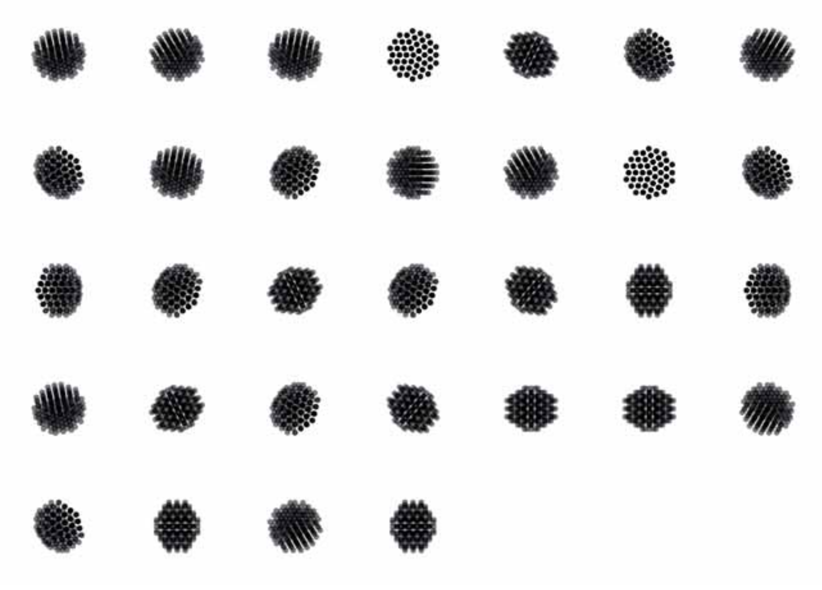

Figure A.4: Lennard-Jones cluster 190 - Catalog of projections of a Lennard-Jones cluster containing 190 particles onto each of its facets.

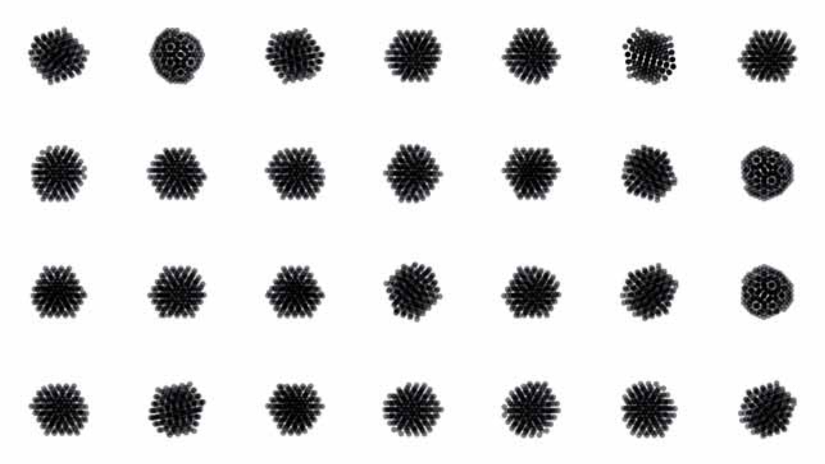

Figure A.5: Lennard-Jones cluster 228 - Catalog of projections of a Lennard-Jones cluster containing 228 particles onto each of its facets.

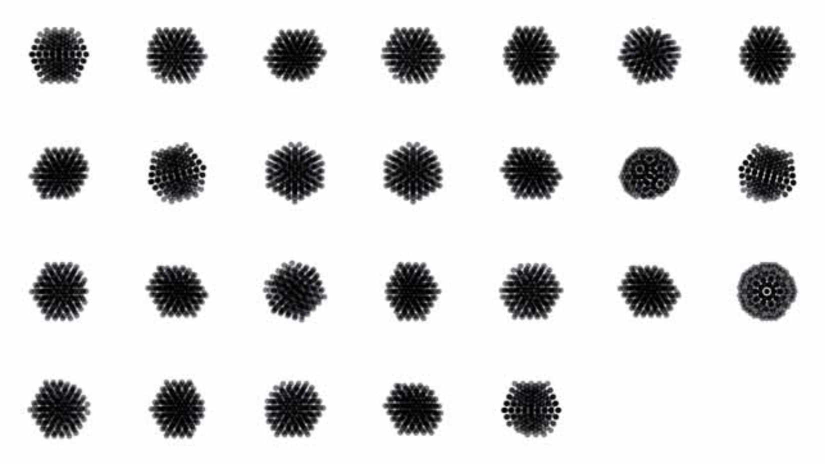

Figure A.6: Lennard-Jones cluster 255 - Catalog of projections of a Lennard-Jones cluster containing 255 particles onto each of its facets.

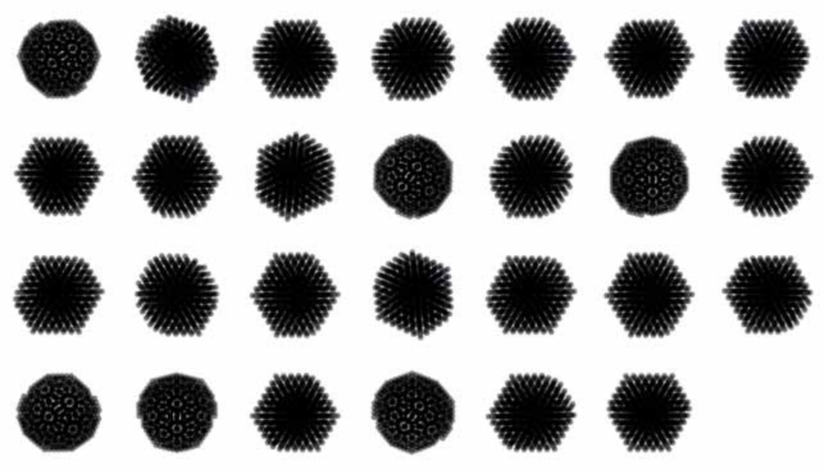

Figure A.7: Lennard-Jones cluster 750 - Catalog of projections of a Lennard-Jones cluster containing 750 particles onto each of its facets.

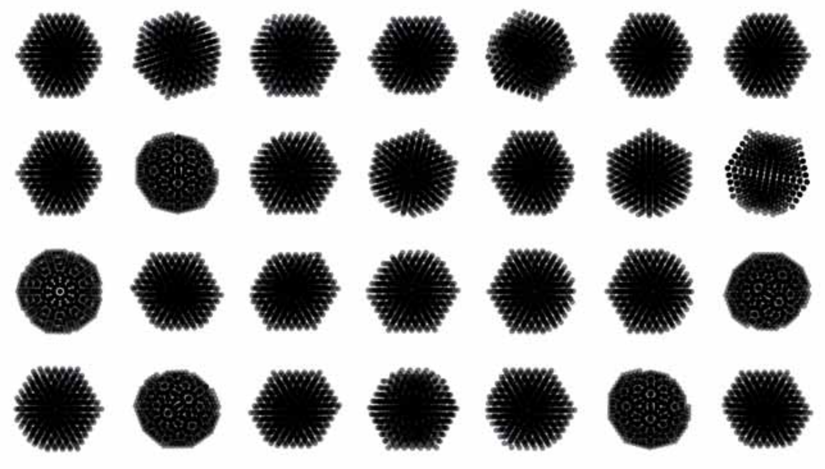

Figure A.8: Lennard-Jones cluster 807 - Catalog of projections of a Lennard-Jones cluster containing 807 particles onto each of its facets.

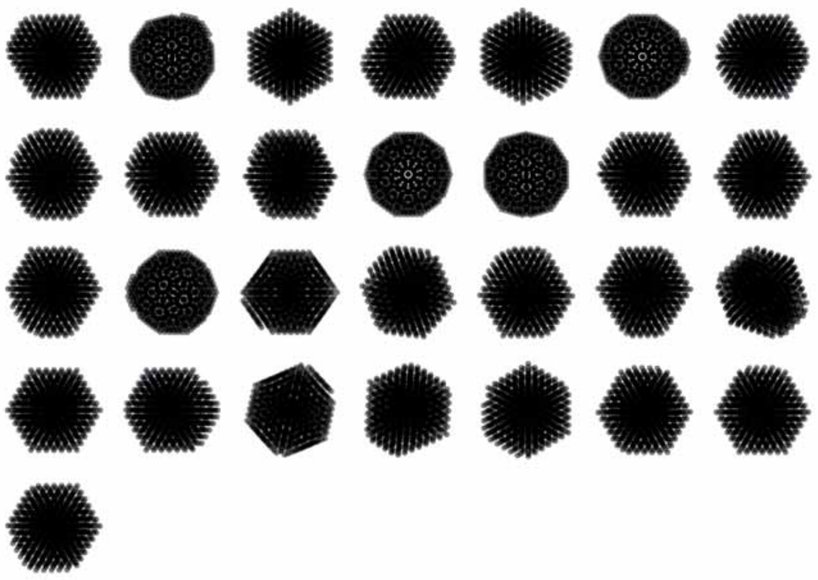

Figure A.9: Lennard-Jones cluster 971 - Catalog of projections of a Lennard-Jones cluster containing 971 particles onto each of its facets.

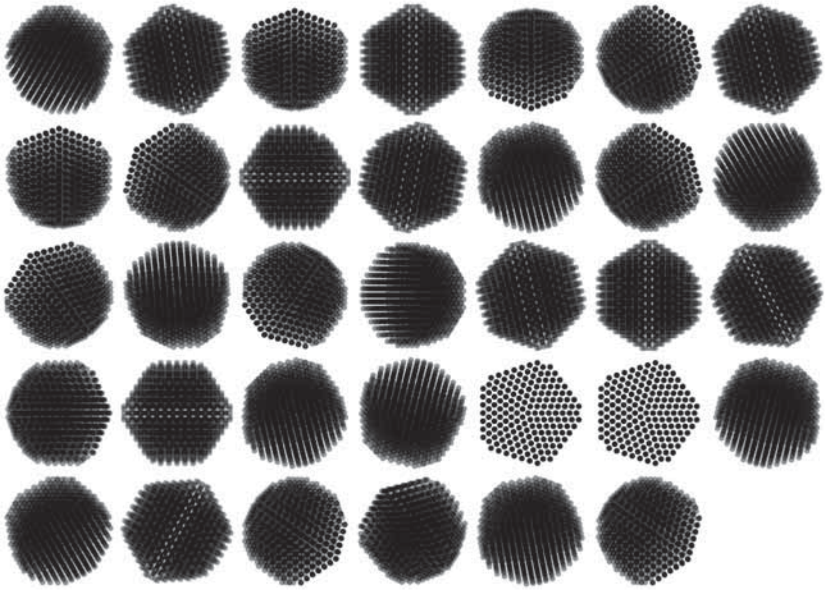

Figure A.10: Lennard-Jones cluster 1609 - Catalog of projections of a Lennard-Jones cluster containing 1609 particles onto each of its facets.

Bibliography

[1] P. Alivisatos. The use of nanocrystals in biological detection. *Nature Biotechnology*, 22:47 – 52, 2004. 1

[2] M. Haruta. Gold as a novel catalyst in the 21st century: Preparation, working mechanism and applications. *Gold Bulletin*, 37(1-2):27–36, 2004.

[3] R. A. Sperling, P. Rivera Gil, F. Zhang, M. Zanella, and W. J. Parak. Biological applications of gold nanoparticles. *Chem. Soc. Rev.*, 37:1896–1908, 2008.

[4] E. Boisselier and D. Astruc. Gold nanoparticles in nanomedicine: preparations, imaging, diagnostics, therapies and toxicity. *Chem. Soc. Rev.*, 38:1759–1782, 2009. 1

[5] F. Westerlund and T. Bjornholm. Directed assembly of gold nanoparticles. *Current Opinion in Colloid and Interface Science*, 14(2):126 – 134, 2009. 1

[6] M. Grzelczak, J. Vermant, E. M. Furst, and Luis M. Liz-Marzǹ. Directed self-assembly of nanoparticles. *ACS Nano*, 4(7):3591–3605, 2010.

[7] J. M. Romo-Herrera, R. A. Alvarez-Puebla, and L. M. Liz-Marzan. Controlled assembly of plasmonic colloidal nanoparticle clusters. *Nanoscale*, 3:1304–1315, 2011. 1

[8] J. Zhuang, H. Wu, Y. Yang, and Y.C. Cao. Controlling colloidal superparticle growth through solvophobic interactions. *Angewandte Chemie International Edition*, 47(12):2208–2212, 2008. cited By (since 1996)68. 1, 105

[9] J. Lee, . O. Govorov, and N. A. Kotov. Nanoparticle assemblies with molecular springs: A nanoscale thermometer. *Angewandte Chemie International Edition*, 44(45):7439–7442, 2005. 1

[10] R. Elghanian, J. J. Storhoff, R. C. Mucic, R. L. Letsinger, and C. A. Mirkin. Selective colorimetric detection of polynucleotides based on the distance-dependent optical properties of gold nanoparticles. *Science*, 277(5329):1078–1081, 1997. 1

[11] J. Lee, P. Hernandez, J. Lee, A. O. Govorov, and N. A. Kotov. Exciton-plasmon interactions in molecular spring assemblies of nanowires and wavelength-based protein detection. *Nature Materials*, 6:291 – 295, 2007.

[12] J.-S. Lee, M. S. Han, and C. A. Mirkin. Colorimetric detection of mercuric ion (hg2+) in aqueous media using dna-functionalized gold nanoparticles. *Angewandte Chemie*, 119(22):4171–4174, 2007. 1, 105

[13] R. J. Tseng, L. Ouyang J. Tsai, C. Ma, C. S. Ozkan, and Y. Yang. Digital memory device based on tobacco mosaic virus conjugated with nanoparticles. *Nature Nanotechnology*, 1:72–77, 2006. 2

[14] S. Sun, C. B. Murray, D. Weller, L. Folks, and A. Moser. Monodisperse fept nanoparticles and ferromagnetic fept nanocrystal superlattices. *Science*, 287(5460):1989–1992, 2000. 2

[15] M. A. Correa-Duarte, J. Perez-Juste, A. Sanchez-Iglesias, M. Giersig, and L. M. Liz-Marzan. Aligning au nanorods by using carbon nanotubes as templates. *Angewandte Chemie International Edition*, 44(28):4375–4378, 2005. 2

[16] H. Wang, W. Lin, K. P. Fritz, G. D. Scholes, M. A. Winnik, and I. Manners. Cylindrical block co-micelles with spatially selective functionalization by nanoparticles. *Journal of the American Chemical Society*, 129(43):12924–12925, 2007. 2

[17] E. Dujardin, C. Peet, G. Stubbs, J. N. Culver, and S. Mann. Organization of metallic nanoparticles using tobacco mosaic virus templates. *Nano Letters*, 3(3):413–417, 2003. 2

[18] F. A. Aldaye, . L. Palmer, and H. F. Sleiman. Assembling materials with dna as the guide. *Science*, 321(5897):1795–1799, 2008. 2

[19] G. Gopalakrishnan, C. Danelon, P. Izewska, M. Prummer, P.-Y. Bolinger, I. Geissbuhler, D. Demurtas, J. Dubochet, and H. Vogel. Multifunctional

lipid/quantum dot hybrid nanocontainers for controlled targeting of live cells. *Angewandte Chemie International Edition*, 45(33):5478–5483, 2006. 2

[20] B. Zebli, A. S. Susha, G. B. Sukhorukov, A. L. Rogach, and W. J. Parak. Magnetic targeting and cellular uptake of polymer microcapsules simultaneously functionalized with magnetic and luminescent nanocrystals. *Langmuir*, 21(10):4262–4265, 2005.

[21] A. G. Skirtach, A. Munoz Javier, O. Kreft, K. Kahler, A. Alberola, H. Mohwald, W. J. Parak, and G. B. Sukhorukov. Laser-induced release of encapsulated materials inside living cells. *Angewandte Chemie International Edition*, 45(28):4612–4617, 2006. 2

[22] O.D. Velev, K. Furusawa, and K. Nagayama. Assembly of latex particles by using emulsion droplets as templates .1. Microstructured hollow spheres. *Langmuir*, 12(10):2374–2384, MAY 15 1996. 2, 26

[23] O.D. Velev, K. Furusawa, and K. Nagayama. Assembly of latex particles by using emulsion droplets as templates .2. Ball-like and composite aggregates. *Langmuir*, 12(10):2385–2391, MAY 15 1996. 2, 26

[24] F. Bai, D. Wang, Z. Huo, W. Chen, L. Liu, X. Liang, C. Chen, X. Wang, Q. Peng, and Y. Li. A versatile bottom-up assembly approach to colloidal spheres from nanocrystals. *Angewandte Chemie*, 46(35):6650–6653, 2007. 44, 105

[25] R. G. Harrison, A. L. Washburn, A. T. Pickett, and D. M. Call. Assembly of cdse nanoparticles into microspheres by a liquid droplet emulsion process. *J. Mater. Chem.*, 18:3718–3722, 2008.

[26] S.-H. Kim, Y.-S. Cho, S.-J. Jeon, T. H. Eun, G.-R. Yi, and S.-M. Yang. Microspheres with tunable refractive index by controlled assembly of nanoparticles. *Advanced Materials*, 20(17):3268, SEP 3 2008. 2

[27] Z. Tang and N. A. Kotov. One-dimensional assemblies of nanoparticles: Preparation, properties, and promise. *Advanced Materials*, 17(8):951–962, 2005. 2

[28] Q. Zhang, S. Gupta, T. Emrick, and T. P. Russell. Surface-functionalized cdse nanorods for assembly in diblock copolymer templates. *Journal of the American Chemical Society*, 128(12):3898–3899, 2006. 2

[29] V. N. Manoharan, M. T. Elsesser, and D. J. Pine. Dense packing and symmetry in small clusters of microspheres. *Science*, 301(5632):483–487, JUL 25 2003. 2, 26, 43, 53, 57, 74

[30] V. N. Manoharan. Colloidal spheres confined by liquid droplets: Geometry, physics, and physical chemistry. *Solid State Communications*, 139(11-12):557–561, 2006. 2, 43, 74, 105

[31] J. C. Maxwell Garnett. Colours in metal glasses and in metallic films. *Philosophical Transactions of the Royal Society of London. Series A, Containing Papers of a Mathematical or Physical Character*, 203:385–420, 1904. 6, 54, 70, 91, 101

[32] G. Mie. Beitrage zur optic truber medien, speziell kolloidaler metalloesungen. *Ann. Phys.*, 25:377, 1908. 6

[33] C. F. Bohren and D. R. Huffman. *Absorption and Scattering of Light by Small Particles*. Wiley, New York, 1983. 6, 9

[34] U. Kreibig and M. Vollmer. *Optical Properties of Metal Clusters*. Springer, Berlin, 1995. 6, 9

[35] A. Moores and F. Goettmann. The plasmon band in noble metal nanoparticles: an introduction to theory and applications. *New J. Chem.*, 30(8):1121–1132, Jun 2006. 7, 54, 91, 101

[36] Paul Mulvaney. Surface plasmon spectroscopy of nanosized metal particles. *Langmuir*, 12(3):788–800, 1996. 7, 10, 12, 89

[37] S. Link and M. A. El-Sayed. Simulation of the optical absorption spectra of gold nanorods as a function of their aspect ratio and the effect of the medium dielectric constant. *J. Phys. Chem. B*, 109:10531, 2005. 9, 10

[38] Jie Zeng, Stefan Roberts, and Younan Xia. Nanocrystal-based time-temperature indicators. *Chemistry European Journal*, 16(42):12559–12563, 2010. 9

[39] M. Rycenga, C. M. Cobley, J. Zeng, W. Li, C. H. Moran, Q. Zhang, D. Qin, and Y. Xia. Controlling the synthesis and assembly of silver nanostructures for plasmonic applications. *Chemical Reviews*, 111(6):3669–3712, 2011. 9, 11

[40] S. Eustis and M. A. El-Sayed. Why gold nanoparticles are more precious than pretty gold: Noble metal surface plasmon resonance and its enhancement of the radiative and nonradiative properties of nanocrystals of different shapes. *Chem. Soc. Rev.*, 35:209–217, 2006. 11

[41] S. Underwood and P. Mulvaney. Effect of the solution refractive index on the color of gold colloids. *Langmuir*, 10(10):3427–3430, 1994. 10, 11

[42] A.E. Hughes and S.C. Jain. Metal colloids in ionic crystals. *Advances in Physics*, 28:717–828, 1979. 12

[43] J. Turkevich, P. C. Stevenson, and J. Hillier. A study of the nucleation and growth processes in the synthesis of colloidal gold. *Discuss. Faraday. Soc.*, 11:55–75, 1951. 12

[44] B. V. Derjaguin and L. Landau. Theory of the stability of strongly charged lyophobic sols and of the adhesion of strongly charged particles in solutions of electrolytes. *Acta Physicochim.*, 14:633, 1941. 13

[45] E. J. W. Verwey and J. Th. G. Overbeek. *Theory of the stability of lyophobic colloids*. Elsevier., 1948. 13

[46] X. Ben and H. S. Park. Size dependence of the plasmon ruler equation for two-dimensional metal nanosphere arrays. *J. Phys. Chem. C*, 115:15915–15926, 2011. 14, 91, 101

[47] C. Sonnichsen, B. M. Reinhard, J. Liphardt, and A. P. Alivisatos. A molecular ruler based on plasmon coupling of single gold and silver nanoparticles. *Nat. Biotechnol.*, 23:741– 745, 2005. 14

[48] P. K. Jain, W. Huang, and M. A. El-Sayed. On the universal scaling behavior of the distance decay of plasmon coupling in metal nanoparticle pairs: A plasmon ruler equation. *Nano Letters*, 7:2080–2088, 2007. 14

[49] P. K. Jain and M. A. El-Sayed. Surface plasmon coupling and its universal size scaling in metal nanostructures of complex geometry: Elongated particle pairs and nanosphere trimers. *J. Phys. Chem. C*, 112:4954–4960, 2008. 91, 101

[50] W. Huang, W. Qian, P. K. Jain, and M. A. El-Sayed. The effect of plasmon field on the coherent lattice phonon oscillation in electron-beam fabricated gold nanoparticle pairs. *Nano Letters*, 7(10):3227–3234, 2007. 14

[51] H. Yan, S. Cingarapu, K. J. Klabunde, A. Chakrabarti, and C. M. Sorensen. Nucleation of gold nanoparticle superclusters from solution. *Phys. Rev. Lett.*, 102:095501, Mar 2009. 15

[52] P. Born and T. Kraus. Ligand-dominated temperature dependence of agglomeration kinetics and morphology in alkyl-thiol-coated gold nanoparticles. *Phys Rev E*, 6:062313, 2013. 15, 78, 100, 108

[53] M. P. Pileni. Supra- and nanocrystallinity: Specific properties related to crystal growth mechanisms and nanocrystallinity. *J. Phys.: Condens. Matter*, 23:503102, 2011. 15

[54] N. Goubet, J. Richardi, P. A. Albouy, and M. P. Pileni. How to predict the growth mechanism of supracrystals from gold nanocrystals. *The Journal of Physical Chemistry Letters*, 2(5):417–422, 2011. 15, 78

[55] Tihamér Geyer, Philip Born, and Tobias Kraus. Switching between crystallization and amorphous agglomeration of alkyl thiol-coated gold nanoparticles. *Phys. Rev. Lett.*, 109:128302, Sep 2012. 15

[56] J. Sjoblom. *Emulsions and Emulsion Stability*. CRC Press, 2005. 16, 20

[57] T. F. Tadros. *Emulsion Science and Technology: A General Introduction*. Wiley-VCH Verlag GmbH & Co. KGaA, 2009. 17

[58] R. P. Borwankar, L. A. Lobo, and D. T. Wasan. Emulsion stability - kinetics of flocculation and coalescence. *Colloids and Surfaces*, 69:135, 1992. 18, 20

[59] E. Dickinson. *Hydrocolloids and Emulsion Stability, Chap. 2, in: Handbook of Hydrocolloids (Second Edition)*. CRC Press, 2009. 19

[60] R. Chanamai and D. J. McClements. Dependence of creaming and rheology of monodisperse oil-in-water emulsions on droplet size and concentration. *Colloids and Surfaces A*, 172:79, 2000. 19

[61] S. U. Pickering. Emulsions. *J. Chem. Soc., Trans.*, 91:2001–2021, 1907. 21, 22, 60

[62] W. D. Bancroft. The theory of emulsification. *J. Phys. Chem.*, 17:501–519, 1913. 21

[63] W. C. Griffin. Classification of surface active agents by hlb. *J. Soc. Cosmet. Chem.*, 1:311–326, 1949. 21

[64] W. C. Griffin. Calculation of hlb values of non-ionic surfactants. *J. Soc. Cosmet. Chem.*, 5:249–256, 1954. 21

[65] W. Ramsden. Separation of solids in the surface-layers of solutions and suspensions. *Proc. Roy. Soc.*, 72:156, 1903. 22

[66] R. Aveyard, B. P. Binks, and J. H. Clint. Emulsions stabilised solely by colloidal particles. *Advances in Colloid and Interface Science*, 100-102(0):503–546, 2003. 22

[67] H. Wang and E. K. Hobbie. Amphiphobic carbon nanotubes as macroemulsion surfactants. *Langmuir*, 19(8):3091–3093, 2003. 22

[68] L. S. Dorobantu, A. K. C. Yeung, J. M. Foght, and M. R. Gray. Stabilization of oil-water emulsions by hydrophobic bacteria. *Appl. Env. Microbiology*, 70:6333–6336, 2004. 23

[69] B. P. Binks, J. H. Clint, G. Mackenzie, C. Simcock, and C. P. Whitby. Naturally occurring spore particles at planar fluid interfaces and in emulsions. *Langmuir*, 21:8161–8167, 2005. 23

[70] S. Simovic and C. A. Prestidge. Nanoparticle layers controlling drug release from emulsions. *Eur. J. Pharm. Biopharm.*, 67:39–47, 2007. 23

[71] B. P. Binks. Particles as surfactants : similarities and differences. *Current Opinion in Colloid & Interface Science*, 7(12):21, 2002. 23, 24

[72] S. Levine, B.D. Bowen, and S. J. Partridge. Stabilization of emulsions by fine particles i. partitioning of particles between continuous phase and oil/water interface. *Colloids and Surfaces*, 38(2):325–343, 1989.

[73] J. H. Clint and S. E. Taylor. Particle size and interparticle forces of overbased detergents: A langmuir trough study. *Colloids and Surfaces*, 65(1):61–67, 1992. 24

[74] Z. Nie, A. Petukhova, and E. Kumacheva. Properties and emerging applications of self-assembled structures made from inorganic nanoparticles. *Nature Nanotechnology*, 5:15, 2010. 25, 105

[75] J. Zhang, Z. Wang, J. Liu, S. Chen, and G. Liu. *Self-assembled nanostructures*. Kluwer Academic/Plenum Publisher, 2003. 25

[76] Y. Xia, Y. Yin, Y. Lu, and J. McLellan. Template-assisted self-assembly of spherical colloids into complex and controllable structures. *Advanced Functional Materials*, 13(12):907–918, 2003. 25

[77] Z. Nie, W. Li, M. Seo, S. Xu, and E. Kumacheva. Janus and ternary particles generated by microfluidic synthesis: Design, synthesis, and self-assembly. *Journal of the American Chemical Society*, 128:9408–9412., 2006. 26

[78] V. Rastogi, S. Melle, O. G. Calderon, A. A. Garcia, M. Marquez, and O. D. Velev. Synthesis of light-diffracting assemblies from microspheres and nanoparticles in droplets on a superhydrophobic surface. *Advanced Materials*, 20:4263–4268, 2008. 26, 44, 108

[79] P. Garstecki, I. Gitlin, W. DiLuzio, G. M. Whitesides, E. Kumacheva, and H. A. Stone. Formation of monodisperse bubbles in a microfluidic flow-focusing device. *App. Phys. Lett.*, 85:2649–2651., 2004. 26, 107

[80] D. R. Link, E. Grasland-Mongrain, A. Duri, F. Sarrazin, Z. D. Cheng, G. Cristobal, M. Marquez, and D. A. Weitz. Electric control of droplets in microfluidic devices. *Angewandte Chemie International Edition*, 45:2556–2560, 2006. 26

[81] J. Ally, B. Martin, M. B. Khamesee, W. Roa, and A. Amirfazli. Magnetic targeting of aerosol particles for cancer therapy. *J. Magn. Magn. Mater.*, 293(1):442 – 449, 2005. 26

[82] P. Dames, B. Gleich, A. Flemmer, K. Hajek, N. Seidl, Wiekhorst. F., D. Eberbeck, I. Bittmann, C. Bergemann, T. Weyh, L. Trahms, J. Rosenecker, and C. Rudolph. Targeted delivery of magnetic aerosol droplets to the lung. *Nat. Nano.*, 2:495–499, 2007.

[83] F. F. Sahle, H. Metz, J. Wohlrab, and R. H. H. Neubert. Lecithin-based microemulsions for targeted delivery of ceramide ap into the stratum corneum: Formulation, characterizations, and in vitro release and penetration studies. *Pharm Res.*, 2012. 26

[84] A. D. Dinsmore, M. F. Hsu, M. G. Nikolaides, M. Marquez, A. R. Bausch, and D. A. Weitz. Colloidosomes: Selectively permeable capsules composed of colloidal particles. *Science*, 298(5595):1006–1009, 2002. 26

[85] S. M. Klein, V. N. Manoharan, D. J. Pine, and F. F. Lange. Synthesis of spherical polymer and titania photonic crystallites. *Langmuir*, 21(15):6669–6674, JUL 19 2005. 27, 53, 107

[86] Nanfeng Zheng, Jie Fan, and Galen D. Stucky. One-step one-phase synthesis of monodisperse noble-metallic nanoparticles and their colloidal crystals. *Journal of the American Chemical Society*, 128(20):6550–6551, 2006. 28

[87] S. K. Hait and S. P. Moulik. Determination of critical micelle concentration (cmc) of nonionic surfactants by donor-acceptor interaction with lodine and correlation of cmc with hydrophile-lipophile balance and other parameters of the surfactants. *Journal of Surfactants and Detergents*, 4(3):303–309, 2001. 29

[88] L. S. C. Wan and P. F. S. Lee. Cmc of polysorbates. *Journal of Pharmaceutical Sciences*, 63(1):136–137, 1974. 29

[89] C.C. Ruiz. A photophysical study of the urea effect on micellar properties of sodium dodecylsulfate aqueous solutions. *Colloid and Polymer Science*, 273(11):1033–1040, 1995. 29

[90] L. Rayleigh. The incidence of light upon a transparent sphere of dimensions comparable with the wave-length. *Proceedings of the Royal Society A*, 84:25, 1910. 38

[91] M. Sztucki and T. Narayanan. Development of an ultra-small-angle X-ray scattering instrument for probing the microstructure and the dynamics of soft matter. *J. App. Crys.*, 40(1):459–462, APR 2007. 39, 49, 56

[92] T. Sobisch, D. Lerche, S. Kuechler, and A. Uhl. Rapid stability assessment for liquid and paste-like foods with multisample analytical centrifugation. *Proceedings Euro Food Chem XIII, Macromolecules and their degradation products in food physiological, analytical and technological aspects,*, pages 671–675, 2005. 40

[93] J. Lacava, P. Born, and T. Kraus. Nanoparticle clusters with lennard-jones geometries. *Nano Letters*, 12(6):3279–3282, 2012. 43, 67, 70, 74

[94] Y. Cho, G. Yi, S. Kim, D. J. Pine, and S. Yang. Colloidal clusters of microspheres from water-in-oil emulsions. *Chemistry of Materials*, 17:5006–5013, 2005. 43, 44, 45, 105

[95] B. A. Korgel, S. Fullam, S. Connolly, and D. Fitzmaurice. Assembly and self-organization of silver nanocrystal superlattices: Ordered "soft spheres". *J. Phys. Chem. B*, 102(43):8379–8388, October 1998. 47, 73

[96] W. Niu and G. Xu. Crystallographic control of noble metal nanocrystals. *Nano Today*, 6(3):265 – 285, 2011. 47, 51, 74

[97] D. J. Wales, J. P. K. Doye, A. Dullweber, M. P. Hodges, F. Naumkin, F. Y.and Calvo, and T. F. Hernandez-Rojas, J.and Middleton. Cambridge cluster database. 51, 110

[98] X. G. Shao. Global minimal energies and coordninates of the lj clusters for n=151-309 and n=1001-1610. 51, 110

[99] A. L. Mackay. A dense non-crystallographic packing of equal spheres. *Acta Crystallographica*, 15(9):916–918, Sep 1962. 52, 54

[100] Jonathan P. K. Doye and David J. Wales. Structural consequences of the range of the interatomic potential a menagerie of clusters. *J. Chem. Soc.*, 93:4233–4243, 1997.

[101] E. G. Noya, J. P.K. Doye, D. J. Wales, and A. Aguado. Geometric magic numbers of sodium clusters: Interpretation of the melting behaviour. *Euro. Phys. J. D*, 43:57–60, 2007. 52

[102] B. P. Binks and J. H. Clint. Solid wettability from surface energy components: Relevance to pickering emulsions. *Langmuir*, 18(4):1270–1273, 2002. 53

[103] B. P. Binks and S. O. Lumsdon. Influence of particle wettability on the type and stability of surfactant-free emulsions. *Langmuir*, 16(23):8622–8631, 2000. 53

[104] N. Tsapis, D. Bennett, B. Jackson, D.A. Weitz, and D.A. Edwards. Trojan particles: Large porous carriers of nanoparticles for drug delivery. *PNAS*, 99(19):12001–12005, SEP 17 2002. 53

[105] N. Glaser, D. J. Adams, A. Boeker, and G. Krausch. Janus particles at liquid-liquid interfaces. *Langmuir*, 22(12):5227–5229, JUN 6 2006. 53, 62

[106] E. Vignati. *Optical methods for the investigation of application-oriented complex fluids*. PhD thesis, Dipartimento di Ingegneria Nucleare, Politechnico di Milano, 2005. 53

[107] Wiel H. Evers, Bart De Nijs, Laura Filion, Sonja Castillo Castillo, Marjolein Dijksra, and Daniel Vanmaekelbergh. Entropy-driven formation of binary semiconductor-nanocrystal superlattices. *Nano Letters*, 10:4235–4241, 2010. 59

[108] D. J. Wales and T. V. Bogdan. Potential energy and free energy landscapes. *The Journal of Physical Chemistry B*, 110(42):20765–20776, 2006. 59

[109] J. Lacava, A.-A. Ouali, B. Raillard, and T. Kraus. On the behaviour of nanoparticles in oil-in-water emulsions with different surfactants. *Soft Matter*, 2014. 60

[110] Tharwat F. Tadros. *Surfactants in the Food Industry*, pages 595–629. Wiley-VCH Verlag GmbH & Co. KGaA, 2005. 60

[111] M. Rieger and L. D. Rhein. *Surfactants in Cosmetics, Second Edition.* CRC Press, 1997. 60

[112] D. Karsa. *Surfactants in Polymers, Coatings, Inks, and Adhesives.* Blackwell, 2003. 60

[113] L. L. Schramm. *Surfactants: Fundamentals and Applications in the Petroleum Industry.* Cambridge University Press, 2000. 60

[114] Bernard P. Binks, Jhonny A. Rodrigues, and William J. Frith. Synergistic interaction in emulsions stabilized by a mixture of silica nanoparticles and cationic surfactant. *Langmuir*, 23(7):3626–3636, 2007. 60

[115] B. P. Binks, A. Desforges, and D. G. Duff. Synergistic stabilization of emulsions by a mixture of surface-active nanoparticles and surfactant. *Langmuir*, 23(3):1098–1106, 2007. 60

[116] Huan Ma, Mingxiang Luo, and Lenore L. Dai. Influences of surfactant and nanoparticle assembly on effective interfacial tensions. *Phys. Chem. Chem. Phys.*, 10:2207–2213, 2008. 61

[117] C. P. Whitby, D. Fornasiero, and J. Ralston. Effect of adding anionic surfactant on the stability of pickering emulsions. *Journal of Colloid and Interface Science*, 329(1):173 – 181, 2009. 61

[118] Charu Vashisth, Catherine P. Whitby, Daniel Fornasiero, and John Ralston. Interfacial displacement of nanoparticles by surfactant molecules in emulsions. *Journal of Colloid and Interface Science*, 349(2):537 – 543, 2010. 61

[119] N. G. Eskandar, S. Simovic, and C. A. Prestidge. Interactions of hydrophilic silica nanoparticles and classical surfactants at non-polar oil-water interface. *Journal of Colloid and Interface Science*, 358(1):217 – 225, 2011. 61, 70

[120] P. Joos, D. Vollhardt, and M. Vermeulen. Interfacial tension of sodium dodecyl sulfate solutions at the hexane-water interface. *Langmuir*, 6(2):524–525, 1990. 62

[121] L. J. Peltonen and J. Yliruusi. Surface pressure, hysteresis, interfacial tension, and {CMC} of four sorbitan monoesters at water-air, water-hexane, and hexane-air interfaces. *Journal of Colloid and Interface Science*, 227(1):1 – 6, 2000. 62

[122] A. Yeung, T. Dabros, and J. Masliyah. Does equilibrium interfacial tension depend on method of measurement? *Journal of Colloid and Interface Science*, 208(1):241 – 247, 1998. 62

[123] W. Wang, Z. Zhou, K. Nandakumar, Z. Xu, and J. H. Masliyah. Effect of charged colloidal particles on adsorption of surfactants at oil-water interface. *Journal of Colloid and Interface Science*, 274(2):625 – 630, 2004. 70

[124] M. Sztucki, T. Narayanan, G. Belina, A. Moussaid, F. Pignon, and H. Hoekstra. Kinetic arrest and glass-glass transition in short-ranged attractive colloids. *Phys. Rev. E*, 74(5, Part 1):051504, NOV 2006. 71

[125] Carl S. Weisbecker, Margaret V. Merritt, and George M. Whitesides. Molecular self-assembly of aliphatic thiols on gold colloids. *Langmuir*, 12(16):3763–3772, 1996. 76

[126] Shu-Yi Lin, Yi-Ting Tsai, Chien-Chih Chen, Chia-Mei Lin, and Chun-hsien Chen. Two-step functionalization of neutral and positively charged thiols onto citrate-stabilized au nanoparticles. *The Journal of Physical Chemistry B*, 108(7):2134–2139, 2004.

[127] J. Christopher Love, Lara A. Estroff, Jennah K. Kriebel, Ralph G. Nuzzo, and George M. Whitesides. Self-assembled monolayers of thiolates on metals as a form of nanotechnology. *Chemical Reviews*, 105(4):1103–1170, 2005. 76

[128] Herwig Dollefeld, Kathrin Hoppe, Joanna Kolny, Kristian Schilling, Horst Weller, and Alexander Eychmuller. Investigations on the stability of thiol stabilized semiconductor nanoparticles. *Phys. Chem. Chem. Phys.*, 4:4747–4753, 2002. 76, 80

[129] Gregory Kalyuzhny and Royce W. Murray. Ligand effects on optical properties of cdse nanocrystals. *The Journal of Physical Chemistry B*, 109(15):7012–7021, 2005. 77

[130] Jose Aldana, Y. Andrew Wang, and Xiaogang Peng. Photochemical instability of cdse nanocrystals coated by hydrophilic thiols. *Journal of the American Chemical Society*, 123(36):8844–8850, 2001. 77, 102

[131] Guangjun Cheng, Cindi L. Dennis, Robert D. Shull, and A. R. Hight Walker. Probing the growth and aging of colloidal cobalt nanocrystals: A combined study by transmission electron microscopy and magnetic measurements. *Crystal Growth & Design*, 9(8):3714–3720, 2009. 77, 80

[132] Michael J. Hostetler, Allen C. Templeton, and Royce W. Murray. Dynamics of place-exchange reactions on monolayer-protected gold cluster molecules. *Langmuir*, 15(11):3782–3789, 1999. 77

[133] T. Djebaili, J. Richardi, S. Abel, and M. Marchi. Atomistic simulations of the surface coverage of large gold nanocrystals. *The Journal of Physical Chemistry C*, 117(34):17791–17800, 2013. 77

[134] Victor Chechik. Reduced reactivity of aged au nanoparticles in ligand exchange reactions. *Journal of the American Chemical Society*, 126(25):7780–7781, 2004. PMID: 15212517. 77

[135] Y. Ma and V. Chechik. Aging of gold nanoparticles. *Langmuir*, 27(3):14432–14437, 2011. 77

[136] Sjoerd Hak, Emily Helgesen, Helga H. Hektoen, Else Marie Huuse, Peter A. Jarzyna, Willem J.M. Mulder, Olav Haraldseth, and Catharina de Lange Davies. The effect of nanoparticle polyethylene glycol surface density on ligand-directed tumor targeting studied in vivo by dual modality imaging. *ACS Nano*, 6(6):5648–5658, 2012. 78

[137] Georgi As. Georgiev, Dipak K. Sarker, Othman Al-Hanbali, Georgi D. Georgiev, and Zdravko Lalchev. Effects of poly (ethylene glycol) chains conformational transition on the properties of mixed dmpc/dmpe-peg thin liquid films and monolayers. *Colloids and Surfaces B: Biointerfaces*, 59(2):184 – 193, 2007. 78

[138] J. J. Choi, C. R. Bealing, K. Bian, K. J. Hughes, W. Zhang, D.-M. Smilgies, R. G. Hennig, J. R. Engstrom, and T. Hanrath. Controlling nanocrystal superlattice symmetry and shape-anisotropic interactions through variable ligand surface coverage. *Journal of the American Chemical Society*, 133(9):3131–3138, 2011. 78, 102, 103

[139] Yuan Feng Wang, Rui Qin Yang, Zhi Xia Shi, Jian Jun Liu, Ke Zhao, and Yan Ji Wang. The effectiveness of cdse nanoparticle suspension for developing latent fingermarks. *Journal of Saudi Chemical Society*, 18(1):13 – 18, 2014. 80

[140] K. Loza, J. Diendorf, C. Sengstock, L. Ruiz-Gonzalez, J. M. Gonzalez-Calbet, M. Vallet-Regi, M. Koller, and M. Epple. The dissolution and biological effects of silver nanoparticles in biological media. *J. Mater. Chem. B*, 2:1634–1643, 2014. 80

[141] Gerd H. Woehrle, Leif O. Brown, and James E. Hutchison. Thiol-functionalized, 1.5-nm gold nanoparticles through ligand exchange reactions: scope and mechanism of ligand exchange. *Journal of the American Chemical Society*, 127(7):2172–2183, 2005. PMID: 15713095. 80, 93

[142] P. Kanninen, C. Johans, J. Merta, and K. Kontturi. Influence of ligand structure on the stability and oxidation of copper nanoparticles. *Journal of Colloid and Interface Science*, 318(1):88 – 95, 2008. 80, 93

[143] L. Piot, S. Le Floch, T. Cornier, S. Daniele, and D. Machon. Amorphization in nanoparticles. *The Journal of Physical Chemistry C*, 117(21):11133–11140, 2013. 80

[144] Paul Mulvaney, Jorge Perez-Juste, Michael Giersig, LuisM. Liz-Marzan, and Carlos Pecharroman. Drastic surface plasmon mode shifts in gold nanorods due to electron charging. *Plasmonics*, 1(1):61–66, 2006. 91, 101

[145] S. A. Maier, M. L. Brongersma, P. G. Kik, S. Meltzer, A. A. G. Requicha, and H. A. Atwater. Plasmonics : A route to nanoscale optical devices. *Advanced Materials*, 13:1501–1505, 2001. 91, 101

[146] E. Hutter and J. H. Fendler. Exploitation of localized surface plasmon resonance. *Advanced Materials*, 16(19):1685–1706, 2004. 91, 101

[147] Scott F. Sweeney, Gerd H. Woehrle, and James E. Hutchison. Rapid purification and size separation of gold nanoparticles via diafiltration. *Journal of the American Chemical Society*, 128(10):3190–3197, 2006. 99

[148] S. K. Balasubramanian, L. Yang, L. L. Yung, C.-N. Ong, W.-Y. Ong, and L. E. Yu. Characterization, purification, and stability of gold nanoparticles. *Biomaterials*, 31(34):9023 – 9030, 2010.

[149] M. F. Ferreira, B. Mousavi, P. M. Ferreira, C. I. O. Martins, L. Helm, J. A. Martins, and C. F. G. C. Geraldes. Gold nanoparticles functionalised with stable, fast water exchanging gd3+ chelates as high relaxivity contrast agents for mri. *Dalton Trans.*, 41:5472–5475, 2012.

[150] F. R. Kersey, T.J. Merkel, J. L. Perry, M. E. Napier, and J. M. DeSimone. Effect of aspect ratio and deformability on nanoparticle extravasation through nanopores. *Langmuir*, 28(23):8773–8781, 2012. 99

[151] Verena Goertz, Frederik Weis, Elena Keln, Hermann Nirschl, and Martin Seipenbusch. The effect of water vapor on the particle structure and size of silica nanoparticles during sintering. *Aerosol Science and Technology*, 45(11):1287–1293, 2011. 100

[152] Prashant K. Jain, Wei Qian, and Mostafa A. El-Sayed. Ultrafast cooling of photoexcited electrons in gold nanoparticles-thiolated dna conjugates involves the dissociation of the gold-thiol bond. *Journal of the American Chemical Society*, 128(7):2426–2433, 2006. PMID: 16478198. 101

[153] R.E. Benfield, J.A. Creighton, D.G. Eadon, and G. Schmid. The relationship of au55(pph3)12cl6 to colloidal gold. *Zeitschrift für Physik D Atoms, Molecules and Clusters*, 12(1-4):533–536, 1989. 101

[154] Yvonne Joseph, Berit Guse, and Gabriele Nelles. Aging of 1,ω-alkyldithiol interlinked au nanoparticle networks. *Chemistry of Materials*, 21(8):1670–1676, 2009. 102

[155] Y. Xia, T. D. Nguyen, M. Yang, B. Lee, A. Santos, Z. Podsiadlo, P. andTang, S. C. Glotzer, and N. A. Kotov. Self-assembly of self-limiting monodisperse supraparticles from polydisperse nanoparticles. *Nat. Nanotechnol.*, 6:580, 2011. 105

[156] T. P. Chou, Q. Zhang, G. E. Fryxell, and G. Cao. Hierarchically structured-cellsfilms for dye-sensitized solar cells with enhanced energy conversion efficiency. *Adv. Mater.*, 19:2588, 2007. 105

[157] T. P. Zhang, Q. andChou, B. Russo, S. A. Jenekhe, and G. Cao. Aggregation of zno nanocrystallites for high conversion efficiency in dye-sensitized solar cells. *Angew. Chem.*, 47:2402, 2008. 105

[158] X. Hu, J. Gong, L. Zhang, and J. C. Yu. Continuous size tuning of monodisperse zno colloidal nanocrystal clusters by a microwave-polyol process and their applications for humidity sensing. *Adv. Mater.*, 20:4845, 2008. 105

[159] T. Nakashima, M. Shimizu, and M. Kukizaki. Membrane emulsification by microporous glass. *Key Engineering Materials*, 61-62:513–516, 1991. cited By (since 1996)124. 107

[160] T. Nakashima, M. Shimizu, and M. Kukizaki. Particle control of emulsion by membrane emulsification and its applications. *Advanced drug delivery reviews*, 45(1):47–56, 2000. 107

[161] T. Kawakatsu, Y. Kikuchi, and M. Nakajima. Regular-sized cell creation in microchannel emulsification by visual microprocessing method. *Journal of the American Oil Chemists' Society*, 74(3):317–321, 1997. 107

[162] S. Sugiura, M. Nakajima, and M. Seki. Preparation of monodispersed emulsion with large droplets using microchannel emulsification. *Journal of the American Oil Chemists' Society*, 79(5):515–519, 2002.

[163] F.-C. Chang and Y.-C. Su. Controlled double emulsification utilizing 3d pdms microchannels. *Journal of Micromechanics and Microengineering*, 18(6):065018, 2008. 107

[164] H. Zhang, R. Tumarkin E. Peerani, Z. Nie, R. M. A. Sullan, G. C. Walker, and E. Kumacheva. Microfluidic production of biopolymer microcapsules with controlled morphology. *Journal of the American Chemical Society*, 128, 2006. 107

[165] Z.T. Cygan, J.T. Cabral, K. L. Beers, and E. J. Amis. Microfluidic platform for the generation of organic-phase microreactors. *Langmuir*, 21:36293634, 2005.

[166] P. Garstecki, M. A. Fischbach, and G. M. Whitesides. Design for mixing using bubbles in branched microfluidic channels. *Appl. Phys. Lett.*, 86:244108, 2005.

[167] S.D. Hudson, J. T. Cabral, W. J. Goodrum, K. L. Beers, and E. J. Amis. Microfluidic interfacial tensiometry. *Appl. Phys. Lett.*, 87:081905, 2005. 107

[168] E. V. Shevchenko, D. V. Talapin, C. B. Murray, and S. O'Brien. Structural characterization of self-assembled multifunctional binary nanoparticle superlattices. *Journal of the American Chemical Society*, 128(11):3620–3637, 2006. 108